Thermo-Electric Properties of One-Dimensional Constrictions

Olivio Chiatti

Royal Holloway
University of London

Dissertation submitted for the degree of
Doctor of Philosophy

July 2005

Abstract

This thesis describes low-temperature transport measurements in low-dimensional systems fabricated in high-mobility GaAs/AlGaAs heterostructures. These low-dimensional systems are formed by electrostatically constricting the electrons in the two-dimensional electron gas at the interface of the heterostructure, by applying a voltage to a pair of metallic gates known as a *split-gate*. At low temperatures the electrical conduction occurs without scattering. The aim is to measure the thermal conductance of these one-dimensional ballistic conductors.

The thermal conductance of a split-gate device was measured as a function of gate voltage, over a wide range of temperatures and in the absence of a magnetic field. The electrons on one side of the constriction were heated with an electric current, and the temperature drop across the split-gate was measured using the thermopower of another split-gate. The measurements show that the thermal conductance displays plateaux corresponding to the one-dimensional subbands, confirming previous results.

The design of the samples allows a quantitative test of the Wiedemann-Franz law in one-dimensional constrictions. The results strongly suggest that the Wiedemann-Franz law is satisfied, and new information was obtained regarding the anomaly in the conductance known as *0.7 structure*, which can provide a new insight into the nature of this anomaly. It is found that the thermal conductance corresponding to the anomaly is suppressed with respect to the value expected from a single-particle picture.

Acknowledgments

I thank my supervisor Dr. James Nicholls, whose support and patience made this work possible. I wish to thank Prof. Victor Petrashov for providing the research facilities. Many thanks to all members of the *Nanophysics and Nanotechnology* group, in particular to Massimo Venti and Dr. Rais Shaikhaidarov. None of the experimental work could have been possible without the high quality wafers grown in the MBE facility at the *Cavendish Laboratory*, Cambridge University, and the liquid Helium provided by Francis Greenough. Last, but not least, I thank my family and my friends.

Contents

List of Figures

List of Tables

Chapter 1

Basic Concepts

Electronic transport in a system is described as *low-dimensional*, when potential barriers constrain the electrons in one or more directions. This is achieved with structures that have relevant dimensions smaller than the de Broglie wavelength λ of the electrons.

If the kinetic energy of the electrons is smaller than the confining potential energy, the momentum and energy associated with the motion in the confined direction are quantized [1, 2]. The electrons lose one or more degrees of freedom and the system becomes two, one or zero-dimensional, depending on whether the confinement occurs along one, two or three directions. The dimensionality of a system depends on the length scales which determine the physical properties under study. In general, in order to quantize the motion of a particle in one direction, the confining potential must have a width comparable to the de Broglie wavelength $\lambda = h/p$ of the particle.

The electric transport of conducting materials like metals or semiconductors can be understood using the Drude model of the free electron gas. The transport properties at low temperatures are determined by the electrons close to the Fermi level E_F. Therefore, the electron gas will be considered low-dimensional if one or more sample dimensions are comparable to the *Fermi wavelength* λ_F (the de Broglie wavelength of the electrons at E_F).

Until the 1960s, quantum-confinement of electrons could be found only in naturally occurring systems, such as atoms, molecules and crystals. The first artificial structures with low-dimensional electronic systems were thin metallic films [3]. With the development of the semiconductor technology, the focus of the research in low-dimensional systems switched to Si MOSFETs (Metal Oxide-Semiconductor Field-Effect Transistor) and GaAs/AlGaAs heterostructures. Semicon-

ductors have two main advantages over metallic films. First, due to the relative high-quality of the semiconducting materials, the charge carriers have a higher mobility than in thin films. Second, by doping or by applying an electric field, the carrier concentration can be varied. The carrier density is much lower than in metals, with a Fermi wavelength comparable to structures that can be easily fabricated by lithographic methods. Semiconductors made it possible to study novel transport regimes, as for example the ballistic regime. For general reviews of the field see Refs. [4–9].

In this chapter, the basic concepts about *low-dimensional electronic gases* (LDEGs) are introduced. We will first see how quantum confinement of electrons is achieved in the practice, concentrating on the GaAs/AlGaAs heterostructure. Then, in order to interpret correctly the transport properties of low-dimensional electronic systems, we have to understand the effect of the quantization of motion on the equilibrium properties of a free-electron gas. Finally we will introduce the semiclassical theory of homogeneous transport of LDEGs.

1.1 Low-dimensional electron gases in practice

In semiconductor technology there are two methods to achieve quantum confinement of charge carriers:

1. growth of inhomogeneous layer structures, where the confinement occurs in the growth direction, perpendicular to the substrate surface;

2. lateral pattering, achieved by ultrafine lithographic techniques.

Modulation-doped heterostructures

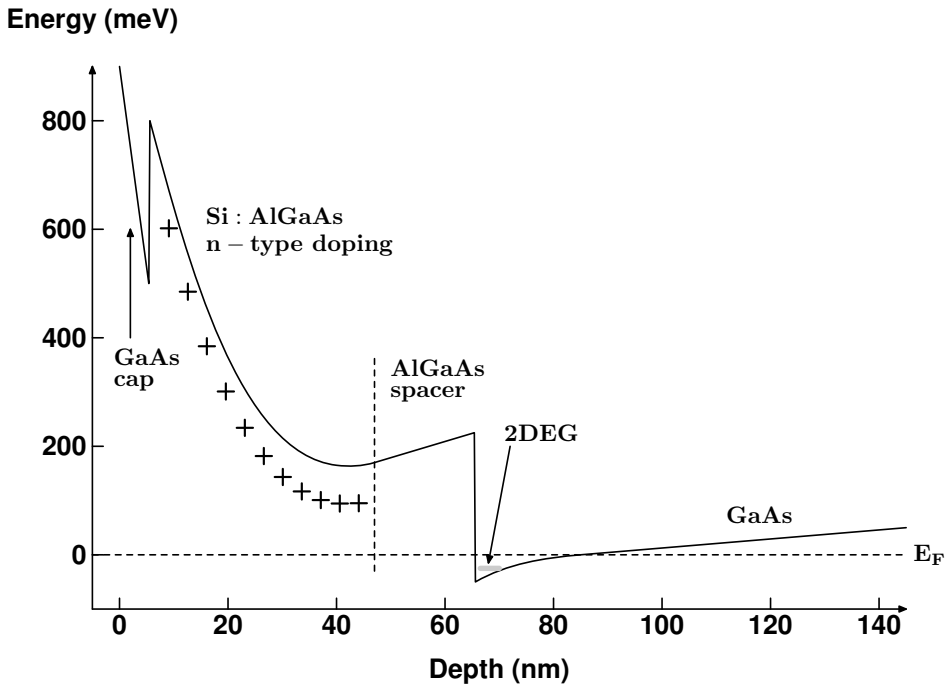

Figure 1.1: Conduction band profile of a GaAs/AlGaAs heterostructure. The 2DEG is formed in the potential well below the Fermi level E_F on the GaAs side of the interface, far from the ionized donors in the doped AlGaAs layer. The width of the potential well is of the order of 10 nm, comparable to the Fermi wavelength of the electrons.

Heterostructures are inhomogeneous layer structures, where the discontinuities in the conduction and valence band edges between different materials, provide potential discontinuities that can be used to confine electrons. The first example of confinement is the inversion layer of Silicon Metal-Oxide Semiconductor structures (Si MOS), where the confining potential is realized at the Si/SiO_2 interface. Ando *et al.* [4] focused on this material in their review.

Since the development of growth techniques such as Molecular Beam Epitaxy (MBE) and Metal Organic Chemical Vapor Deposition (MOCVD), it is possible to grow crystals in layers with atomic precision. By controlling the composition of the crystal and the doping, these techniques allow the fabrication of high-quality lattice-matched heterostructures and *band-structure engineering* is possible. This control also allows for *modulation doping*, where the dopants that provide the free charge carriers in the heterostructure are spatially separated from the carriers themselves, reducing the scattering from the ionized impurities [10].

The material of choice for research on low-dimensional systems in recent years has been the modulation-doped GaAs/AlGaAs heterostructure (also known as High-Electron-Mobility Transistor, HEMT). Figure 1.1 shows an example of a GaAs/AlGaAs heterostructure, which is fabricated by growing the ternary compound $Al_xGa_{1-x}As$ ($x \approx 0.33$) on a GaAs substrate. The mismatch in lattice spacing between the two materials is very small, and so the crystal has few lattice defects. At the interface between the two materials, the edge of the conduction band is bent to form a potential well, and electrons donated by Si dopants in the AlGaAs are trapped in the potential well at the interface. The dopants are spatially separated from the 2DEG by a spacer layer, thus reducing the scattering of the electrons by the ionized dopants.

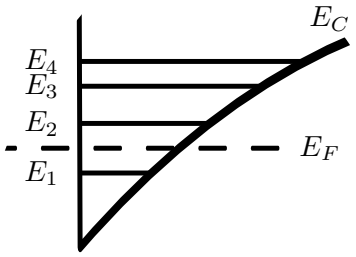

Figure 1.2: Schematic representation of the triangular potential well formed at the interface of the GaAs/AlGaAs heterostructure depicted in Fig. 1.1. E_C is the bottom of the conduction band, E_F is the chemical potential of the system, and E_1, E_2, *etc.*, are the 2D subbands of the electrons confined in the potential well. Typically only the first subband is occupied, as depicted.

As shown in Fig. 1.2, the potential well in a heterojunction is approximately triangular, and has a width comparable to the Fermi wavelength of the electrons. The result is that the motion of the electrons trapped in the potential well is quantized in the direction of growth of the crystal, but free in the plane parallel to the interface. The electrons confined at the interface form a *two-dimensional elec-*

tron gas (2DEG). For a more detailed review of AlGaAs/GaAs heterostructures, see Refs. [11, 12].

The other advantage of this heterostructure, besides the high mobility of the charge carriers, is the possibility of changing the charge density of the 2DEG. Three mechanisms are generally used: shining light onto the sample, increasing the hydrostatic pressure, and applying a voltage to a gate on the surface.

The electron density in a heterostructure at low temperature can be increased by *persistent photoconductivity* (PPC). There are several different optical processes that can generate extra electrons, and the effect is persistent because at low temperatures electrons are trapped at the interface.

Another method to change the carrier density is the fabrication of a gate electrode, as shown in Fig. 1.3. A metallic layer is deposited on the surface of the heterostructure, which forms a *Schottky gate* with the semiconducting material [13]. The charge density in the 2DEG is varied electrostatically by applying a voltage to the gate (one can picture the system as a parallel-plate capacitor). For more information on the fabrication of low-dimensional structures see Refs. [5, 9].

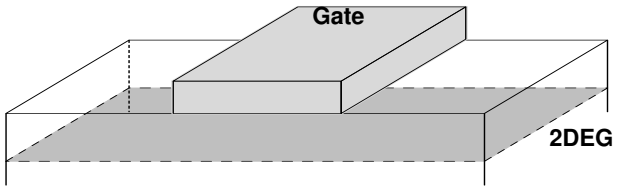

Figure 1.3: GaAs/AlGaAs heterostructure with a metallic gate deposited on the surface. Applying a negative voltage on the gate reduces the charge density in the region of the 2DEG beneath the gate.

Lateral confinement

The 2DEG created at a GaAs/AlGaAs heterojunction is the starting point for many investigations of one and zero-dimensional electron systems, obtained by further lateral confinement of the electrons in the 2DEG. In order to create a one-dimensional system, a narrow channel needs to be created in the plane of the 2DEG. Most of the methods presented here share the lithographic techniques that provide the pattern for lateral confinement.

Lithography refers to the method by which a desired pattern is transferred onto a substrate. Typically, a *resist* is spun onto the surface of the sample and is exposed selectively to a particular radiation source, which changes the chemical bonding in the irradiated regions. A suitable developer then dissolves the exposed

regions (*positive resist*) or the unexposed regions (*negative resist*), depending on the requirements. The most popular *nanolithographic* technique is *electron-beam lithography*: a modification of a conventional *Scanning Electron Microscope* (SEM) allows the *e-beam* to "write" the desired pattern directly onto the resist, with a typical resolution of $10 - 20$ nm. For a typical 2DEG formed in a heterostructure, with an electron density $n = 2 \times 10^{11}$ cm^{-2} and a mobility $\mu = 2 \times 10^{6}$ cm/Vs, the Fermi wavelength is $\lambda_F \approx 50$ nm.

The simplest technique for lateral confinement is *deep-mesa etching*, where the material is etched away to a depth below the GaAs/AlGaAs interface. This technique is typically used to prepare a 2DEG for large-scale geometry (like a Hall bar), but is not considered reliable for the small channel widths necessary to obtain one-dimensional transport.[1]

A more reliable approach is the *shallow-mesa etching* [14,15]. In this case, only the doped layer of AlGaAs is etched away, depleting selected regions of the 2DEG. A variation of this technique is the *trench-etching* [16], where regions of the 2DEG are separated by etching trenches between them. Both of these techniques have been used to fabricate one-dimensional channels.

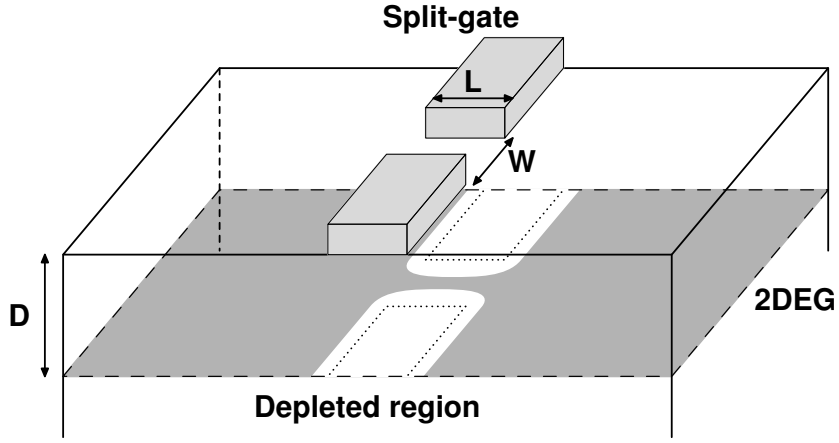

Figure 1.4: Schematic representation of a *split-gate device*. L and W are the lithographic length and width of the gap between the two gates, and D is the depth of the 2DEG with respect to the surface of the sample. Regions in the 2DEG are depleted by the application of a negative voltage to the split-gate, leaving a narrow channel connecting the two sides of the 2DEG.

The technique that allows for the widest variety of structures is the *split-gate technique* [17]. We have seen that the voltage applied to a Schottky gate on the

[1]The sidewall of the *mesa* has a large roughness compared to the GaAs/AlGaAs interface, and the defects left by the etching provide a high density of surface states, which affect the potential in the channel, "softening" the confining potential.

surface of the heterostructure can be used to control the electron density of the 2DEG. By applying a suitable negative voltage, it is possible to deplete regions of the 2DEG beneath a patterned electrode, allowing a selective depletion of the 2DEG. So it is possible to fabricate a variety of structures such as *quantum wires* and *quantum dots*. For a review of the techniques, with references, see Refs. [6,8,9].

1.2 Low-dimensional electron gases in equilibrium

In this section we review the basic properties of *low-dimensional electron gases* (LDEGs) in thermodynamic equilibrium. The results presented here can be applied to LDEGs in GaAs/AlGaAs heterostructure in a straightforward manner, by substituting the mass of the electron with the *effective mass* of electron in GaAs, $m^* = 0.067m_e$.[2] The details of the wavefunctions corresponding to the bound states are not required to understand the equilibrium properties of the electron gas. For reviews of this topic see Refs. [4–6, 9].

1.2.1 Electron gas: from 3D to 2D

Consider a gas of non-interacting electrons in a box of volume $V = L_x \times L_y \times L_z$. In the absence of magnetic fields, the solution of the time-independent Schrödinger equation for an electron yields

$$\psi(\mathbf{r}) = \frac{1}{\sqrt{V}} \exp\left(\mathrm{i}\mathbf{k} \cdot \mathbf{r}\right), \tag{1.1}$$

where $\mathbf{r} = (x, y, z)$ is the position vector and $\mathbf{k} = (k_x, k_y, k_z)$ is the wavevector. The state has momentum $\hbar\mathbf{k}$ and energy E_k:

$$E_k = \frac{\hbar^2 k^2}{2m^*} = \frac{\hbar^2}{2m^*}(k_x^2 + k_y^2 + k_z^2) \tag{1.2}$$

(m^* is the mass of the electron). The *density of states* (DOS) per unit volume is given by

$$D(E) = \frac{dN}{dE} = \frac{m^*}{\pi^2\hbar^2}\sqrt{\frac{2m^*E}{\hbar^2}}, \tag{1.3}$$

where $N(E)$ is the number of states per unit volume with energy between E and $E + dE$ (a factor 2 takes into account spin-degeneracy, $s = \frac{1}{2}$).

In thermodynamic equilibrium, the available states are occupied by the electrons according to the *Fermi-Dirac distribution*:

$$f_0(E, E_F, T) = \left[1 + \exp\left(\frac{E - E_F}{k_B T}\right)\right]^{-1}, \tag{1.4}$$

where E_F is the *Fermi level*, T is the temperature, and k_B the *Boltzmann constant*.

[2] In typical situations only one 2D subband is occupied and it is possible to work within the *effective mass approximation*, assuming parabolic bands.

At low temperatures the Fermi function becomes

$$f_0(E, E_F, T) \xrightarrow[T\to 0]{} \Theta(E_F - E), \tag{1.5}$$

where $\Theta(x)$ is the unit step function. This is known as the *degenerate limit* of an electron gas, where all the states with energy lower than the *Fermi energy*, $E \leq E_F$, are occupied. In the k-space, the occupied states with $k \leq k_F = \sqrt{\frac{2m^*}{\hbar^2}E_F}$ define the *Fermi sphere*. Also, the density of electrons can be related directly to the Fermi level:

$$n_{3\mathrm{d}} = \int_0^\infty D(E) f_0(E) dE = \frac{m^*}{\pi^2\hbar^2}\left(\frac{2m^*E_F}{\hbar^2}\right)^{\frac{3}{2}}. \tag{1.6}$$

If $L_z \leq \lambda_F = \dfrac{2\pi}{k_F}$, where λ_F is the *Fermi wavelength*, the electrons are confined to the xy-plane. A one-electron eigenstate is then

$$\psi(\mathbf{r}) = \psi'(x, y)\phi_n(z), \tag{1.7}$$

where $\phi_n(z)$ is the wavefunction corresponding to the confinement in the z-direction, and

$$\psi'(x, y) = \frac{1}{\sqrt{A}} \exp\left(\mathrm{i}(k_x x + k_y y)\right) \tag{1.8}$$

is the wavefunction for a free electron in the xy-plane ($A = L_x \times L_y$). The energy of this eigenstate is given by

$$E_{n,k} = E_n + \frac{\hbar^2}{2m^*}(k_x^2 + k_y^2), \tag{1.9}$$

where E_n is the (quantized) energy corresponding to $\phi_n(z)$. We can see that for each bound state n there is a continuum of states associated with free motion confined to the xy-plane. For every 2D *subband* n, the DOS is the same and does not depend on energy:

$$D_n(E) = \frac{m^*}{\pi\hbar^2}\Theta(E - E_n) \tag{1.10}$$

(a factor 2 is included to account for spin-degeneracy). Figure 1.5 depicts the total DOS of a 2DEG: every step of the staircase corresponds to one 2D subband.

Most situations involve 2DEGs where $E_1 < E_F < E_2$, where only the first 2D subband is occupied. In this case the DOS is constant, and, in the degenerate limit, the occupied states fill a circle in the k-space with radius k_F (see Fig. 1.6).

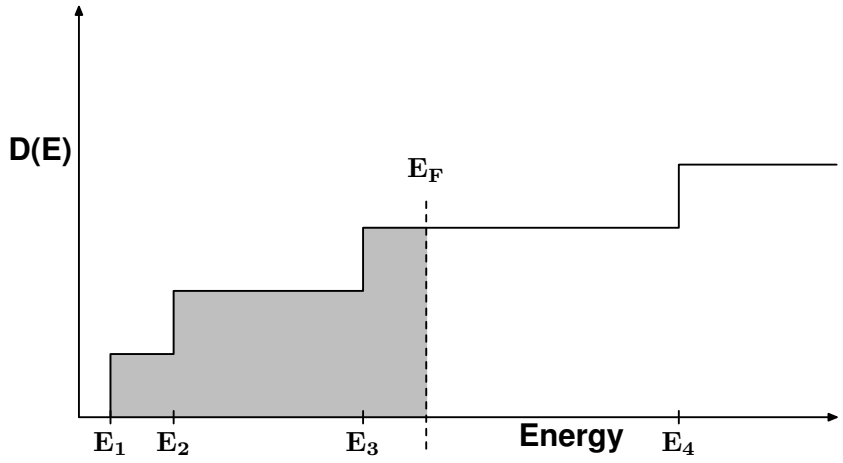

Figure 1.5: Density of states for a 2DEG as a function of energy. Every step of the staircase corresponds to a 2D subband. The shaded region are the states occupied in the ground-state ($T = 0$).

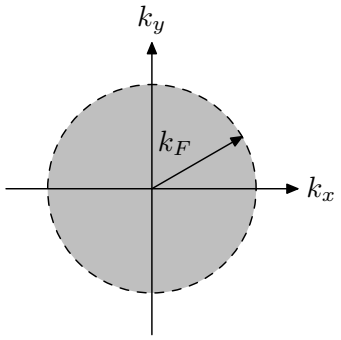

Figure 1.6: Fermi "sphere" for a 2DEG in equilibrium at $T = 0$. k_F is the *Fermi wavevector*: the states with $k \leq k_F$ are occupied, while the states with $k > k_F$ are empty.

The total number of electrons per unit area can be written as

$$n_{2\mathrm{d}} = \frac{m^*}{\pi\hbar^2}\int_0^\infty \Theta(E-E_1)\Theta(E_F-E)dE = \frac{m^*}{\pi\hbar^2}(E_F-E_1). \tag{1.11}$$

1.2.2 Electron gas: from 2D to 1D

If we also confine the electron gas along the y-direction, the new one-electron wavefunction is

$$\psi(\mathbf{r}) = \frac{1}{\sqrt{L_x}}\exp\left(\mathrm{i}k_x x\right)\chi_m(y)\phi_n(z), \tag{1.12}$$

where $\chi_m(y)$ corresponds to the quantized motion in the y-direction, and the energy of the electron is

$$E_{n,m,k} = E_n + E_m + \frac{\hbar^2 k_x^2}{2m^*}, \tag{1.13}$$

where E_m is the energy corresponding to $\chi_m(y)$. For each n, m pair of bound states, there is a continuum of states associated with free motion in the x-direction. For each 2D subband n, the DOS is now:

$$D_n(E) = \frac{1}{2\pi}\sqrt{\frac{2m^*}{\hbar^2}}\sum_m \frac{\Theta(E-E_n)}{\sqrt{E-E_m}}. \tag{1.14}$$

In Fig. 1.7 the total DOS is sketched for three occupied 1D subbands.

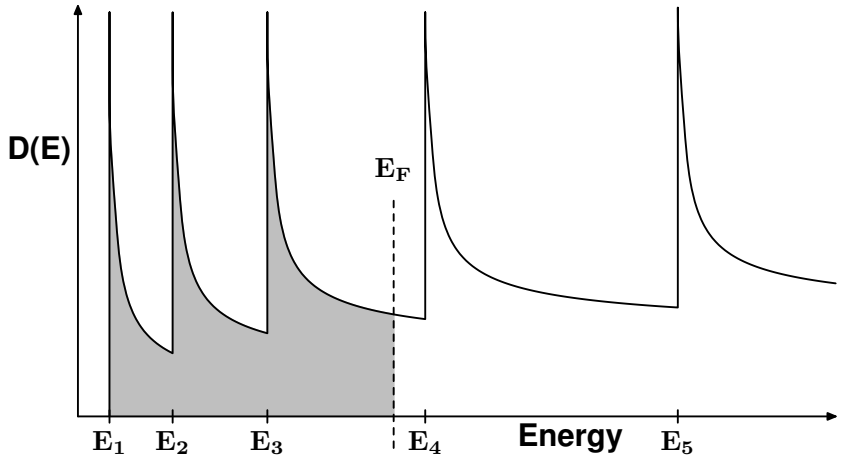

Figure 1.7: Density of states for a 1DEG as a function of energy (within one 2D subband). The shaded region are the states occupied in the ground-state. The effects of the divergences in E_m are usually not observed due to the broadening caused by disorder introduced in the fabrication process.

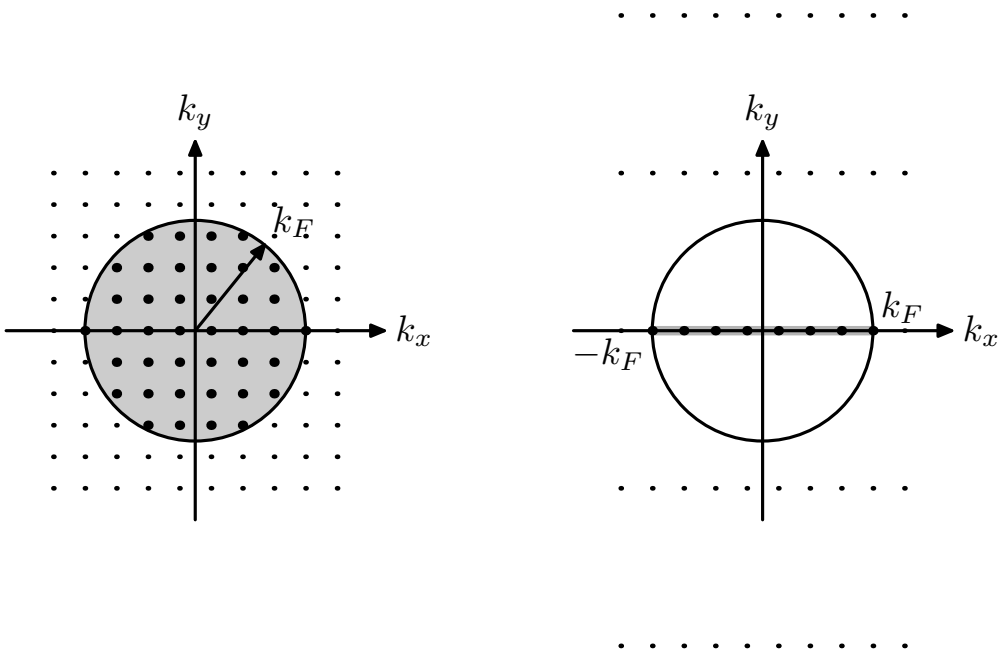

Figure 1.8: Fermi "sphere" for LDEGs in equilibrium at $T = 0$. On the left the Fermi circle for a 2DEG; on the right the Fermi "segment" for a 1DEG. The confinement along the y-direction changes the density of states, increasing the spacing Δk_y between adjacent states. When $\Delta k_y > k_F$, the condition $L_y < \lambda_F$ is satisfied and the system is 1D.

Figure 1.8 shows what happens to the Fermi circle in k-space. Each dot represents an available state: the spacing between the states depends on the boundary conditions, $\Delta k \sim 1/L$. When the electron gas is confined along the y-direction, the spacing Δk_y between the states increases. The motion of the electrons becomes quantized when $\Delta k_y \geq k_F$, which is equivalent to the condition $L_y \leq \lambda_F$.

1.2.3 2DEG in a magnetic field

Consider a 2DEG as described in Section 1.2.1 and let us apply a magnetic field perpendicular to its plane. The free translational motion in the plane is now impeded by the Lorentz force, which forces the electrons on *cyclotron orbits*. The motion in these orbits is harmonic in time. The consequence is that the energy spectrum is now completely quantized:

$$E_{n,l} = E_n + E_l = E_n + \left(l - \frac{1}{2}\right)\hbar\omega_c, \tag{1.15}$$

where $\omega_c = eB/m^*$ is the *cyclotron frequency*. The conditions for this quantization are that an electron does several orbits before being scattered, $\omega_c\tau > 1$ (where τ is

a scattering time), and that the thermal broadening of the Landau levels is small compared to their spacing, $k_B T \ll \hbar\omega_c$.

The energy levels E_l are known as *Landau levels* and, unlike the specific solutions of the Schrödinger equation, they do not depend on the choice of gauge. The spin degeneracy of each level is lifted in high magnetic fields by the Zeeman splitting (which adds the term $\pm sg\mu_B B$ to the energy). For each 2D subband n,

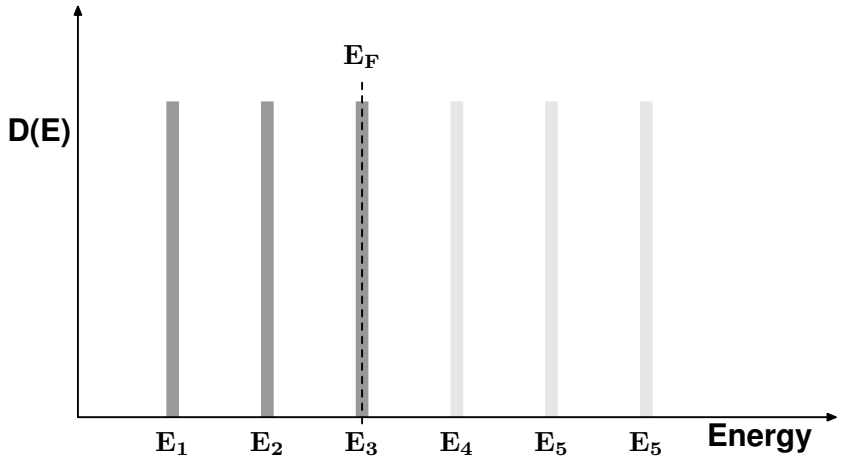

Figure 1.9: Density of states for a 2DEG in perpendicular magnetic field (Zeeman splitting has been neglected). The spacing between each level is given by $\Delta E = \hbar\omega_c \propto B$. The Fermi level E_F is shown pinned to the highest occupied Landau level.

the resulting DOS is

$$D(E) = \frac{2eB}{h} \sum_l \delta(E - E_l) \tag{1.16}$$

and is depicted in Fig. 1.9. Each Landau level has the degeneracy $2eB/h$ and the Fermi level "jumps" from one Landau level to the next when the magnetic field is varied. This leads to oscillations in the response of the 2DEG as a function of magnetic field (for example, *Shubnikov-de Haas oscillations* in the magnetoresistance). Typically the Landau levels are broadened by disorder.

What happens if we consider that the 2DEG is not infinite, but is constrained along the y-direction by an electric potential $U(y)$? It can be shown [18] that the energy of an electron becomes:

$$E_{n,l}(k_x) = E_n + \left(l - \frac{1}{2}\right)\hbar\omega_c^* + \frac{\hbar^2 k_x^2}{2M}, \tag{1.17}$$

where ω_c^* and M are a cyclotron frequency and an effective mass that depend on both the magnetic field and the potential $U(y)$. For each 2D subband we have

magneto-electric subbands, with Landau levels l that are no longer degenerate, but have the dispersion of a 1D system. In a classical picture, these states correspond to *skipping orbits*, where an electron "bounces" off the edges while moving in the x-direction.

By increasing the magnetic field, the states in the $+x$-direction are pushed towards one edge by the Lorentz force, while the states for motion in the $-x$-direction are pushed towards the opposite edge. The resulting *edge states* carrying current in opposite direction are spatially separated, which has a dramatic effect on the transport properties, as observed in the *Quantum Hall Effect* (QHE).

1.3 Diffusive transport in low-dimensional electron gases

If we restrict ourselves to the carrier transport parallel to the confining potentials, we can discuss homogeneous transport in a low-dimensional system in the same context as for bulk systems. We can apply the *semiclassical theory of transport* based on Boltzmann's transport equation, and describe the transport properties in terms of macroscopic phenomenological parameters such as mobility, conductivity, thermopower, *etc.* In the linear response regime it is possible to write these parameters in terms of the equilibrium properties of a LDEG. For a more detailed discussion see Refs. [19–22].

1.3.1 Semiclassical approach to transport

Assume that we can describe a LDEG in terms of a distribution function $f(\mathbf{r}, \mathbf{p}, t)$, where $\mathbf{r}$ is the position and $\mathbf{p}$ is the momentum of a particle. The number of particles that occupy a state at a time t within the volume $d\mathbf{r}d\mathbf{p}$ located at $(\mathbf{r}, \mathbf{p})$ in phase space is given by

$$f(\mathbf{r}, \mathbf{p}, t)d\mathbf{r}d\mathbf{p}. \tag{1.18}$$

Furthermore we assume that the following *semiclassical equations* are valid for the motion of a particle under the influence of an external electric field $\mathbf{F}$ (in the absence of a magnetic field):

$$\frac{d\mathbf{p}}{dt} = \frac{d(\hbar\mathbf{k})}{dt} = -e\mathbf{F}, \tag{1.19a}$$

$$\frac{d\mathbf{r}}{dt} = \mathbf{v}(\mathbf{k}) = \frac{1}{\hbar}\nabla_{\mathbf{k}} E_{\mathbf{k}}, \tag{1.19b}$$

where $E_{\mathbf{k}}$ is the energy of an electron with momentum $\mathbf{p} = \hbar\mathbf{k}$. Considering time scales longer than the mean free time between scattering events, the distribution function after a time interval δt will be

$$f(\mathbf{r} + \mathbf{v}\delta t, \mathbf{p} - e\mathbf{F}\delta t, t + \delta t) = f(\mathbf{r}, \mathbf{p}, t) + \left|\frac{\partial f}{\partial t}\right|_{coll} \delta t, \tag{1.20}$$

where $\left|\frac{\partial f}{\partial t}\right|_{coll}$ is the rate of change of the distribution function due to scattering. If both the external fields and the scattering are weak, we can treat them as separate perturbations of the equilibrium system. Expanding and re-arranging the terms

in Eq. (1.20), we can write a kinetic equation for the distribution function, the *Boltzmann transport equation*:

$$\frac{\partial f}{\partial t} = -\frac{1}{\hbar}\nabla_{\mathbf{k}} E_{\mathbf{k}} \cdot \nabla_{\mathbf{r}} f + \frac{e}{\hbar}\mathbf{F} \cdot \nabla_{\mathbf{k}} f + \left|\frac{\partial f}{\partial t}\right|_{coll}. \tag{1.21}$$

Assuming that the scattering events are instantaneous in time and space, and that they randomize the phase of the carrier (i.e., after a scattering event a particle is not correlated to other particles), we can write $\left|\frac{\partial f}{\partial t}\right|_{coll}$ as a detailed balance of in-scattering and out-scattering events and the *collision integral* becomes

$$\left|\frac{\partial f}{\partial t}\right|_{coll} = \int \frac{d\mathbf{k}'}{(2\pi)^d}\{\underbrace{S(\mathbf{k}', \mathbf{k})\left[f(\mathbf{k}')(1 - f(\mathbf{k}))\right]}_{\text{IN}} - \underbrace{S(\mathbf{k}, \mathbf{k}')\left[f(\mathbf{k})(1 - f(\mathbf{k}'))\right]}_{\text{OUT}}\}, \tag{1.22}$$

where $S(\mathbf{k}', \mathbf{k})$ is the scattering rate from state $\mathbf{k}'$ to state $\mathbf{k}$, d is the dimensionality of the system and the integral sums over all possible values of $\mathbf{k}'$.

If the system is in a steady state and close to equilibrium, we can use the *relaxation time approximation*:

$$\left|\frac{\partial f}{\partial t}\right|_{coll} = -\frac{f(\mathbf{k}) - f_0(E_{\mathbf{k}})}{\tau(E_{\mathbf{k}})}, \tag{1.23}$$

which means that the effect of scattering tends to bring the distribution function $f(\mathbf{k})$ back to its equilibrium form f_0 (the Fermi function) with some characteristic time scale $\tau(E_{\mathbf{k}})$. At this point, the non-equilibrium distribution function for a homogeneous system ($\nabla_{\mathbf{r}} f = 0$) in a steady state ($\partial f/\partial t = 0$) can be written as

$$f(\mathbf{k}) = f_0(E_{\mathbf{k}}) + \tau(E_{\mathbf{k}}) e\mathbf{F} \cdot \mathbf{v}(\mathbf{k}) \frac{\partial f_0}{\partial E}(E_{\mathbf{k}}). \tag{1.24}$$

We can use this result to calculate, for example, the current density:

$$\begin{aligned}
\mathbf{J} &= -e \int \frac{d\mathbf{k}'}{(2\pi)^d} \mathbf{v}(\mathbf{k}) f(\mathbf{k}) \\
&= -e \int \frac{d\mathbf{k}'}{(2\pi)^d} \mathbf{v}(\mathbf{k}) \left(\tau(E_{\mathbf{k}})\ e\mathbf{F} \cdot \mathbf{v}(\mathbf{k}) \frac{\partial f_0}{\partial E}(E_{\mathbf{k}})\right) \\
&= -e^2 \int_0^\infty dE\ D(E)\ \tau(E)\ \mathbf{v}(E)\left(\mathbf{v}(E) \cdot \mathbf{F}\right) \frac{\partial f_0}{\partial E}(E),
\end{aligned} \tag{1.25}$$

where the integral over $\mathbf{k}$ has been converted into an integral over E. Factoring

out the electric field $\mathbf{F}$ and the carrier density n, Eq. (1.25) becomes

$$\mathbf{J} = -e^2 n \left\{ \frac{\int_0^\infty dE\ D(E)\ \tau(E)\ v_{\mathbf{F}}^2(E) \dfrac{\partial f_0}{\partial E}(E)}{\int_0^\infty dE\ D(E)\ f_0(E)} \right\} \cdot \mathbf{F}, \tag{1.26}$$

where $v_{\mathbf{F}}$ is the component of $\mathbf{v}$ along the electric field. The term in braces can be written as $-\dfrac{\langle\tau\rangle}{m}$ and thus:

$$\mathbf{J} = \frac{e^2 n \langle\tau\rangle}{m}\mathbf{F} = en\mu\mathbf{F}, \tag{1.27}$$

where $\mu = \dfrac{e\langle\tau\rangle}{m}$ is the mobility. In the degenerate limit, $\langle\tau\rangle \approx \tau(E = E_F)$, showing that the transport properties of the LDEG are determined by the DOS at the Fermi level. Other physical properties, such as conductivity or thermopower, can be related to the relaxation time $\langle\tau\rangle$ by the same procedure.

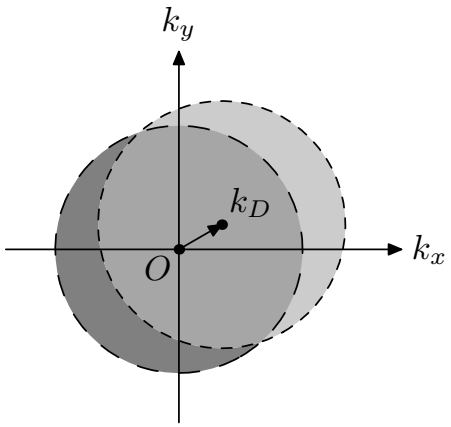

Figure 1.10: Fermi circle for a 2DEG in a small electric field. The out-of-equilibrium Fermi circle is shifted with respect to the equilibrium Fermi circle by $\mathbf{k}_D$, the wavevector corresponding to the drift velocity $\mathbf{v}_D$. Electrons occupying states in the light-grey area tend to scatter into states in the dark-grey area. Electrons in the states in the medium-grey area cannot scatter, and have no influence on the transport properties.

For a 2DEG there is a good picture that illustrates what happens to the distribution function when an uniform electric field is applied, and we examine the linear response in a steady state. The distribution function becomes:

$$f(\mathbf{k}) = f_0(\mathbf{k} - \mathbf{k}_D), \tag{1.28}$$

where $\mathbf{k}_D$ is the wavevector corresponding to the *drift velocity* $\mathbf{v}_D = \mu\mathbf{F}$. In k-space this distribution function is simply the equilibrium Fermi circle shifted from the origin by a vector $\mathbf{k}_D = \frac{m}{\hbar}\mathbf{v}_D$, as depicted in Fig. 1.10.

All the information about the scattering mechanisms that affect the transport properties of the LDEG is contained in the relaxation time τ. If there is more than one scattering process, and the processes are independent from each other, the total scattering time is given by *Mathiessen's rule*:

$$\frac{1}{\tau} = \sum_j \frac{1}{\tau_j}. \tag{1.29}$$

1.3.2 Scattering mechanisms

For a 2DEG in a GaAs/AlGaAs heterostructure there are several possible scattering mechanisms. In addition to those normally present in bulk GaAs (bulk phonon scattering, background impurities, inter-subband scattering), there are mechanisms specific to the heterojunction structures (remote ionized impurities, interface phonons, interface roughness). Although many mechanisms are possible in principle [5, 23], only a few determine the mobility of the 2DEG:

1. Coulomb scattering from remote and background ionized impurities;
2. interaction with bulk acoustic and optical phonons.

Coulomb scattering

Coulomb scattering is due to the presence of ionized impurities in the nominally undoped GaAs (called *background impurities*), and the ionized dopants in the doped AlGaAs layer (called *remote impurities*). Although the density of remote impurities is higher, their distance from the electron gas makes them less effective scatterers than the background impurities.

The impurities interact with the electrons via the Coulomb interaction. This mechanism dominates the momentum relaxation of the electrons at low temperatures, providing a temperature-independent mobility. However, since the scattering is elastic, it does not contribute to the energy relaxation of the electrons.

Phonon scattering

One can distinguish three regimes for phonon scattering, depending on the temperature [24]:

- *Inelastic regime* for $T \gtrsim 40$ K.
- *Equipartition regime* for $4\text{ K} \lesssim T \lesssim 40$ K.
- *Bloch-Grüneisen regime* for $T \lesssim 4$ K.

In the inelastic regime the electrons scatter from optical phonons via the Fröhlich interaction. In a polar crystal an optical phonon changes the separation between positive and negative ions. This changes the polarization field which affects the electrons. The energy scale for this interaction is given by $\hbar\omega_{opt} \gtrsim E_F$. At low temperatures ($k_B T \ll \hbar\omega_{opt}$) optical phonons are "frozen" and do not contribute to the scattering.

In both the equipartition regime and the Bloch-Grüneisen regime, the electron-phonon interaction is dominated by acoustic phonons. The electron-phonon coupling is of two types:

1. *Deformation potential* (DP): the local deformation of the lattice due to acoustic phonons shifts the band-edges of the GaAs.
2. *Piezoelectric coupling* (PZ): acoustic phonons deform the lattice in a polar material, changing the polarization field.

The energy scale for both couplings is set by $\hbar\omega_{max} \approx 2\hbar u_s k_F$ (where u_s is the speed of sound), and the scattering can be considered quasi-elastic.[3]

In the equipartition regime $k_B T \gg \hbar\omega_{max}$ and the Bose occupation factor for the phonons is approximately linear in temperature. The experiments presented in this work were performed at low temperatures, where $k_B T \approx \hbar\omega_{max}$ and the system is in the Bloch-Grüneisen regime. There is a small number of phonons (which depends exponentially on temperature) and the electron gas is strongly degenerate. Both these factors lead to a drastic reduction of the electron-phonon scattering. Figure 1.11 shows the electron mobility in GaAs/AlGaAs heterostructures as a function of temperature. The contribution of the different scattering mechanisms are shown, as well as the total mobility which is obtained using Mathiessen's rule (1.29).

[3]The speed of sound u_s is much lower than the speed of the electrons at the Fermi surface $v_F = \frac{\hbar k_F}{m}$. That means that $\hbar u_s k_F \ll \hbar v_F k_F = \dfrac{\hbar^2 k_F^2}{m} = 2E_F$ and therefore $\hbar\omega_{max} \ll E_F$.

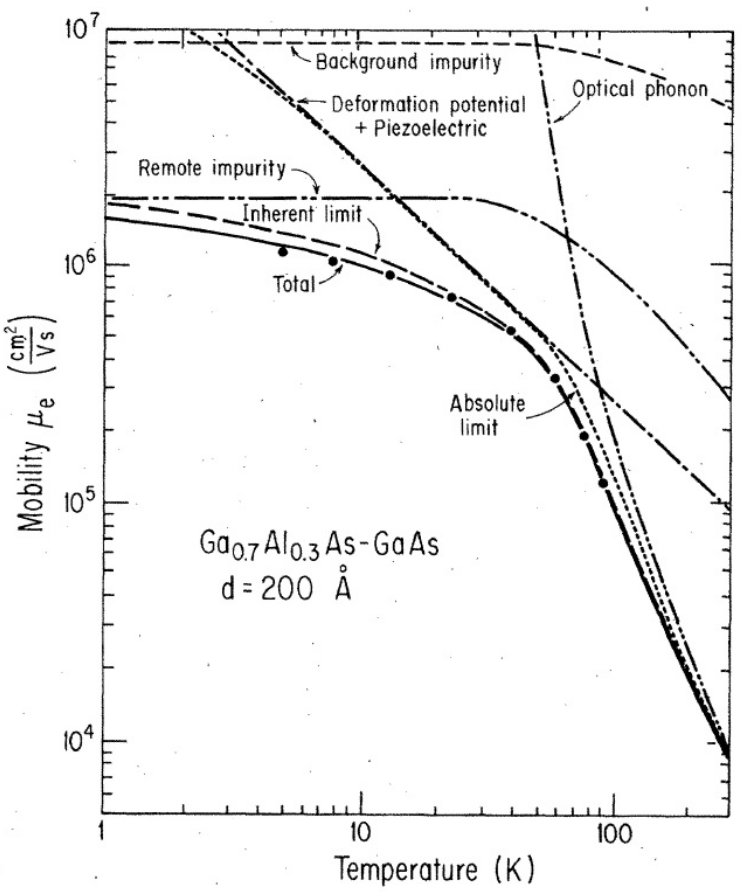

Figure 1.11: Temperature dependence of the electron mobility in GaAs/AlGaAs heterostructures, from [25]. Points are experimental data, curves are calculated mobilities. In the limit of low temperatures, the mobility is determined by scattering with ionized impurities.

Bibliography

[1] L. D. Landau and E. M. Lifshitz, *Quantum Mechanics. Non-Relativistic Theory* (Pergamon Press, London, 1958).

[2] R. Eisberg and R. Resnick, *Quantum Physics of Atoms, Molecules, Solids, Nuclei, and Particles* (Wiley, New York, 1985).

[3] V. N. Lutskii, *Phys. Stat. Sol. A* **1**, 199 (1970).

[4] T. Ando, A. B. Fowler, and F. Stern, *Rev. Mod. Phys.* **54**, 437 (1982).

[5] J. J. Harris, J. A. Pals, and R. Woltjer, *Rep. Prog. Phys.* **52**, 1217 (1989).

[6] C. W. J. Beenakker and H. van Houten, *Solid State Physics* **44**, 1 (1991).

[7] S. Datta, *Electronic Transport in Mesoscopic Systems* (Cambridge University Press, Cambridge, 1995).

[8] D. K. Ferry and S. M. Goodnick, *Transport in Nanostructures* (Cambridge University Press, Cambridge, 1997).

[9] J. H. Davies, *The Physics of Low-Dimensional Semiconductors. An Introduction* (Cambridge University Press, Cambridge, 1998).

[10] R. Dingle, H. L. Störmer, A. C. Gossard, and W. Wiegmann, *Appl. Phys. Lett.* **33**, 665 (1978).

[11] M. J. Kelly and R. J. Nicholas, *Rep. Prog. Phys.* **48**, 1699 (1985).

[12] M. J. Kelly, *Low-dimensional semiconductors: materials, physics, technology, devices* (Oxford University Press, Oxford, 1995).

[13] S. M. Sze, *Physics of Semiconductor Devices* (Wiley, New York, 1981).

[14] W. J. Skocpol, L. D. Jackel, E. L. Hu, R. E. Howard, and L. A. Fetter, *Phys. Rev. Lett.* **49**, 951 (1982).

[15] H. van Houten, B. J. van Wees, M. G. J. Heijman, and J. P. André, *Appl. Phys. Lett.* **49**, 1781 (1986).

[16] A. Kristensen, J. Bo Jensen, M. Zaffalon, C. B. Sørensen, S. M. Reimann, P. E. Lindelof, M. Michel, and A. Forchel, *J. Appl. Phys.* **83**, 607 (1998).

[17] T. J. Thornton, M. Pepper, H. Ahmed, D. Andrews, and G. J. Davies, *Phys. Rev. Lett.* **56**, 1198 (1986).

[18] K.-F. Berggren, G. Roos, and H. van Houten, *Phys. Rev. B* **37**, 10118 (1988).

[19] J. M. Ziman, *Electrons And Phonons. The Theory of Transport Phenomena in Solids* (Oxford University Press, Oxford, 1963).

[20] N. W. Ashcroft and N. D. Mermin, *Solid State Physics* (Saunders College Publishing, 1976).

[21] C. Kittel, *Introduction to Solid State Physics* (Wiley, New York, 1996).

[22] K. Huang, *Statistical Mechanics* (Wiley, New York, 1987).

[23] B. K. Ridley, *Rep. Prog. Phys.* **54**, 169 (1991).

[24] T. Kawamura and S. D. Sarma, *Phys. Rev. B* **45**, 3612 (1992).

[25] W. Walukiewicz, H. E. Ruda, J. Lagowski, and H. C. Gatos, *Phys. Rev. B* **30**, 4571 (1984).

Chapter 2

Ballistic conduction through one-dimensional constrictions

In the previous chapter we have seen the effect of confinement on the equilibrium properties of an electron gas. We have also seen that transport parallel to the confining potentials can be described by the semiclassical theory of transport. Quantum effects enter only through the description of the bound states arising from the confinement, and the phase information of the particles is ignored due to *ensemble* averaging. In structures too small for *ensemble* averaging, quantum interference affects the transport properties, leading to effects like *universal conductance fluctuations* and *weak localization* [1, 2].

One of the assumptions underlying the semiclassical transport theory is to look at the system over time scales that are much longer than the average scattering time $\langle\tau\rangle$. What happens if the size of the sample is comparable or smaller than the average distance between scattering events? The transport properties are no longer determined by the scattering from impurities, but by the scattering at the sample boundaries, which means that the transport depends on the geometry of the sample. This regime is called *ballistic transport*.

The dependence of the transport properties on the geometry of the sample is analogous to electromagnetic waveguides. The approach of treating conductors as *electron waveguides* was introduced by Landauer [3], and has lead to the development of the *Landauer-Büttiker formalism* [4], which relates mesoscopic transport to the transmission and reflection probabilities of the electrons [5]. Although the earliest applications of Landauer's approach were to tunneling junctions, the formalism has been successfully applied to ballistic conductors.

The prime example of such ballistic conductors are the *split-gate devices* [6–8],

which use the split-gate technique to form a constriction in a 2DEG. At low temperatures the transport through the constriction can be ballistic, and a *one-dimensional ballistic conductor* is obtained. The transport properties of such devices have been successfully described within the Landauer-Büttiker formalism.

In this chapter we introduce ballistic transport, and point out the main differences from diffusive transport. The Landauer-Büttiker formalism will be outlined, and then we will see how one-dimensional constrictions in a 2DEG behave as ballistic conductors. Finally we will present the conductance anomaly in 1D constrictions known as the *0.7 structure*.

2.1 Ballistic transport

The *Fermi wavelength* is the length scale which determines whether an electron gas is confined or not. It is possible to define other length scales which are characteristic of a LDEG and which determine the regime of electronic transport. When the size of the conductor is comparable to one of these length scales, the conductor is usually called *mesoscopic* (because it is "between" the *microscopic* and *macroscopic*). In this case macroscopic properties, such as conductivity, are insufficient to fully describe the transport. For a review see Refs. [1, 2].

2.1.1 Characteristic length scales in a 2DEG

In Section 1.3 the average scattering time $\tau_m = \langle\tau\rangle$ was introduced. This is the average time interval necessary for an electron to change its momentum due to scattering, and is also called *momentum-relaxation time*. The length scale associated with this time is the *mean free path*:

$$L_e = v_F \tau_m, \tag{2.1}$$

where v_F is the Fermi velocity of the electrons. The mean free path is the average distance an electron travels before its initial momentum is destroyed. It is this length scale that determines whether transport is ballistic or diffusive. If the length of a conductor is smaller than the mean free path, the electrons pass through without being scattered (hence the term "ballistic"). The only source of scattering are the boundaries, and so in the ballistic regime the geometry of the conductor becomes important. For a 2DEG with electron density $n = 2 \times 10^{11}$ cm^{-2} and mobility $\mu = 2 \times 10^6$ cm/Vs, $\tau_m \approx 76$ ps and $L_e \approx 15$ µm. Modern lithographic techniques can fabricate structures with lengths below 1 µm.

The length scale which tells us whether quantum interference effects are important is the *phase-relaxation length* L_φ. Similar to the mean free path, the phase-relaxation length is usually defined in terms of the *phase-relaxation time* τ_φ, which is the average time for an electron to lose its initial phase:

$$L_\varphi = \sqrt{D\tau_\varphi}, \tag{2.2}$$

where D is the diffusion coefficient. When this length is determined by inelastic processes, the phase-relaxation length is sometimes called *inelastic mean free path* (as opposed to the *elastic* mean free path L_e). In high-mobility GaAs/AlGaAs

heterostructures at low temperatures, the phase-relaxation length is given by $L_\varphi = v_F \tau_\varphi$, where v_F is the Fermi velocity of the electrons and τ_φ is determined by the electron-electron scattering time τ_{ee}[1]. For a 2DEG with electron density $n = 2 \times 10^{11}$ cm^{-2} and mobility $\mu = 2 \times 10^6$ cm/Vs, $v_F \approx 2 \times 10^5$ m/s and $\tau_\varphi \sim \tau_{ee} \approx 100$ fs, which gives $L_\varphi \approx 20$ nm.

We have seen that a magnetic field changes the spectrum of a 2DEG at low temperatures, with the formation of discrete energy levels. It is possible to associate a length scale to the Landau levels, the *magnetic length*:

$$L_B = \sqrt{\frac{\hbar}{eB}}. \tag{2.3}$$

This length scale gives the spatial extent of the wave function that corresponds to the lowest Landau level. At $B = 1$ T $L_B \approx 26$ nm.

2.1.2 From diffusive to ballistic transport regime

Figure 2.1 presents a depiction of the three possible transport regimes for a constriction defined in a 2DEG. In the *diffusive regime* both the length L and the width W of the constriction are much greater than the mean free path L_e of the electrons. The transport properties at low temperatures are determined by impurity scattering and can be expressed in terms of local quantities such as mobility μ or conductivity σ, which are well defined in this regime. The semiclassical approach described in the previous chapter is appropriate to describe the transport. Quantum interference effects are important if the size of the constriction is comparable to the phase-relaxation length, as it is possible for low-mobility semiconductors. As long as both the mean free path and the phase-relaxation length are small, the conductor can be considered as a portion of 2DEG.

If the width of the constriction W is smaller than the mean free path L_e, but the length L is larger, the regime is called *quasi-ballistic*. In this case both internal impurity scattering and boundary scattering are important to the transport properties. This is an intermediate regime between diffusive and ballistic, showing some of the size effects which have a more dramatic effect on transport in the ballistic regime (such as the edge states mentioned Section 1.2.3).

The transport is in the *ballistic regime* if both the length L and the width W of the conductor are much smaller than the mean free path L_e. Now the scattering

[1]Electron-electron interactions do not affect the momentum-relaxation time and the elastic mean free path.

is dominated by the boundaries of the constrictions[2], and the transport properties cannot be expressed in terms of local quantities but depend on the geometry of the conductor. This dependence on the sample geometry is analogous to electromagnetic wave guides. So, as opposed to the diffusive regime where the conductance of the sample can be written as $G = (W/L)\sigma$ (where σ is the conductivity), the conductance can be expressed in terms of *transmission probability* T of the electron wave-guide: $G = (e^2/h)T$, which is the essence of the Landauer approach to transport in small structures.

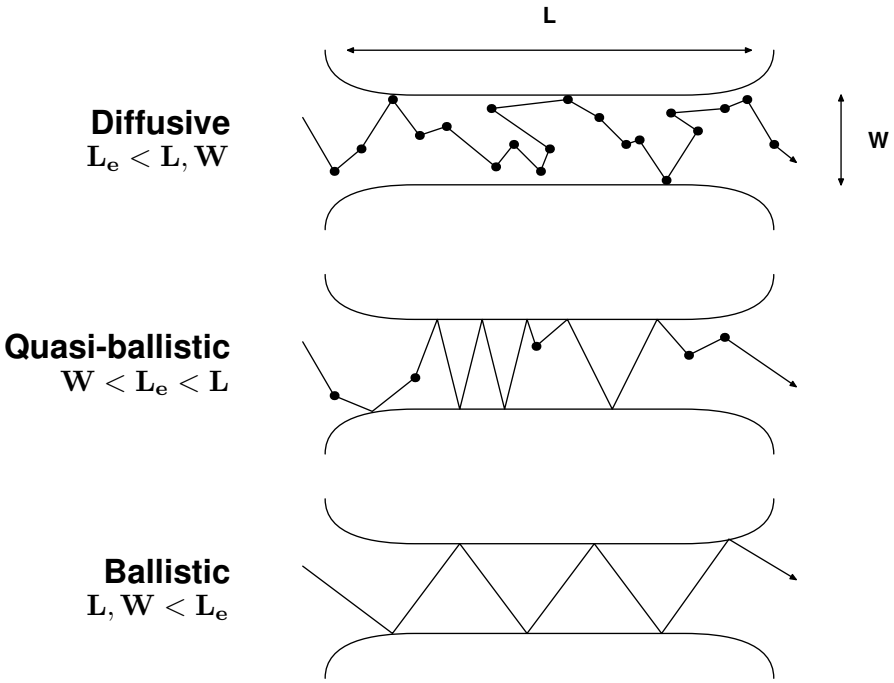

Figure 2.1: Three possible regimes for the transport in a 1D conductor defined by a constriction in a 2DEG, from Ref. [1]. L and W are the length and the width of the constriction, L_e is the mean free path of the charge carriers. In the ballistic regime the momentum of the carrier parallel to the axis of the conductor is conserved. The scattering at the boundaries of the constriction is depicted as specular (which is a good approximation for a constriction defined electrostatically).

[2]Boundary scattering has two limiting case: *diffuse scattering*, where the momentum of a carrier is completely randomized after a scattering event; *specular scattering*, where the component of the momentum parallel to the axis of the channel is conserved. Specular scattering is typical for electrostatically defined constrictions.

2.2 Landauer-Büttiker formalism

Landauer [3, 9] proposed an approach where the current through a conductor is expressed in terms of the probability that an electron is transmitted. He provided a formula for the linear response conductance G of a one-dimensional conductor with a single channel. Fisher and Lee [10] extended the *Landauer formula* to a multi-channel conductor and showed that it could be derived from the Kubo formula, via the scattering matrix. Engquist and Anderson [11] stressed the need to consider the actual conditions corresponding to the measurements, and Imry [12] clarified the concept of *contact resistance*. Büttiker *et al.* [13] extended Landauer's approach to devices with multiple reservoirs and non-zero magnetic fields. For more details, see Refs. [2, 5, 14].

2.2.1 Landauer formula

Consider the 1D conductor in Fig. 2.2, where a scattering region S is connected to reservoirs (*left* and *right*) by leads. For simplicity we assume that the leads are ideal (i.e., without scattering) and that only one 1D subband is occupied. Each reservoir has a distribution of electrons given by the Fermi function (with chemical potential μ_L and μ_R, respectively). All the inelastic scattering is assumed to occur in these reservoirs, which means that the phase of the electrons injected or absorbed by them is randomized. The flow of electrons from one reservoir to the other can be described using *incident* (I), *reflected* (R) and *transmitted* (T) flux. The flux can be written in term of a *transmission probability* $t(E)$, which is a function of energy.

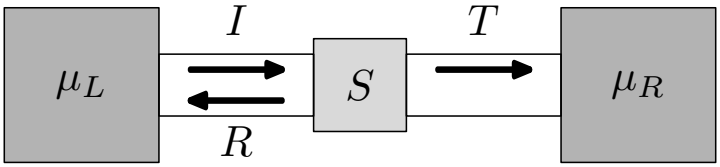

Figure 2.2: Example of two-terminal device. A scatterer S is connected to two reservoirs by ideal leads. The two reservoirs are characterized by their chemical potentials μ_L and μ_R. I, R and T are the incident, reflected and transmitted component of the electron flux.

If we apply a small potential difference V between the two reservoirs, such that

$eV = \mu_L - \mu_R \ll \mu_L, \mu_R$, the current flowing from left to right is:

$$\begin{aligned} I \;=\; & e \int_0^\infty D(E)\; f_0(E, \mu_L)\; v(E)\; t(E)\; dE \;- \\ & - e \int_0^\infty D(E)\; f_0(E, \mu_R)\; v(E)\; t(E)\; dE, \end{aligned} \tag{2.4}$$

where $D(E)$ is the DOS in the leads, $f_0(E, \mu)$ is the Fermi function for the reservoirs ($D(E) f_0(E, \mu)$ gives the number of electrons), $v(E)$ is the velocity and $t(E)$ is the transmission probability. In 1D $D(E) = \dfrac{1}{h}\sqrt{2m^*/E}$ (from Eq. (1.14)) and $v(E) = \sqrt{2E/m^*}$ (from Eq. (1.19b)), so $D(E)v(E) = \dfrac{1}{h}$. Equation (2.4) at low temperatures becomes then

$$\begin{aligned} I &= e \int_0^{\mu_L} D(E)\; v(E)\; t(E)\; dE - e \int_0^{\mu_R} D(E)\; v(E)\; t(E)\; dE \\ &= 2e \frac{1}{h} \int_{\mu_R}^{\mu_L} t(E)\; dE \\ &= \frac{2e}{h}\; t(\mu)\; (\mu_L - \mu_R) = \frac{2e^2}{h}\; t(\mu) V, \end{aligned} \tag{2.5}$$

where a factor 2 accounts for spin-degeneracy and it has been assumed that $t(E)$ is nearly constant over the range between μ_L and μ_R. $t(\mu)$ is the transmission probability of the scatterer S at the average chemical potential, $\mu = \dfrac{\mu_L + \mu_R}{2}$. The conductance of a single-channel 1D conductor with transmission probability $T = t(\mu)$ is then:

$$G = \frac{I}{V} = \frac{2e^2}{h} T, \tag{2.6}$$

which is known as the two-terminal *Landauer formula*.

If transport is ballistic, $T \to 1$ and $G = \dfrac{2e^2}{h}$. This result seems contradictory because we obtain a finite conductance (and hence, finite resistance) for a conductor when there is no scattering. Eq. (2.6) was derived by considering the current flowing from one reservoir into the other, through the conductor. Since the conductor has only a few transmitting modes, the electrons are "squeezed" though the conductor. It is the fact that the current has to go through a narrow channel that gives a finite resistance (*contact resistance*), even if the channel itself is ballistic.

2.3 Split-gate devices as one-dimensional ballistic conductors

The split-gate technique [6] was presented in the previous chapter as a method to produce low-dimensional systems in a semiconductor heterostructure. Figure 2.3 is a schematic representation of such a split-gate: by applying a negative voltage to the gates, a constriction is formed in the 2DEG. If the width of the constriction is small enough, it forms a one-dimensional conductor that connects two regions of 2DEG (it is also known as *quantum point contact*, QPC). At low temperatures, the mean free path of the electrons can be much larger than the length of the constriction, and so the transport is ballistic.

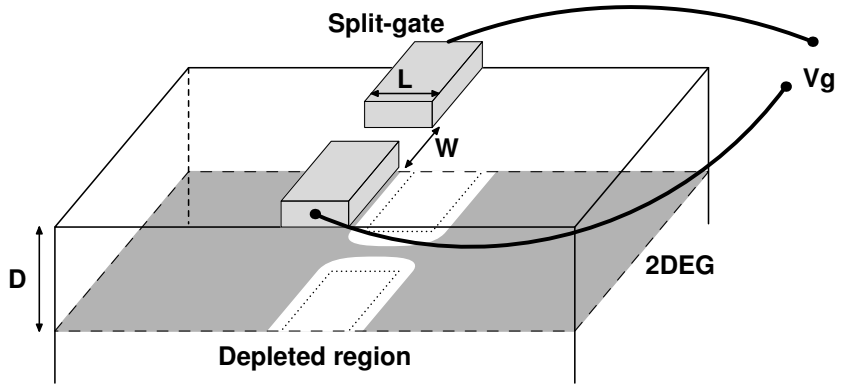

Figure 2.3: Schematic representation of a split-gate device. L and W are the lithographic length and width of the gap between the gates. D is the depth of the 2DEG. Applying a negative voltage V_g to the split-gate, the regions of the 2DEG beneath the gates are depleted and a narrow channel is left, which connects the two sides of the 2DEG.

In 1988 van Wees *et al.* [7] and Wharam *et al.* [8] independently reported measurements of the conductance versus gate voltage in split-gate structures. The measurements showed plateaux in the conductance quantized in integer multiples of $2e^2/h$. The data can be interpreted in terms of Landauer-Büttiker formalism for a two-terminal device. For a ballistic conductor in the absence of a magnetic field:

$$G = \frac{2e^2}{h} N, \tag{2.7}$$

where N is the number of transmitting channels in the 1D conductor. In a split-gate device the number of transmitting 1D subbands varies with gate voltage V_g. The more negative V_g, the narrower the constriction, and the lower the electron density. As the 1D subbands are depopulated with decreasing V_g, G decreases by

steps of $\frac{2e^2}{h}$, and the resulting $G(V_g)$ characteristic looks like in Fig.2.4.

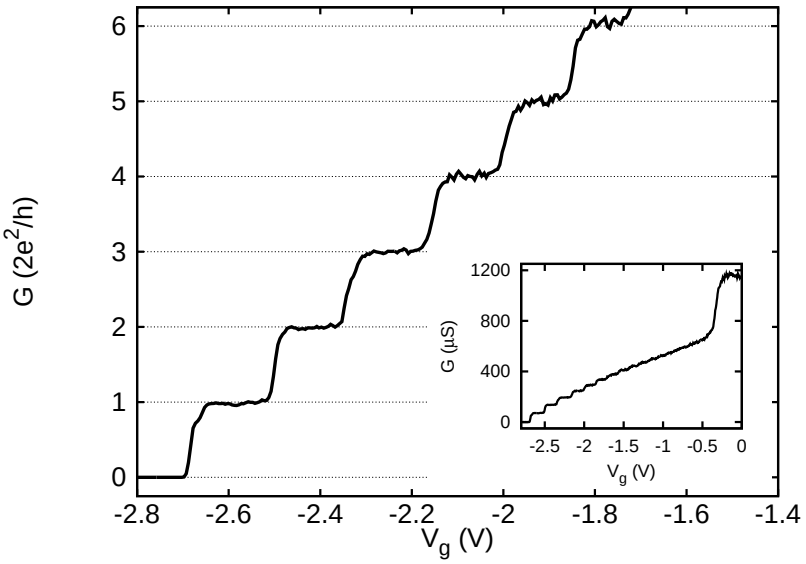

Figure 2.4: Conductance characteristic $G(V_g)$ as a function of gate voltage V_g of a split-gate device (split-gate B in sample III), at $T \approx 50$ mK.
The conductance has been corrected for a series resistance of 840 Ω, which is due to the regions of 2DEG that connect the constriction to the electric leads. The inset shows the overall characteristic.

A realistic model for the potential profile in a split-gate device is given by the *saddle-point potential* [15, 16]:

$$V(x,y) = V_0 - \frac{1}{2}m^*\omega_x^2 x^2 + \frac{1}{2}m^*\omega_y^2 y^2, \tag{2.8}$$

where (x, y) are the coordinates in the plane of the 2DEG, V_0 is the potential at the center of the saddle, m^* is the effective mass of the electrons, and ω_x and ω_y are parameters that characterize the potential (curvatures). The "y-part" of Eq. (2.8) describes the confining potential of the constriction in the 2DEG, and $\hbar\omega_y$ gives the energy spacing between the 1D subbands. The "x-part" gives the shape of a potential barrier, which allows for tunneling through the constriction even when a subband is not fully transmitting. The transmission probabilities are given by [16]

$$t_{mn} = \delta_{mn}\frac{1}{1+\exp(-\pi\epsilon_n)}, \tag{2.9}$$

where δ_{mn} is the Kronecker delta and $\epsilon_n = \frac{2}{\hbar\omega_x}\left(E - \hbar\omega_y(n+\frac{1}{2}) - V_0\right)$ is a dimensionless measure of the energy E. The resulting transmission is plotted in Fig. 2.5, and one can see the similarity with the conductance in Fig. 2.4.

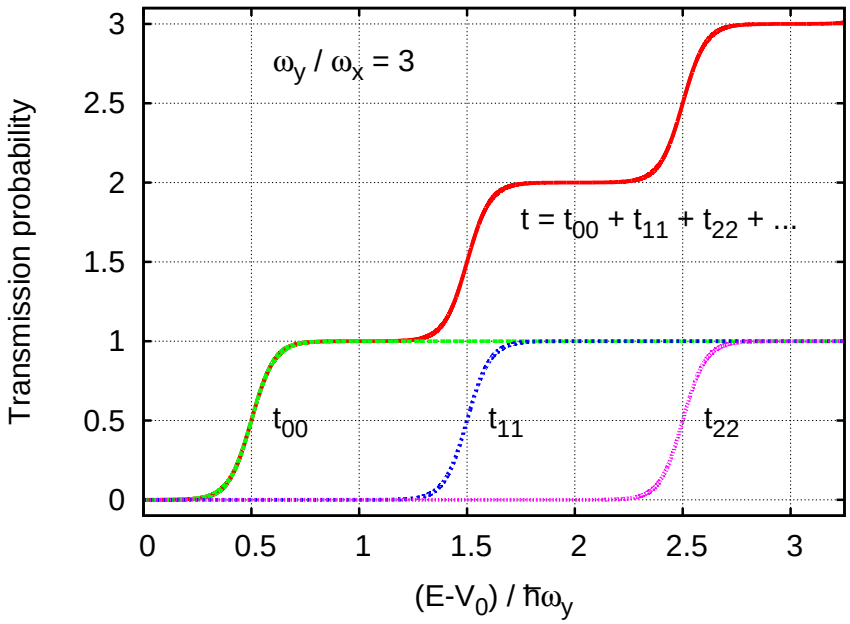

Figure 2.5: Transmission probability of a saddle-point potential with $\hbar\omega_x = 1$ meV and $\hbar\omega_y = 3$ meV. t_{00}, t_{11}, t_{22} are the transmission probabilities of single subbands as a function of energy, t is the sum of the transmission probabilities of all subbands.

2.3.1 The "0.7 structure"

The *0.7 structure* is a shoulder-like feature observed in the electrical conductance at $G \approx 0.7(2e^2/h)$, as can be seen in Fig. 2.6. The exact height and shape depends on temperature and electron density. In 1996 Thomas *et al.* [17] showed that the 0.7 structure is an intrinsic property of a 1D constriction. Further work determined several properties of the 0.7 structure:

- The 0.7 structure becomes stronger with increasing temperature [17]. From a shoulder-like feature at $G \approx 0.7(2e^2/h)$ it evolves into a plateau-like feature at $G \approx 0.6(2e^2/h)$, as shown in Fig. 2.6. Such a change in conductance is not observed in the regular quantized plateaux, and the 0.7 structure is still present at temperatures where the regular plateaux are thermally smeared.

- As the magnetic field is increased, the 0.7 structure evolves continuously into the spin-split plateau at e^2/h [17]. Features analogous to the 0.7 structure are observed for higher subbands (e.g., at $\sim 1.7(2e^2/h)$ and $\sim 2.7(2e^2/h)$), which evolve into spin-split plateaux with increasing magnetic field ("0.7 analogues") [18, 19]. As the temperature is increased, the e^2/h spin-split plateau increases towards $\sim 0.6 \times (2e^2/h)$ [20].

- With decreasing electron density the 0.7 structure becomes more marked and moves towards e^2/h [18, 19]. As the temperature is increased, the feature at $\sim e^2/h$ moves towards $\sim 0.6(2e^2/h)$.

- Measurements of the non-linear conductance $G(V_{sd})$ (where V_{sd} is the source-drain bias) show that the 0.7 structure evolves into a plateau-like structure at $\sim 0.85(2e^2/h)$ [18, 19]. An additional feature at $\sim 0.3(2e^2/h)$ appears to evolve from the 0.7 structure (first observed in Refs. [21, 22]).

The 0.7 structure is not due to an impurity or a resonance in the constriction, because it would become weaker with increasing temperature.[3] The magnetic field dependence indicates that the 0.7 structure is related to the spin. The fact that the 0.7 structure becomes stronger with decreasing electron density, and that the g-factor is higher for the lower subbands than for the bulk 2DEG [17, 18], as shown in Fig. 2.7 on page 43, points towards the exchange interaction as important mechanism in the 0.7 structure. These considerations lead Thomas *et al.* to

[3] Figure 2.6 shows an impurity feature (marked with a star). It becomes weaker with increasing temperature; in contrast the 0.7 structure becomes stronger.

interpret the 0.7 structure as a spontaneous spin polarization due to electron-electron interactions.

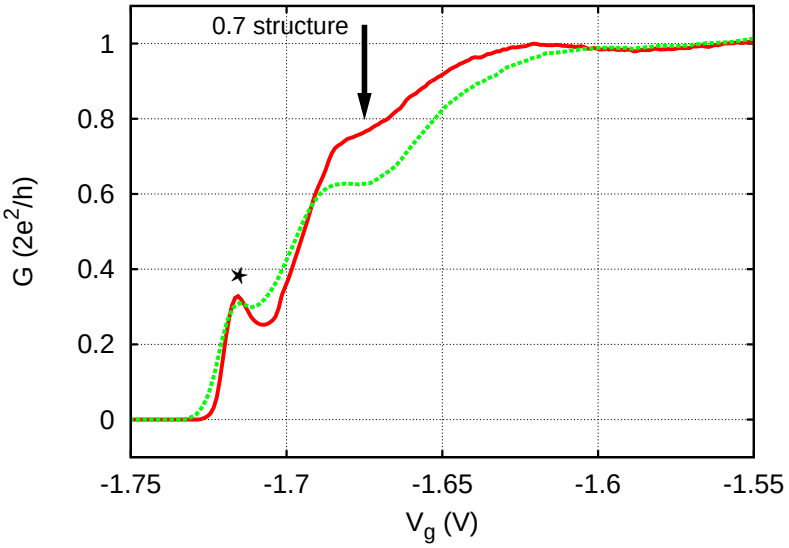

Figure 2.6: The 0.7 structure in the electrical conductance $G(V_g)$ (split-gate A in sample I), measured at $T \approx 0.3$ K (full red) and at $T \approx 1.2$ K (dashed green). The black arrow indicates the 0.7 structure: at $T \approx 0.3$ K it is observed as a shoulder at $G \approx 0.75(2e^2/h)$, which evolves into a plateau-like structure at $G \approx 0.63(2e^2/h)$ at $T \approx 1.2$ K. The star (*) marks a feature due to an impurity (see Sec. 5.2.4).

Spontaneous spin polarization

Lieb and Mattis [23] proved that the ground-state of an infinite 1D conductor cannot be spin-polarized. However, the theorem might not be applicable to split-gate devices, because the constriction has a finite width and a finite length, and so it is not strictly 1D. Wang and Berggren [24] showed that exchange interactions in a *quasi*-1D conductor result in a spontaneous spin polarization. The saddle-point potential in the constriction has a different height for spin-up and spin-down electrons, so that when $G \leq 2e^2/h$ only one spin is fully transmitted, but the other has to tunnel. However, this theory agrees only qualitatively with the measurements, and in particular does not explain the temperature dependence.

Further confirmation of the 0.7 structure came from Kristensen *et al.* [25, 26], who showed that the temperature dependence and the source-drain bias measurements of shallow-etched constrictions give the same results as split-gate devices,

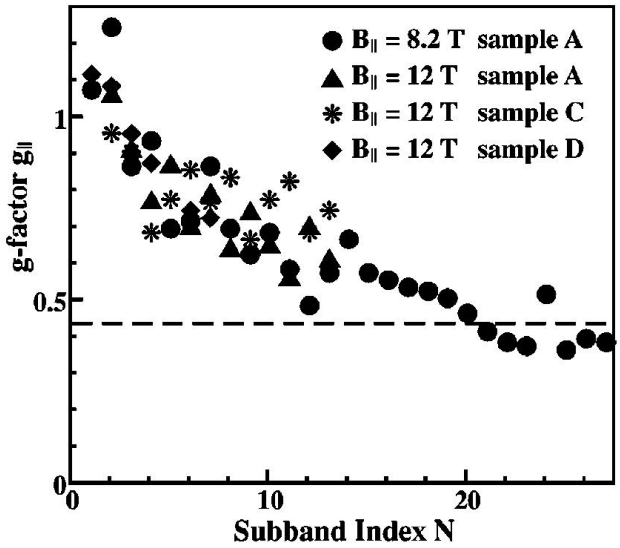

Figure 2.7: The in-plane g factor $g_{\|}$ as a function of subband index N, from [18]. The dashed line at $|g| = 0.44$ indicates the g factor for bulk GaAs.

the only difference being the higher energy scale due to the larger subband spacing provided by the shallow-etching technique. The temperature dependence of the conductance suppression was interpreted as thermal activation across a gap between the average chemical potential and an anomalous subband edge.

Singlet-triplet resonances

Rejec *et al.* [27] showed that an electron can be bound in a cylindrical quantum wire with a small thickness fluctuation. The bound electron affects the transport via Coulomb interaction and can form singlet or triplet resonances, resulting in conductance structures at $0.25(2e^2/h)$ and $0.75(2e^2/h)$. However, the 0.7 structure in 1D constrictions has not the features of a resonance structure, and no structure at $\sim 0.25(2e^2/h)$ has been observed in the linear conductance. Also, the saddle-point potential of a 1D constriction is different from the cylindrical bulging wire.

Kondo-like effect

In 2002 Cronenwett *et al.* [28] measured the electrical conductance of split-gate devices as a function of temperature, magnetic field and source-drain bias. Source-drain bias measurements at low temperatures and in low magnetic field show a *zero-bias anomaly*: a narrow peak in the $G(V_{sd}, V_g = \text{const.})$ curves about $V_{sd} = 0$, corresponding to a "lifting" of the conductance of the 0.7 structure towards

$2e^2/h$. The peak disappears at high temperatures, and splits into two peaks when the magnetic field is increased. These properties of the 0.7 structure lead Cronenwett *et al.* to interpret the 0.7 structure as something similar to the Kondo effect in quantum dots.

The interpretation of the 0.7 structure as Kondo-like effect is also supported by the fact that the conductance scales with temperature following a Kondo-like form, and that the corresponding Kondo temperature can be related to the width of the zero-bias peak. However, there is no obvious way to localize a spin in an open system like a 1D constriction. Meir *et al.* [29] showed that multiple reflections between entrance and exit of a constriction result in a single bound electron, which can be treated as an $s = 1/2$ Kondo impurity.

More experimental results

Further experimental results were obtained by Appleyard *et al.* [30], who measured the thermopower of a split-gate device in magnetic field. When the magnetic field is zero, the measured thermopower corresponding to the 0.7 structure is not proportional to the transconductance, violating the Cutler-Mott relation (3.17b). In high magnetic fields the subbands are Zeeman-split and the thermopower follows the Cutler-Mott relation.

Graham et al. [31] performed source-drain bias measurements of split-gate devices in magnetic field. It was found that when Zeeman-split subbands of opposite spin cross, the conductance shows features similar to the 0.7 structure. These "0.7 analogs" are interpreted as consequence of the exchange interaction, which lifts the degeneracy at the crossing point.

Roche *et al.* [32] measured the non-equilibrium current noise in a split-gate device. The Fano factor was found to be significantly reduced on the 0.7 structure. In high magnetic fields, where the 0.7 structure has evolved into the Zeeman-split plateau at e^2/h, the Fano factor was zero, as expected. Based on these results, the 0.7 structure was interpreted as a consequence of two conducting channels with different transmission probabilities, associated with different spin orientations.

The 0.7 structure has been investigated also in quantum wires longer than the typical split-gate device. Reilly *et al.* [33] measured the conductance of quantum wires with nominal lengths of $l = 0, 0.5,$ and 2 µm. The results obtained for the $l = 0$ µm quantum wires are consistent with the measurements performed by others. The measurements of the $l = 0.5$ µm quantum wire show a feature at $0.7(2e^2/h)$, which evolves continuously towards $\sim 0.55(2e^2/h)$ with increasing

electron density. In the $l = 2$ µm quantum wire a feature at $G \approx 0.5(2e^2/h)$ is observed, in addition to a feature at $\sim 1.7(2e^2/h)$.

Luttinger liquid and Wigner crystallization

A typical objection against the theories of the 0.7 structure is that a 1D conductor with interacting electrons is a Luttinger liquid. Maslov and Stone [34] have shown that a Luttinger liquid connected to reservoirs has a DC conductance quantized at e^2/h per spin orientation, exactly as in the non-interacting case. In contrast, the thermal conductance is not expected to be quantized at $(e^2/h)L_0T$, because the energy is transported by plasmons, which have different scattering properties than the electrons. So a violation of the Wiedemann-Franz law is expected. In particular, Fazio *et al.* [35] predict that in some temperature range plasmons can be localized due to random variations of electron density in the 1D conductor. The thermal conductance decreases from its non-interacting value with increasing temperature.

Matveev [36] models a quantum wire at low electron density as a Wigner crystal, where the Coulomb interactions between the electrons lead to short-range order. This system displays a separation of spin and charge degrees of freedom, characteristic of a Luttinger liquid. The conductance of the quantum wire is the result of a charge contribution of $2e^2/h$, and a negative correction due to a spin contribution, which depends on temperature.

Despite the amount of theoretical work, there is still no general agreement on the origin of the 0.7 structure. In Chapter 5 we will see that this work provides new information about the transport properties of the 0.7 structure, in particular that the thermal conductance is reduced and the Wiedemann-Franz law is violated.

Bibliography

[1] C. W. J. Beenakker and H. van Houten, *Solid State Physics* **44**, 1 (1991).

[2] D. K. Ferry and S. M. Goodnick, *Transport in Nanostructures* (Cambridge University Press, Cambridge, 1997).

[3] R. Landauer, *IBM J. Res. Dev.* **1**, 223 (1957).

[4] M. Büttiker, *Phys. Rev. Lett.* **57**, 1761 (57).

[5] S. Datta, *Electronic Transport in Mesoscopic Systems* (Cambridge University Press, Cambridge, 1995).

[6] T. J. Thornton, M. Pepper, H. Ahmed, D. Andrews, and G. J. Davies, *Phys. Rev. Lett.* **56**, 1198 (1986).

[7] B. J. van Wees, H. van Houten, C. W. J. Beenakker, J. G. Williamson, L. P. Kouwenhoven, D. van der Marel, and C. T. Foxon, *Phys. Rev. Lett.* **60**, 848 (1988).

[8] D. A. Wharam, T. J. Thornton, R. Newbury, M. Pepper, H. Ahmed, J. E. F. Frost, D. G. Hasko, D. C. Peacock, D. A. Ritchie, and G. A. C. Jones, *J. Phys. C* **21**, L209 (1988).

[9] R. Landauer, *Phil. Mag.* **21**, 863 (1970).

[10] D. S. Fisher and P. A. Lee, *Phys. Rev. B* **23**, 6851 (1981).

[11] H.-L. Engquist and P. W. Anderson, *Phys. Rev. B* **24**, 1151 (1981).

[12] Y. Imry, *Physics of Mesoscopic Systems* (World Scientific Press, Singapore, 1986).

[13] M. Büttiker, Y. Imry, R. Landauer, and S. Pinhas, *Phys. Rev. B* **31**, 6207 (1985).

[14] A. D. Stone and A. Szafer, *IBM J. Res. Develop.* **32**, 384 (1988).

[15] H. A. Fertig and B. I. Halperin, *Phys. Rev. B* **36**, 7969 (1987).

[16] M. Büttiker, *Phys. Rev. B* **41**, 7906 (1990).

[17] K. J. Thomas, J. T. Nicholls, M. Y. Simmons, M. Pepper, D. R. Mace, and D. A. Ritchie, *Phys. Rev. Lett.* **77**, 135 (1996).

[18] K. J. Thomas, J. T. Nicholls, N. J. Appleyard, M. Y. Simmons, M. Pepper, D. R. Mace, and D. A. Ritchie, *Phys. Rev. B* **58**, 4846 (1998).

[19] K. J. Thomas, J. T. Nicholls, M. Pepper, W. R. Tribe, M. Y. Simmons, and D. A. Ritchie, *Phys. Rev. B* **61**, R13365 (2000).

[20] K. J. Thomas, J. T. Nicholls, M. Pepper, M. Y. Simmons, D. R. Mace, and D. A. Ritchie, *Physica E* **12**, 708 (2002).

[21] N. K. Patel, L. Martin-Moréno, M. Pepper, R. Newbury, J. E. F. Frost, D. A. Ritchie, G. A. C. Jones, J. T. M. B. Janssen, J. Singleton, and J. A. A. J. Perenboom, *J. Phys.: Cond. Matt.* **2**, 7247 (1990).

[22] N. K. Patel, J. T. Nicholls, L. Martin-Moréno, M. Pepper, J. E. F. Frost, D. A. Ritchie, and G. A. C. Jones, *Phys. Rev. B* **44**, 13549 (1991).

[23] E. Lieb and D. Mattis, *Phys. Rev.* **125**, 164 (1962).

[24] C.-K. Wang and K.-F. Berggren, *Phys. Rev. B* **54**, 14257 (1996).

[25] A. Kristensen, J. Bo Jensen, M. Zaffalon, C. B. Sørensen, S. M. Reimann, P. E. Lindelof, M. Michel, and A. Forchel, *J. Appl. Phys.* **83**, 607 (1998).

[26] A. Kristensen, H. Bruus, A. E. Hansen, J. B. Jensen, P. E. Lindelof, C. J. Marckmann, J. Nygård, and C. B. Sørensen, *Phys. Rev. B* **16**, 10950 (2000).

[27] T. Rejec, A. Ramšak, and J. H. Jefferson, *Phys. Rev. B* **62**, 12985 (2000).

[28] S. M. Cronenwett, H. J. Lynch, D. Goldhaber-Gordon, L. P. Kouwenhoven, C. M. Marcus, K. Hirose, N. S. Wingreen, and V. Umansky, *Phys. Rev. Lett.* **88**, 226805 (2002).

[29] Y. Meir, K. Hirose, and N. S. Wingreen, *Phys. Rev. Lett.* **89**, 196802 (2002).

[30] N. J. Appleyard, J. T. Nicholls, M. Pepper, W. R. Tribe, M. Y. Simmons, and D. A. Ritchie, *Phys. Rev. B* **62**, 16275 (2000).

[31] A. C. Graham, K. J. Thomas, M. Pepper, N. R. Cooper, M. Y. Simmons, and D. A. Ritchie, *Phys. Rev. Lett.* **91**, 136404 (2003).

[32] P. Roche, J. Ségala, D. C. Glattli, J. T. Nicholls, M. Pepper, A. C. Graham, K. J. Thomas, M. Y. Simmons, and D. A. Ritchie, *Phys. Rev. Lett.* **93**, 116602 (2004).

[33] D. J. Reilly, G. R. Facer, A. S. Dzurak, B. E. Kane, R. G. Clark, P. J. Stiles, R. G. Clark, A. R. Hamilton, J. L. O'Brien, N. E. Lumpkin, L. N. Pfeiffer, and K. W. West, *Phys. Rev. B* **63**, 121311(R) (2001).

[34] D. L. Maslov and M. Stone, *Phys. Rev. B* **52**, R5539 (1995).

[35] R. Fazio, F. W. J. Hekking, and D. E. Khmel'nitskii, *Phys. Rev. Lett.* **80**, 5611 (1998).

[36] K. A. Matveev, *Phys. Rev. B* **70**, 245319 (2004).

Chapter 3

Thermoelectric properties of one-dimensional constrictions

So far the discussion has been focused on the electrical conductance of low-dimensional systems. The main reason is that the conductance has been the principal concern of experimental and theoretical investigations. In this chapter we will extend the discussion to thermoelectric transport. As before, we will first discuss the thermoelectric properties of a LDEG within the semiclassical approach, focusing on the linear response regime. Following Landauer's approach, we will then see the thermoelectric properties for ballistic transport. Finally, we will briefly discuss hot electrons and electron thermometry, necessary to investigate experimentally the thermoelectric transport.

3.1 Thermoelectric transport in an electron gas

The transport in a LDEG in the diffusive regime can be described within the semiclassical approach. The transport properties are expressed in terms of macroscopic phenomenological parameters such as conductance, thermoelectric power and thermal conductance. Before presenting the semiclassical theory of thermoelectric transport, a physical picture of thermoelectric effects will be given.

3.1.1 Physical picture of thermoelectric transport

Consider two reservoirs of electrons (*left* and *right*), connected by a conductor. The electrons in each reservoir are distributed according to the Fermi function, with well defined temperature T_i and chemical potential μ_i ($i = L, R$). The idea is to present the thermoelectric effects as they are measured experimentally, disregarding the details of the conductor connecting the two reservoir. The following discussion follows Landauer's approach to transport, and we will see that it can be applied in a straightforward manner to ballistic transport.

Electrical conductance

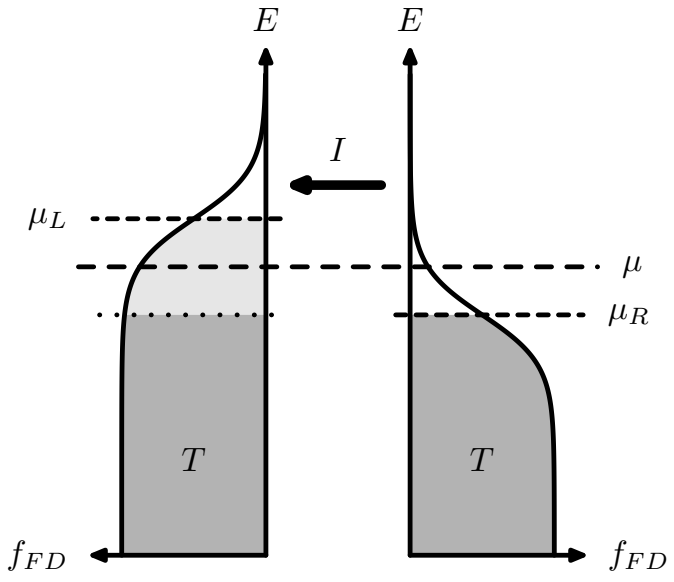

Figure 3.1: *Electrical conductance.* A potential difference ΔV is applied between the reservoirs, which are at the same temperature, $T_L = T_R = T$; μ is the chemical potential in equilibrium. The result is an imbalance in the chemical potentials $\Delta\mu \equiv \mu_L - \mu_R = -e\Delta V$, which gives rise to an electric current I.

Figure 3.1 depicts a typical electrical conductance measurement. A potential

difference ΔV is applied between the two reservoirs, which are at the same temperature, $T_L = T_R = T$ (that is, $\Delta T \equiv T_L - T_R = 0$). The chemical potential in the reservoirs is shifted from the equilibrium value μ such that $\Delta\mu \equiv \mu_L - \mu_R = -e\Delta V$, and as a result there is a net flow of electrons from one reservoir to the other, giving rise to an electric current I. The *electrical conductance* is defined as

$$G = \left(\frac{I}{\Delta V}\right)_{\Delta T=0}. \tag{3.1}$$

If $e\Delta V \ll \mu$, the system is close to equilibrium, and the conductance G yields information about transmission properties at the Fermi energy μ.

In four-terminal measurements the current is controlled as an independent variable, and the potential drop across the conductor is measured. Therefore the quantity measured is the *electrical resistance*

$$R = \left(\frac{\Delta V}{I}\right)_{\Delta T=0} = \frac{1}{G}. \tag{3.2}$$

Thermal conductance

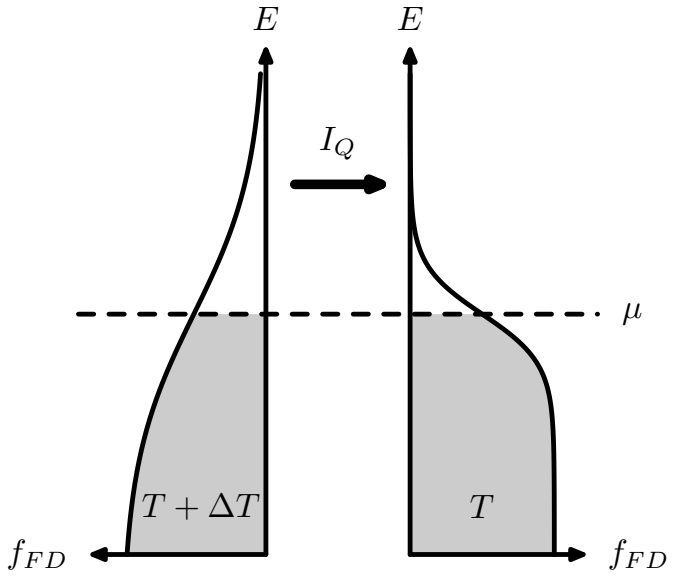

Figure 3.2: *Thermal conductance.* A temperature difference ($\Delta T \neq 0$) is applied between the reservoirs, while the electric current between the two is kept at zero, $I = 0$. The flow of heat I_Q results from the fact that there are more electrons slightly above the chemical potential μ on the left rather than on the right.

Consider the situation in Fig. 3.2. A temperature difference $\Delta T \equiv T_L - T_R > 0$ is applied between the two reservoirs, while the electric current is kept zero ($I = 0$).

This means that the number of electrons going from left to right is the same as the number of electrons going from right to left. Since the electrons coming from the left reservoir have a higher energy than the electrons from the right reservoir (because $T_L > T_R$), there is a net transfer of energy from left to right, i.e., a heat flow I_Q. The *thermal conductance* is defined as

$$\kappa = -\left(\frac{I_Q}{\Delta T}\right)_{I=0}. \tag{3.3}$$

Similar to the electrical conductance, when the system is close to equilibrium ($\Delta T \ll T_L, T_R$), the thermal conductance gives information about the transmission at μ, $t(\mu$.

Electrons carry both electric charge and energy, so the thermal conductance is connected to the electrical conductance via the *Wiedemann-Franz law*:

$$\kappa = L_0 T G, \tag{3.4}$$

where $L_0 = \dfrac{\pi^2 k_B^2}{3e^2} \approx 2.44 \times 10^{-8}$ WΩ/K^2 is the *Lorenz number*.

Cross-effects

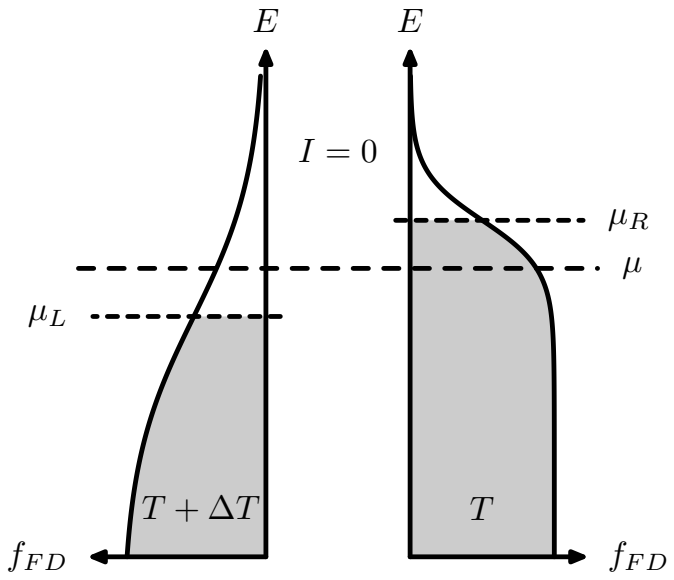

Figure 3.3: *Seebeck effect.* A temperature difference $\Delta T \neq 0$ is applied to the reservoirs, while the electric current is kept zero, $I = 0$. The result is an imbalance in the chemical potentials between the two reservoirs, which yields a potential difference $\Delta V = \frac{1}{-e}\Delta\mu$.

Figure 3.3 shows the *Seebeck effect*, which occurs when a temperature difference ΔT is applied between the two reservoirs and the electric current is kept zero ($I = 0$). The flow of electrons from the hot reservoir to the cold reservoir is balanced by a potential difference ΔV (*thermovoltage*), which is proportional to the temperature difference ΔT. The *thermoelectric power* (or *thermopower*) is defined as

$$S = -\left(\frac{\Delta V}{\Delta T}\right)_{I=0}. \tag{3.5}$$

The *Peltier effect* is a heat flow I_Q due to an electric current I, when there is no temperature difference between the two reservoirs. The corresponding *Peltier coefficient* is defined as

$$\Pi = \left(\frac{I_Q}{I}\right)_{\Delta T=0}. \tag{3.6}$$

Both the Seebeck and the Peltier effects relate thermal properties to electrical properties, and the two are themselves related through the *Kelvin-Onsager relation*: $\Pi = ST$ (see Eq. (3.11c)).

3.1.2 Formalism of thermoelectric transport

Usually thermoelectric transport in the diffusive regime is approached via the theory of non-equilibrium thermodynamics [1]. A system of particles is defined in terms of *extensive parameters*, such as total entropy, total energy, number of particles, *etc.* The system is also characterized by *intensive parameters*, such as temperature and chemical potential. In equilibrium the intensive parameters are constant throughout the system. When there are spatial gradients of these parameters, there are fluxes of the extensive parameters and the system is out of equilibrium. For example, a gradient in temperature results in a heat flow, while a gradient in density yields diffusion (flow of particles).

Empirically, for a large class of irreversible phenomena and under a wide range of experimental conditions, a system can be assumed to be in local equilibrium. This means that thermodynamic quantities such as entropy, temperature, density, *etc.*, are well defined locally. Also, under the same conditions, the irreversible flows of the extensive parameters are well approximated by linear functions of the gradients of the intensive parameters. These linear functions are the formal expression of phenomenological laws such as Fourier's law of heat conduction and Ohm's law for electrical conduction.

For a diffusive conductor the relevant intensive parameters for thermoelectric

transport are the temperature T and the electrochemical potential $\mu_e = \mu - eV$, where V is the electric potential. Gradients of these parameters drive electric currents and heat flows. If the electric field and the temperature gradient are small and slowly varying, the electric current density $\mathbf{j}$ and the thermal current density $\mathbf{j_Q}$ can be expressed in terms of linear functions of the gradients [2, 3]:

$$\begin{pmatrix} \mathbf{j} \\ \\ \mathbf{j_Q} \end{pmatrix} = \begin{pmatrix} \mathcal{L}^{(0)} & \frac{1}{eT}\mathcal{L}^{(1)} \\ \\ -\frac{1}{e}\mathcal{L}^{(1)} & -\frac{1}{e^2T}\mathcal{L}^{(2)} \end{pmatrix} \begin{pmatrix} \frac{1}{e}\nabla\mu_e \\ \\ \nabla T \end{pmatrix} = \begin{pmatrix} \boldsymbol{\sigma} & \mathsf{L} \\ \\ \mathsf{M} & \mathsf{N} \end{pmatrix} \begin{pmatrix} \frac{1}{e}\nabla\mu_e \\ \\ \nabla T \end{pmatrix}, \tag{3.7}$$

where the thermoelectric transport coefficients $\boldsymbol{\sigma}$, L, M and N are tensors (following the notation in Ref. [4]), and are defined in terms of integrals:

$$\mathcal{L}^{(\alpha)} = -e^2 \int_0^\infty dE\ D(E)\ \tau(E)\ \mathbf{v}(E)\mathbf{v}(E)\ (E-\mu)^\alpha \frac{\partial f_0}{\partial E}(E) \tag{3.8}$$

(see Section 1.3.1 for the definition of the terms used). The transport coefficients satisfy the Onsager reciprocity relations [5, 6]:

$$\boldsymbol{\sigma}(\mathbf{B}) = \tilde{\boldsymbol{\sigma}}(-\mathbf{B}) \tag{3.9a}$$

$$\mathsf{L}(\mathbf{B}) = -\frac{1}{T}\tilde{\mathsf{M}}(-\mathbf{B}) \tag{3.9b}$$

$$\mathsf{N}(\mathbf{B}) = \tilde{\mathsf{N}}(-\mathbf{B}), \tag{3.9c}$$

where $\mathbf{B}$ is the magnetic field and $\tilde{\mathsf{A}}$ is the transpose of the matrix A.

In experiments it is usual to control the electric current and the temperature as independent variables. So, it is often more convenient to rearrange Eq. (3.7) in the following way:

$$\begin{pmatrix} \frac{1}{e}\nabla\mu_e \\ \\ \mathbf{j_Q} \end{pmatrix} = \begin{pmatrix} \boldsymbol{\rho} & \mathsf{S} \\ \\ \boldsymbol{\pi} & -\boldsymbol{\kappa} \end{pmatrix} \begin{pmatrix} \mathbf{j} \\ \\ \nabla T \end{pmatrix}, \tag{3.10}$$

where $\boldsymbol{\rho}$, S, $\boldsymbol{\pi}$ and $\boldsymbol{\kappa}$ are respectively the resistivity, the thermoelectric power, the Peltier coefficient and the thermal conductivity. These quantities are related to

the transport coefficients via the following relations:

$$\boldsymbol{\rho} = \boldsymbol{\sigma}^{-1} \tag{3.11a}$$

$$\mathsf{S} = -\boldsymbol{\rho}\mathsf{L} \tag{3.11b}$$

$$\boldsymbol{\pi} = \mathsf{M}\boldsymbol{\rho} = \mathsf{S}T \tag{3.11c}$$

$$\boldsymbol{\kappa} = \mathsf{M}\boldsymbol{\rho}\mathsf{L} - \mathsf{N}. \tag{3.11d}$$

For an isotropic conductor and in the absence of magnetic field, the tensors are diagonal. In the degenerate limit, the transport coefficients (3.11) can be written as [2]

$$\boldsymbol{\rho} \approx \frac{1}{\sigma(E_F)} \tag{3.12a}$$

$$\mathsf{S} \approx \frac{\pi^2 k_B^2 T}{3e} \left(\frac{d \ln \sigma(E)}{dE} \right)_{E=E_F} \tag{3.12b}$$

$$\boldsymbol{\kappa} \approx L_0 T \sigma(E_F). \tag{3.12c}$$

Equation (3.12a) is a result we have seen with Eq. (1.27), where we implicitly defined $\sigma = \dfrac{e^2 n \langle\tau\rangle}{m^*}$ with $\langle\tau\rangle \approx \tau(E_F)$. Equation (3.12b) is the *Cutler-Mott formula* for thermopower [7]. Equation (3.12c) is the Wiedemann-Franz law (see Eq. (3.4) and Ref. [2]). In the 2DEG of a GaAs/AlGaAs heterostructure, the Wiedemann-Franz law (3.12c) is valid as long as $\sigma(E)$ is a slowly varying function over the range $k_B T$ and the scattering is predominantly elastic. As seen in Sec. 1.3.2, these conditions are satisfied at low temperatures where scattering is dominated by ionized impurities. At higher temperatures electron-phonon scattering is not negligible and needs to be taken into account (e. g., *phonon drag* [8,9]); it also results in a violation of the Wiedemann-Franz law [10].

3.2 Thermoelectric properties of one-dimensional constrictions

We have seen that ballistic transport occurs in structures which have a size L, W less than the mean free path L_e of the electrons. There is no scattering inside the conductor, hence the assumption of local equilibrium breaks down. In the absence of local equilibrium, we cannot define a local temperature, chemical potential, and their gradients. However, the temperatures and the chemical potentials of the reservoirs connected to the conductor are still well defined. This is where the discussion presented in Section 3.1.1 is helpful. We can discuss the thermoelectric transport in terms of quantities defined in the reservoirs that are connected by the ballistic conductor. The electric conductance, thermal conductance, *etc.*, are determined by the transmission properties of the conductor.

Sivan and Imry [11] extended the Landauer formula for the conductance (Section 2.2.1) to take into account temperature differences. A multi-terminal formulation was given by Butcher [4]. The discussion in the rest of this section follows van Houten *et al.* [12].

3.2.1 Landauer-Büttiker formalism for thermoelectric transport

Consider two reservoirs connected by a conductor, as in Section 3.1.1. If we substitute gradients with differences between the reservoirs, we can write the non-local version of Eq. (3.7):

$$\begin{pmatrix} I \\ \\ I_Q \end{pmatrix} = \begin{pmatrix} L^{(0)} & \frac{1}{eT}L^{(1)} \\ \\ -\frac{1}{e}L^{(1)} & -\frac{1}{e^2T}L^{(2)} \end{pmatrix} \begin{pmatrix} \frac{1}{e}\Delta\mu_e \\ \\ \Delta T \end{pmatrix} = \begin{pmatrix} G & L \\ \\ M & K \end{pmatrix} \begin{pmatrix} \frac{1}{e}\Delta\mu_e \\ \\ \Delta T \end{pmatrix}, \tag{3.13}$$

where $T = \dfrac{T_L + T_R}{2}$ is the average temperature and $L^{(\alpha)}$, given by

$$L^{(\alpha)} = \frac{2e^2}{h}\int_0^\infty t(E)\,(E - E_F)^\alpha \left(-\frac{\partial f_0}{\partial E}\right) dE, \tag{3.14}$$

is the equivalent of Eq. (3.8); $t(E)$ is the transmission of the conductor (a factor 2 is included for spin-degeneracy). Equation (3.13) can be rewritten as

$$\begin{pmatrix} \frac{1}{e}\Delta\mu_e \\ \\ I_Q \end{pmatrix} = \begin{pmatrix} R & S \\ \\ \Pi & -\kappa \end{pmatrix} \begin{pmatrix} I \\ \\ \Delta T \end{pmatrix}, \tag{3.15}$$

where the coefficients are the same as defined in Section 3.1.1 and satisfy the following relations:

$$R = G^{-1} \tag{3.16a}$$

$$S = -\frac{L}{G} \tag{3.16b}$$

$$\Pi = \frac{M}{G} = ST \tag{3.16c}$$

$$\kappa = -K\left(1 + \frac{S^2GT}{K}\right). \tag{3.16d}$$

The tensorial character of the transport coefficient has been ignored, but in the presence of a magnetic field, they satisfy the same Onsager relations as in Eq. (3.9).

In the degenerate limit, the thermoelectric coefficients for the linear-response regime become:

$$G \approx \frac{2e^2}{h} t(E_F) \tag{3.17a}$$

$$S \approx \frac{\pi^2 k_B^2 T}{3e} \left(\frac{d\ln t(E)}{dE}\right)_{E=E_F} \tag{3.17b}$$

$$\kappa \approx L_0 TG. \tag{3.17c}$$

The similarities of these equations with the semiclassical case (3.12) are obvious, the new feature being the transmission coefficient $t(E)$ of the conductor.

3.2.2 Thermoelectric coefficients for the saddle-point potential

In Section 2.3 the saddle-point potential was introduced as a model for the electrostatic potential produced in a split-gate device. The transmission is given by

$$t(E) = \sum_{n=0}^{\infty} \left[1 + \exp\left(-\frac{2\pi\,(E - E_n)}{\hbar\omega_x} \right) \right]^{-1}, \tag{3.18}$$

where $E_n = \hbar\omega_y \left(n + \frac{1}{2}\right) + V_0$. Equation (3.18) enables us to calculate the thermoelectric coefficients via the integral in Eq. (3.14).

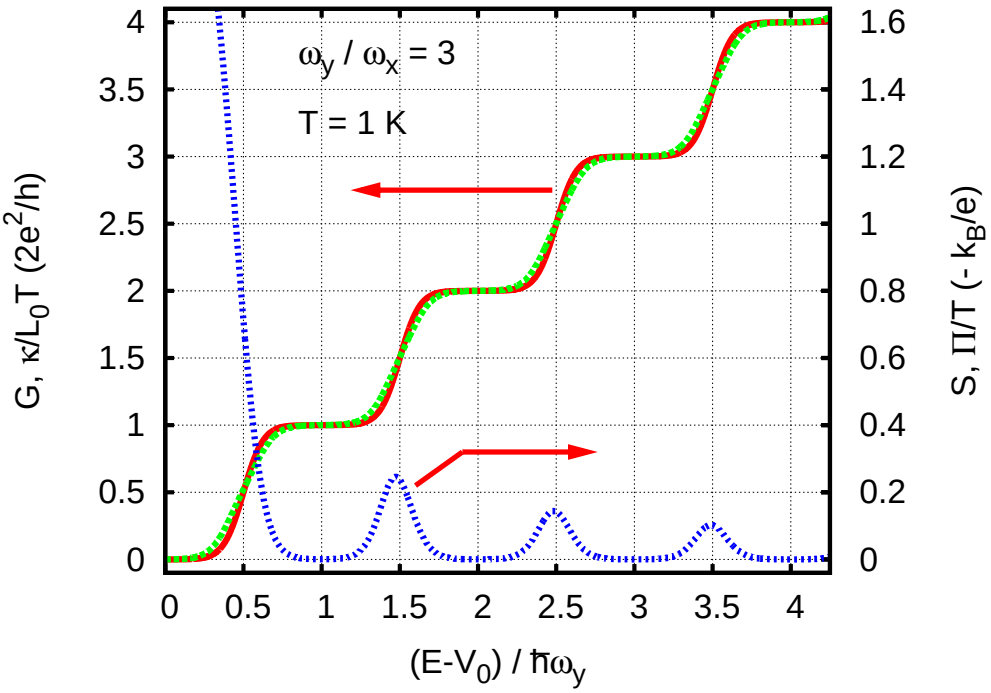

Figure 3.4: Calculated thermoelectric coefficients for a saddle-point potential as a function of Fermi level, after [12]. Left axis: conductance G (full curve) and thermal conductance κ/L_0T (broken curve); right axis: thermopower S and Peltier coefficient Π/T (same dotted curve). The parameters for the saddle-point potential are $\hbar\omega_x = 1$ meV, $\hbar\omega_y = 3$ meV; the temperature T is 1 K.

Figure 3.4 shows an example of the calculated thermoelectric coefficients. The electrical conductance follows closely the total transmission at the Fermi level (Eq. (3.17a) and Fig. 2.5), which is in agreement with experimental results. The

calculated thermal conductance follows the Wiedemann-Franz law (3.17c) except where the condition $S^2 \ll L_0$ is not satisfied. The thermopower satisfies the Cutler-Mott relation (3.12b). In particular, it is zero on a conductance plateau and shows peaks between plateaux. Proetto [13] has shown that the thermopower peak between plateau i and plateau $i+1$ is given by:

$$S_{\mathrm{pk}}^{(i)} = \frac{\pi^2 {k_B}^2}{3e} \frac{T}{\hbar\omega_x} \frac{1}{i+\frac{1}{2}}. \tag{3.19}$$

Equation (3.19) can be used to calibrate the thermopower of a constriction to be used as an electron thermometer, as has been shown by Appleyard *et al.* [14].

3.3 Hot electrons and electron thermometry

In order to investigate thermoelectric transport in one-dimensional constrictions, we need to be able to produce temperature differences and measure the temperature in the 2DEG. The *current heating technique* [15] is a common way to increase the temperature of the electrons above the temperature of the lattice in a controlled way. There are several methods available for electron thermometry, but we will focus on the technique described by Appleyard *et al.* [14], which uses the thermopower of a 1D constriction as a thermometer.

"Hot" electrons at low temperatures

The main scattering mechanisms for electrons in a GaAs/AlGaAs heterostructure have been discussed in Sec. 1.3.2. For a LDEG in the Bloch-Grüneisen regime, the electron-phonon interaction is weak and is responsible for the energy-loss of the electrons.[1] If we apply a voltage to a LDEG beyond the linear response regime, the electron gas gains energy from the electric field. Anderson *et al.* [16] showed that if the scattering rate τ_{ee}^{-1} for electron-electron interaction is much higher than the rate τ_{eph}^{-1} for electron-phonon interaction, the electron gas can be described by a new Fermi function.[2] The hot electrons can be considered as a system in equilibrium at a temperature T_{el}, weakly coupled to the system of phonons in equilibrium at a temperature $T_{ph} \leq T_{el}$ (*two-bath model*).

A steady state is reached when the power of the Joule heating of electron gas is balanced by the energy-loss rate due to scattering with phonons. In this case the net energy-loss rate of the electrons to the phonons is [15]

$$\dot{Q}_{el-ph}(T_{el}, T_{ph}) = N_{el} \left(F(T_{el}) - F(T_{ph}) \right), \tag{3.20}$$

where $\dot{Q}_{el-ph}$ is the power lost, N_{el} is the number of electrons, and $F(T)$ is a function which depends on the energy-loss mechanism. For a 2DEG in a GaAs/AlGaAs heterostructure at low temperatures, $F(T) = \alpha T^{\gamma}$, where α and γ depend on the specific scattering mechanism. Measuring the temperature dependence of $\dot{Q}_{el-ph}$ can give us information about the specific electron-phonon interaction responsible

[1] Coulomb scattering is elastic and does not contribute to the energy relaxation.

[2] For example, in an AlGaAs/GaAs heterostructure at low temperatures, τ_{eph} is of the order of 1 ns [17], and τ_{ee} can be as low as 10 fs [18], depending on the electron density.

for the energy relaxation of the electrons [18–20]:

$\gamma = 3$ unscreened PZ
$\gamma = 5$ unscreened DP and screened PZ
$\gamma = 7$ screened DP

For the temperature range of our interest ($T < 1$ K), we are in the Bloch-Grüneisen regime. Experiments have shown that in this regime $\gamma \approx 5$ [14, 20].

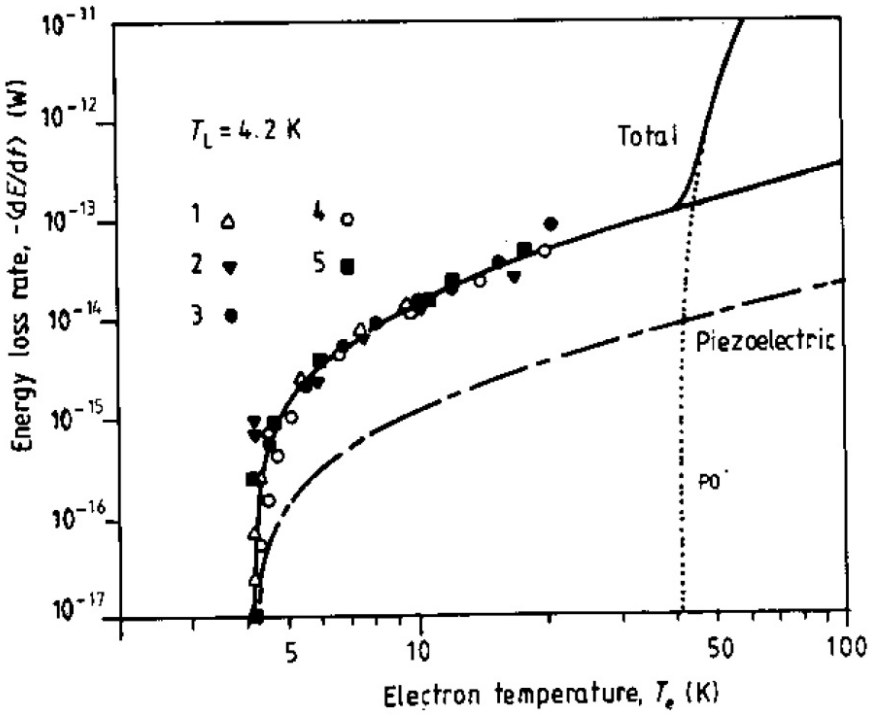

Figure 3.5: Acoustic-phonon energy loss rates in GaAs/AlGaAs heterostructures, from Shubnikov-de Haas data, from [21]. The experimental points are fitted to theory using a deformation potential of 11 eV. The contributions made by piezoelectric and polar optical modes are also shown.

Electron thermometry

Due to the weak coupling between electrons and phonons, the techniques available to measure the lattice temperature of bulk materials cannot be applied to electrons. Several techniques take advantage of the electrical transport properties of the 2DEG itself, such as the temperature dependence of the zero field resistance and weak localization corrections [22, 23], or the Shubnikov-de Haas oscillations in the magnetoresistance [20, 24, 25]. Mesoscopic effects such as Coulomb blockade have also been used for electron thermometry [26].

Molenkamp *et al.* [27] introduced the idea of using the thermopower of a 1D constriction to probe the local temperature of a 2DEG. Appleyard *et al.* [14] have shown how the thermopower can be calibrated to measure the electron temperature. Using the saddle-point potential model, it is possible to relate the height of the peaks in the thermopower to the parameters ω_x and ω_y of the potential, as can be seen from Eq. (3.19). These parameters can be determined from conductance measurements far from equilibrium, and hence allow the calibration of the thermopower, which can be used as a secondary thermometer.

Bibliography

[1] S. R. de Groot and P. Mazur, *Non-Equilibrium Thermodynamics* (Dover Publications, New York, 1984).

[2] N. W. Ashcroft and N. D. Mermin, *Solid State Physics* (Saunders College Publishing, 1976).

[3] J. M. Ziman, *Electrons And Phonons. The Theory of Transport Phenomena in Solids* (Oxford University Press, Oxford, 1963).

[4] P. N. Butcher, *J. Phys.: Cond. Matt.* **2**, 4869 (1990).

[5] L. Onsager, *Phys. Rev.* **37**, 405 (1931).

[6] L. Onsager, *Phys. Rev.* **38**, 2265 (1931).

[7] N. F. Mott and H. Jones, *The Theory of the Properties of Metals and Alloys* (Clarendon, Oxford, 1936).

[8] D. G. Cantrell and P. N. Butcher, *J. Phys. C* **19**, L429 (1986).

[9] R. T. Syme and M. Pepper, *J. Phys.: Cond. Matt.* **1**, 2747 (1989).

[10] A. A. Abrikosov, *Fundamentals of the Theory of Metals* (Elsevier Science Publisher, 1988).

[11] U. Sivan and Y. Imry, *Phys. Rev. B* **33**, 551 (1986).

[12] H. van Houten, L. W. Molenkamp, C. W. J. Beenakker, and C. T. Foxon, *Semicond. Sci. Technol.* **7**, B215 (1992).

[13] C. R. Proetto, *Phys. Rev. B* **44**, 9096 (1991).

[14] N. J. Appleyard, J. T. Nicholls, M. Y. Simmons, W. R. Tribe, and M. Pepper, *Phys. Rev. Lett.* **81**, 3491 (1998).

[15] M. C. Payne, R. A. Davies, J. C. Inkson, and M. Pepper, *J. Phys. C* **16**, L291 (1983).

[16] P. W. Anderson, E. Abrahams, and T. V. Ramakrishnan, *Phys. Rev. Lett.* **43**, 718 (1979).

[17] A. A. Verevkin, N. G. Ptitsina, G. M. Chulcova, G. N. GolŠtsman, E. M. Gershenzon, and K. S. Yngvesson, *Phys. Rev. B* **53**, R7592 (1996).

[18] B. K. Ridley, *Rep. Prog. Phys.* **54**, 169 (1991).

[19] T. Kawamura and S. D. Sarma, *Phys. Rev. B* **45**, 3612 (1992).

[20] Y. Ma, R. Fletcher, E. Zaremba, M. D'Iorio, C. T. Foxon, and J. J. Harris, *Phys. Rev. B* **43**, 9033 (1991).

[21] K. Hirakawa and H. Sakaki, *Appl. Phys. Lett.* **49**, 889 (1986).

[22] A. K. M. Wennberg, S. N. Ytterboe, C. M. Gould, H. M. Bozler, J. Klem, and H. Morkoç, *Phys. Rev. B* **34**, 4409 (1986).

[23] A. Mittal, R. G. Wheeler, M. W. Keller, D. E. Prober, and R. N. Sacks, *Surf. Sci.* **361/362**, 537 (1996).

[24] A. B. Fowler, F. F. Fang, W. E. Howard, and P. J. Stiles, *Phys. Rev. Lett.* **16**, 901 (1966).

[25] S. J. Manion, M. Artaki, M. A. Emanuel, J. J. Coleman, and K. Hess, *Phys. Rev. B* **35**, 9203 (1987).

[26] J. P. Pekola, K. P. Hirvi, J. P. Kauppinen, and M. A. Paalanen, *Phys. Rev. Lett.* **73**, 2903 (1994).

[27] L. W. Molenkamp, H. van Houten, C. W. J. Beenakker, R. Eppenga, and C. T. Foxon, *Phys. Rev. Lett.* **65**, 1052 (1990).

Chapter 4

Experimental techniques

All the experimental work described in this dissertation required the measurement of small voltages and currents in mesoscopic structures fabricated from GaAs/AlGaAs heterostructures or quantum wells. From these experiments we determine the electron temperature, electrical, and thermal conductance of 1D ballistic conductors.

The ideas behind the design and the fabrication of the devices will be presented first. We will show that the quality of the devices are a major improvement on previous work. Then, we will describe the measurements; the focus will be on the electrical circuits, rather than the methods to achieve the low temperatures necessary for the measurements.

4.1 Devices

The devices were fabricated from wafers grown by Dr. M. Y. Simmons and Dr. I. Farrer at the MBE facility at the *Cavendish Laboratory*, Cambridge University. The photolithography was done by Dr. Y. Proskuryakov and Mr. J. Underdown at RHUL, with advice from Dr. N. Lumpkin at the *Cavendish Laboratory*. The e-beam lithography was done by myself at RHUL.

Device	Wafer	Depth	Spacer	Density	Mobility
I	T458	297 nm	80 nm	2.5×10^{11} cm^{-2}	3.3×10^{6} cm^2/Vs
II	T567	97 nm	40 nm	3.2×10^{11} cm^{-2}	1.4×10^{6} cm^2/Vs
III	T569	97 nm	40 nm	$\sim 3.1 \times 10^{11}$ cm^{-2}	$\sim 4.9 \times 10^{6}$ cm^2/Vs

Table 4.1: Characteristics of the wafers. *Wafer* identifies the wafer fabricated at the *Cavendish Laboratory*. The *depth* of the 2DEG is measured from the surface of the wafer; *Spacer* is the width of the spacer layer. The electron density and the mobility are obtained from the characterization measurements, where possible.

4.1.1 Design

Molenkamp *et al.* [1] was the first to measure the thermopower of a split-gate to probe the local temperature of the electron gas, allowing measurements of heat flow through a second split-gate. The measurements showed that the Peltier coefficient has the same oscillations as a function of gate voltage as the thermopower, a result expected from Eq. (3.16c). Also, the thermal conductance κ displayed, see Fig. 4.1, weak plateaux corresponding to those seen in the electrical conductance G, as expected from the Wiedemann-Franz law (see Eq. (3.17c)).

Appleyard *et al.* [2] showed that the thermopower of a split-gate can be calibrated, so that it can be used as a secondary thermometer of the electron temperature. An extension of the design used in that experiment was proposed for thermal conductance measurements in Ref. [3], and is used in this work, as shown in Figs. 4.2 and 4.3.

A current $I_H = V_H/R_H$ heats the electrons in the heating channel up to a temperature T_H. Heat flows through the *main constriction A* into the *thermal box* defined by the three split-gates. The electrons in this box are heated up to a temperature T_{box}, and lose heat by conduction through the other two constrictions (B and C) and to the lattice via the electron-phonon interaction. Since the electron-electron interactions occur much faster than any other interaction relevant to heat flows (see Sec. 2.1.1 and 3.3), T_{box} is uniform throughout the thermal

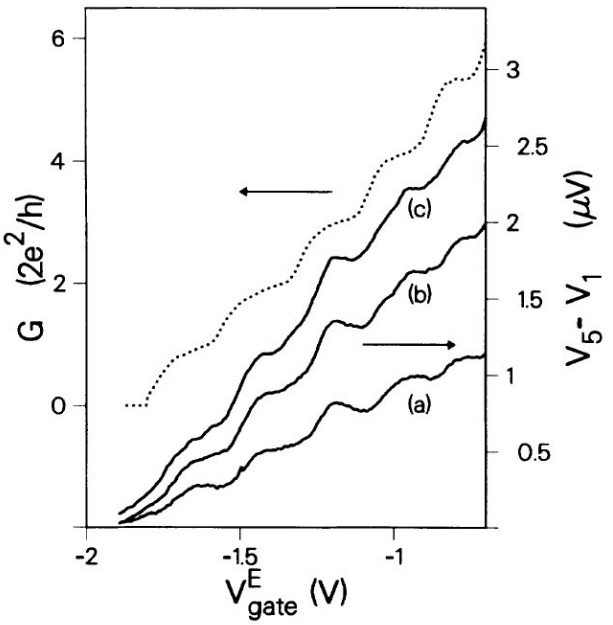

Figure 4.1: Electrical conductance G (dotted line) of a 1D constriction and thermovoltage $V_{th} = V_5 - V_1$ as a function of gate voltage V^E_{gate}, from [1].
The thermovoltage has been measured at a lattice temperature of $T_L = 1.8$ K for different heating currents: (a) 1.0 µA, (b) 1.3 µA, (c) 1.5 µA.

box. The electrons in the voltage arms on the other side of these constrictions, are at the lattice temperature T_L, and are expected to act as a heat sink. The split-gates B and C are used as a thermometer to measure the electron temperature in the box [2, 3]. Since high-impedance voltage probes are used to measure the thermovoltage V^{box}_{th}, no current is expected to flow from the heating channel through any of the constrictions.

T_H is determined by measuring the thermovoltage V^H_{th} when constriction A is not defined. Since the thermal box is small compared to the heating channel, the definition of A does not affect the electron temperature in the channel. When A is not defined, the electrons in the box are heated up to T_H and measuring the thermovoltage yields the correct temperature. The temperature distribution along the heating channel does not affect the measurement of T_H because it is measured locally.

The measurements were carried out in the steady state, where the heat balance

for the thermal box yields:

$$\begin{aligned} I_Q^{(\mathrm{IN})} &= I_Q^{(\mathrm{OUT})} \\ I_Q^{(A)} &= I_Q^{(B)} + I_Q^{(C)} + I_Q^{(el-ph)} \\ \kappa_A(T_H - T_{box}) &= \kappa_B(T_{box} - T_L) + \kappa_C(T_{box} - T_L) + \dot{Q}_{el-ph}(T_{box}, T_L) \\ \kappa_A(T_H - T_{box}) &= (\kappa_B + \kappa_C)(T_{box} - T_L) + \dot{Q}_{el-ph}(T_{box}, T_L), \end{aligned} \tag{4.1}$$

where $\kappa_{A,B,C}$ is the thermal conductance of constriction A, B and C, respectively (as defined by Eq. (3.3)) and $\dot{Q}_{el-ph}(T_{box}, T_L)$ is given by Eq. (3.20).

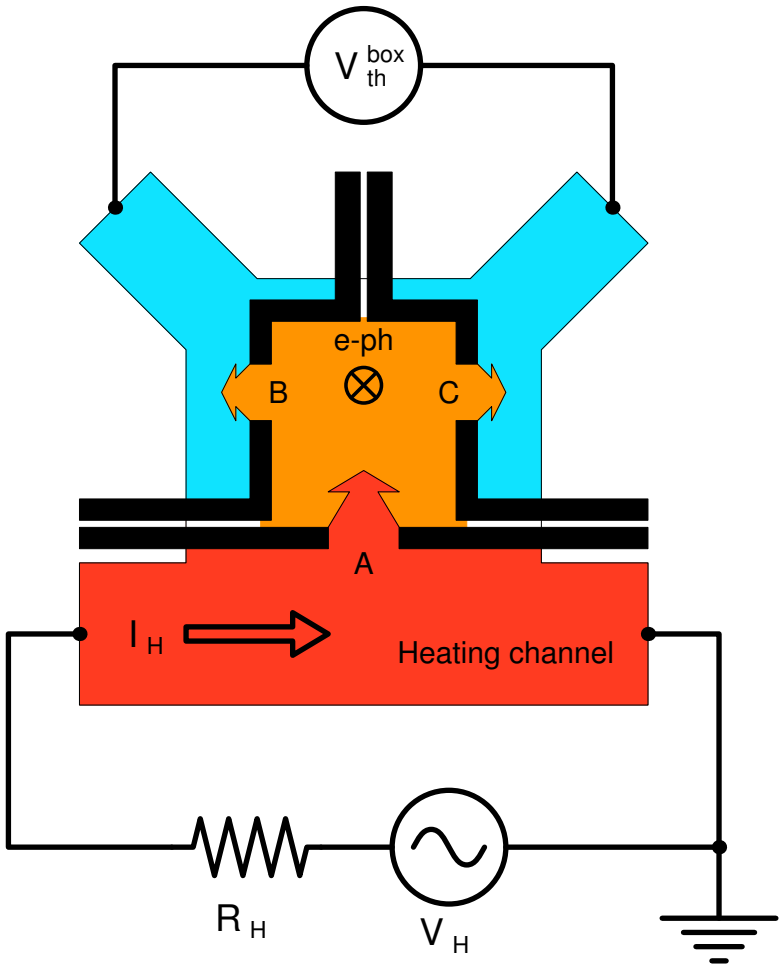

Figure 4.2: Schematic of the measurement of the thermal conductance κ.
The voltage V_H drives the heating current I_H, which is determined by the resistance R_H. I_H heats the electrons in the heating channel to a temperature T_H, and the heat flows through the constrictions A, B, and C as depicted by the arrows. Some amount of heat is lost via the electron-phonon interaction (*e-ph*).
$V_{th}^{box} = (|S_B| + |S_C|) \cdot (T_{box} - T_L)$ is the thermovoltage measured; T_{box} is the electron temperature in the box, and T_L is the lattice temperature.

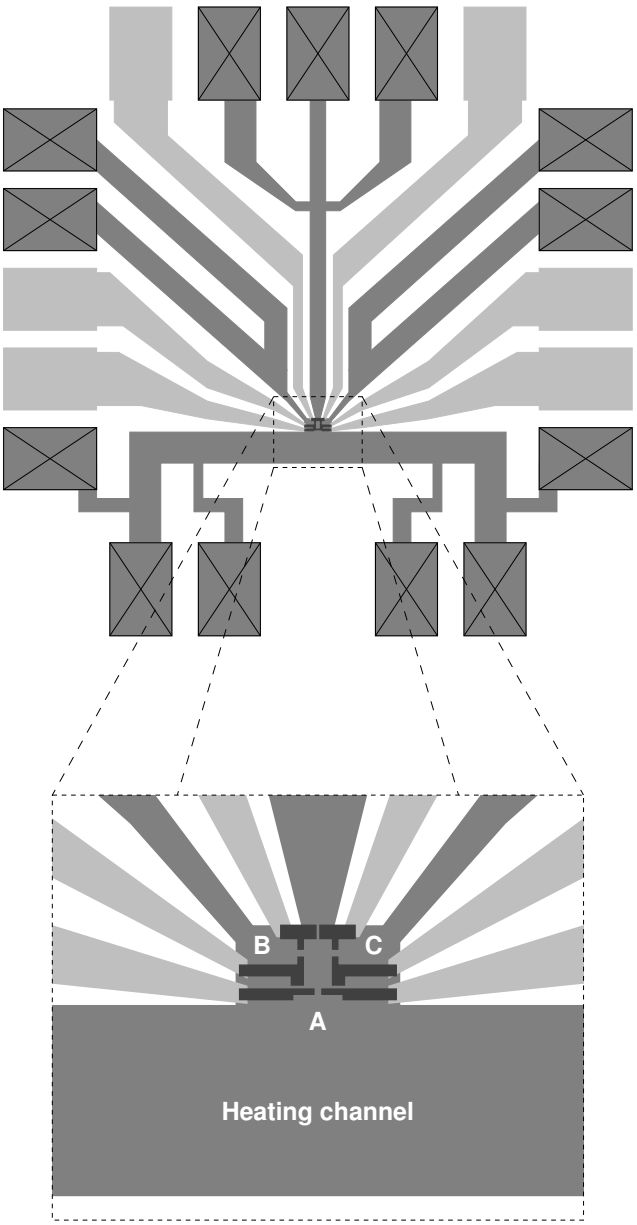

Figure 4.3: Schematic representation of a device. Dark grey areas are the mesa (containing the 2DEG) and light grey areas are the metallic gates fabricated by photolithography. Black structures are the gates fabricated by e-beam lithography and the crossed pads are the ohmic contacts to the 2DEG. A, B, C are the split-gates: A is designated as the "main" split-gate, B is the "thermometer", and C is the "reference". The three split-gates electrostatically define a "box" of electrons with an area between 20 µm^2 and 100 µm^2. The mesa where the thermal box is formed, is approximately (80×40) µm^2 in size, and the heating channel is (800×100) µm^2. The whole chip has an approximate area of (1.4×1.4) mm^2.

4.1.2 Fabrication

The techniques used to fabricate the devices from the wafers are standard, and were carried out in the *clean-room* facilities at RHUL. Photolithography is used to fabricate the mesa, the ohmic contacts to the 2DEG, and the macroscopic gates (*optical gates*). The mesoscopic structures were fabricated by e-beam lithography.

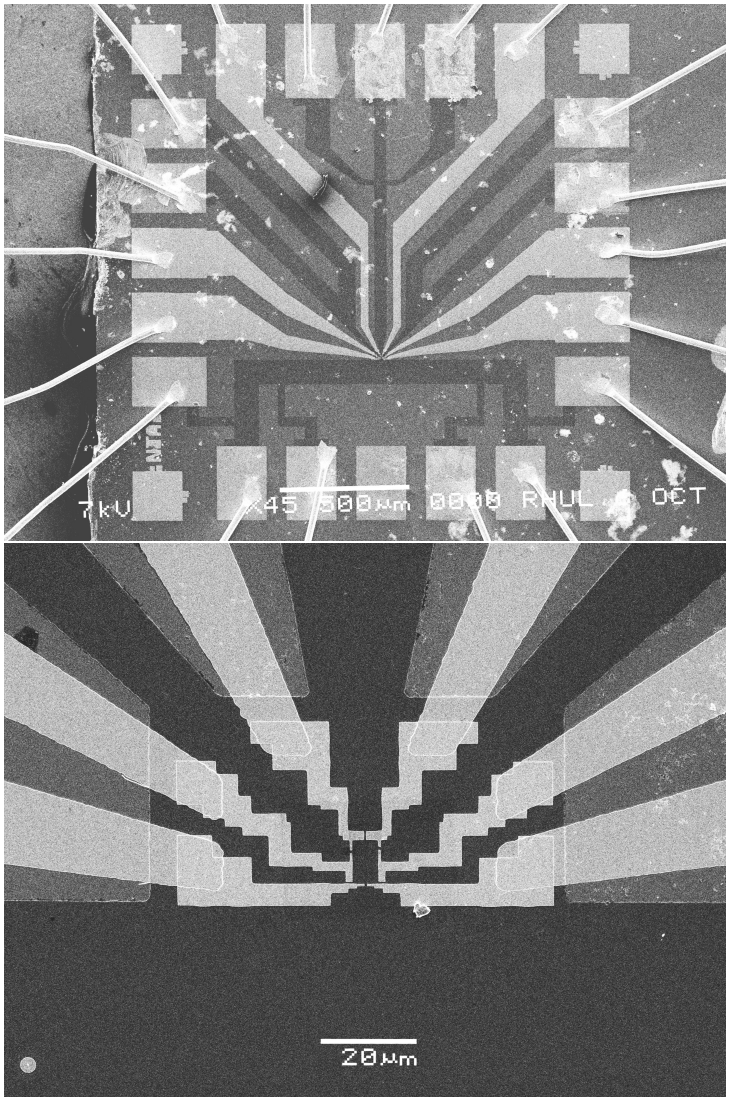

Figure 4.4: SEM micrographs of a typical device. The dark areas are parts of the mesa (containing the 2DEG), the light areas are the macroscopic gates (the "medium grey" areas are the GaAs substrate exposed in the mesa-etching process). Gold wires are bonded to the ohmic pads and the gate pads.

Photolithography: mesa

The resist (*Microposit photoresist S1813*) is spun onto the wafer and baked on a hot-plate for 10 mins at 90℃. The 1.2 µm thick layer of resist is exposed to ultraviolet light through a chrome-on-quartz mask, and the pattern is developed (with *Microposit MF-319*) to expose the regions of the wafer that do not form the mesa. The chip is placed in a wet etchant ($H_3PO_4 : H_2O : H_2O_2$) for $2 - 3$ minutes to remove material to a depth below the level of the 2DEG (the rate is about 40 nm/min), leaving a mesa with the desired pattern. The etching process also passivates the walls of the mesa and electrically isolates the 2DEG.

Photolithography: ohmic contacts and macroscopic gates

Once the mesa has been fabricated, there are two more photolithography steps. In both steps the resist, the exposure and the development are the same as for the mesa, but instead of being etched, the exposed regions are covered with a layer of metal. To make ohmic contacts, approximately 150 nm of AuGeNi alloy is deposited by evaporation in an UHV chamber. After lift-off, the metal is annealed in a Ar atmosphere at 460℃ for 90 seconds. To fabricate the macroscopic gates, 15 nm of *Nichrome 5* and 35 nm of Au are deposited. In both cases, lift-off is achieved by placing the wafer in acetone at 50℃ for several minutes.

E-beam lithography

The chip with completed mesa, ohmic contacts and optical gates is coated with two layers of resist. First, copolymer MMA(8.5)MAA is spun and baked for 10 minutes at 150℃, then PMMA is deposited and baked for 10 minutes at 140℃. This double-layer resist has a thickness of $130 + 60$ nm and provides an *undercut*, which facilitates the lift-off. In the SEM the sample is exposed to a 25 keV electron-beam controlled by a computer, which draws the desired pattern on the surface (shown in Fig. 4.5). After developing the resist in IPA : H_2O (93 : 7) for a few seconds (depending on the exposure dose), evaporation and lift-off occur as for the optical gates.

Finally, the chip is cleaved-cut and glued with *BF-2* into a non-magnetic ceramic package (*Chantek* with 20 leads). The contacts on the wafer are bonded to the package with 25 µm diameter Au wires, using an ultrasonic wedge-bonder.

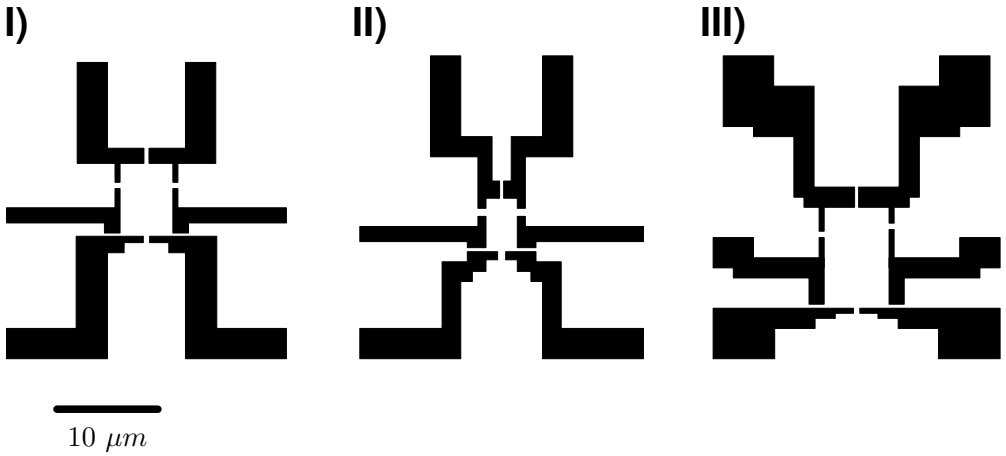

Figure 4.5: The patterns for the e-beam lithography used in the fabrication of the samples presented in this work. From left to right, sample I, II, and III, respectively.

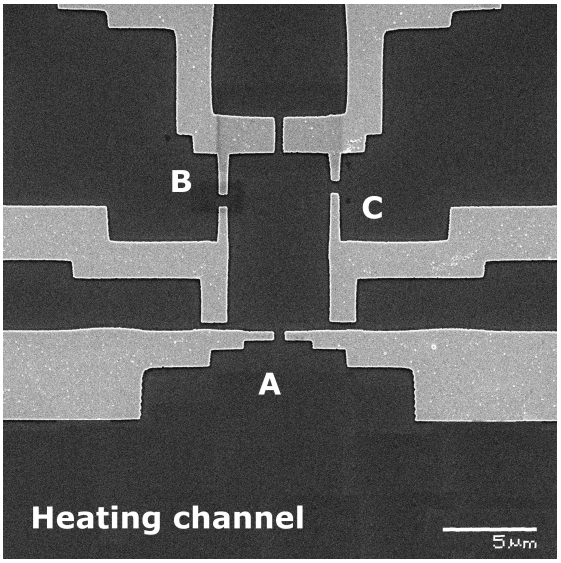

Figure 4.6: SEM micrograph of the thermal box. The split-gates have length $L \approx 0.5$ µm and width $W \approx 0.63$ µm, as defined by the lithography. This design was used in sample III, and the thermal box defined by the gates has an area $A_{box} \approx (6 \times 10)$ µm^2.

4.2 Experimental setups

Initial tests at $T = 4.2$ K were performed in a dipping dewar, to test ohmics, leakage currents and overall characteristics of the split-gates. Lower temperatures are achieved in a pumped ^{3}He cryostat ($0.3 \leq T \leq 1.2$ K), and a ^{3}He/^{4}He dilution refrigerator ($0.03 \leq T \leq 0.75$ K). The setup using the dipping dewar consists of a simple *dipping-probe* with a standard *Chantek* sample holder, which has spring-loaded contacts for electrical connections to the chip carrier. Instruments are connected to the leads via standard BNC connectors at the top of the stick.

The ^{3}He cryostat has a top-loading probe with a *Chantek* sample holder, and electrical access from the outside occurs via BNC connectors. The device sits in a small volume of liquid ^{3}He, which lasts approximately 24 to 48 hours. The temperature of the liquid ^{3}He is controlled by varying the heating power of the sorb that pumps the ^{3}He vapor, giving temperatures in the range $0.3 - 1.2$ K, which are measured by a resistance thermometer mounted in the sample holder. This cryostat has a superconducting coil that provides a magnetic field up to 8 T, perpendicular to the plane of the device.

The ^{3}He/^{4}He dilution refrigerator has a *Chantek* sample holder mounted on the "coldfinger", with electrical access given by BNC connectors. The refrigerator provides continuous cooling with a base temperature of about 10 mK. Temperatures up to about 750 mK are achieved by applying a current to a resistance heater. A RuO_2 thermometer is mounted at the base of the mixing chamber. A superconducting coil with magnetic fields up to 14 T is available.

The experiments involved measuring small currents and voltages, and in order to have a good signal-to-noise ratio, low-frequency AC phase-sensitive detection was employed. Typical setups used an AC voltage source (*Krohn-Hite 4400A* or *4402B* oscillators), pre-amplification of the signals (*EG&G Brookdeal 5002* current pre-amplifier; *HMS Elektronik 568* differential voltage pre-amplifier) and lock-in amplifiers (*Perkin Elmer Instruments 7265* digital lock-in). DC voltages were provided by a digital-analog-converter (*IOTech DAC488/4*). Wherever possible, the measurement circuit had only one electrical ground, in order to avoid ground-loops and noise pick-up from the environment (50 Hz from the mains power and radio-frequency broadcasting). This was made possible by using pre-amplifiers powered by lead-acid batteries and voltage sources (oscillator and DAC) with floating terminals. To protect the device from transients or accidental discharges, low-pass *RC* filters were used on all the connections to the gates. A computer (*Acorn*

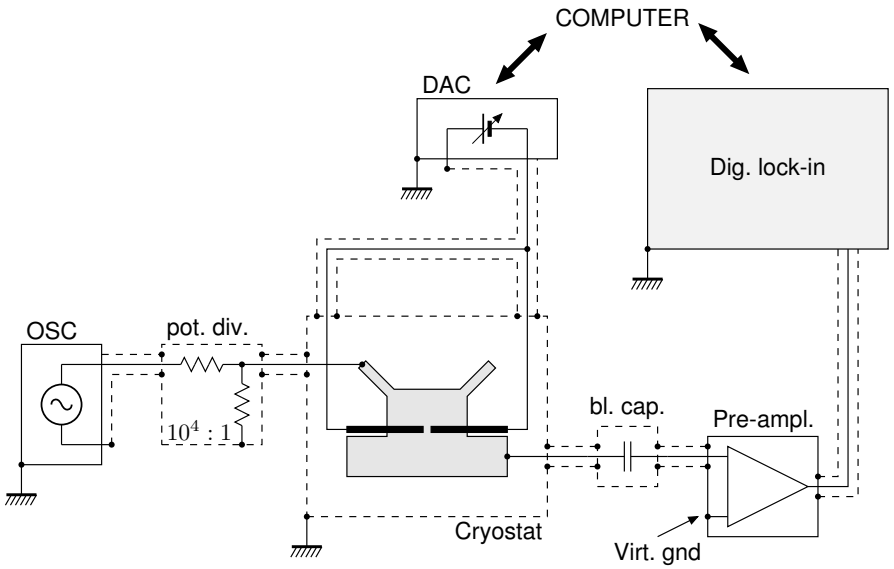

Figure 4.7: Setup for the two-terminal conductance measurement of a split-gate device. "OSC" is the oscillator providing a voltage which is reduced by the potential divider from 100 mV to 10 µV (typical values). The current is measured by the pre-amplifier (with a typical amplification of 10^7 V/A), to the left of which is a blocking capacitor (typical values 43 or 162 µF) that prevents any DC voltage from the pre-amplifier being applied to the sample. The pre-amplifier is powered from a battery pack, and its output is fed into a digital lock-in amplifier. The lock-in is locked on the same frequency (typically 18 Hz) as the voltage from the oscillator. The gate voltage V_g is varied using a *digital-analog converter* (DAC). Both the lock-in and the DAC communicate via GPIB with a computer, which controls the gate voltage and records the measurements.

RiscPC700, running *CryoMeas* written by Dr. C. Ford) was used to control the measurements and record the data.

4.2.1 Characterization

Initial measurements are carried out in a dipping dewar to test a device and determine the characteristics of the 2DEG and the split-gates. Testing includes checking the ohmic contacts and the leakage of the gates. The next step is to measure the conductance of each split-gate as a function of gate voltage, using the configuration shown in Fig. 4.7. Although 4.2 K is typically too high to resolve the quantized 1D subbands, the conductance measurements can tell whether the split-gates operate as expected, for example, finding the gate voltage where the 1D channel is defined and where pinch-off occurs.

Once a device has been selected for the experiments, a proper characterization of the split-gates requires measurement of the equilibrium conductance $G = I/V$

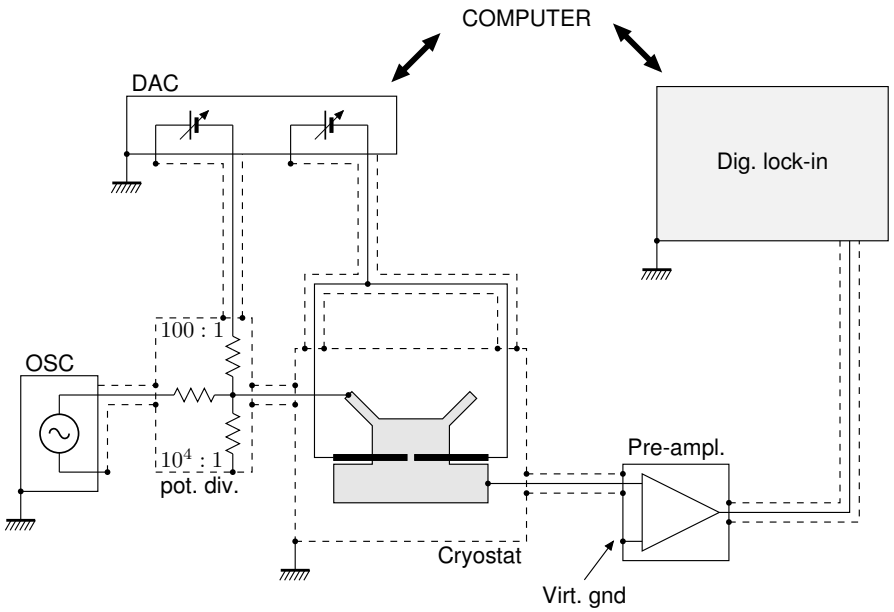

Figure 4.8: Typical configuration for the measurement of the non-linear two-terminal differential conductance of a split-gate. The setup is basically the same as in Fig. 4.7, except there is no blocking capacitor between the device and the pre-amplifier. One channel of the DAC provides the source-drain voltage V_{sd} (which is added to the AC voltage from the oscillator in the potential divider).

at temperatures where the subbands are resolved. This is achieved by carrying out the conductance measurements in the ^{3}He cryostat $T \approx 0.3$ K, or in the ^{3}He/^{4}He dilution refrigerator at $T \approx 0.05$ K. In order to keep the system in the linear-response regime, only small voltages can be applied to the device (0.3 K $\cong$ 30 µV). Typically an *excitation voltage* of 10 µV is used, which gives a current of approximately 10 nA (the resistance of a split-gate is of the order of 10 kΩ).

The next step of the characterization is the measurement of the non-linear conductance (*differential conductance* $G = dI/dV$), using the setup presented in Fig. 4.8. The measurement requires the application of a DC voltage V_{sd} of $1-10$ mV between source and drain, and the measurement of the current in response of a small excitation voltage (typically 10 µV). As explained in Refs. [4–7], the non-linear differential conductance measurements allow the subband spacing to be determined. Also, using the saddle-point potential (Sec. 2.3), it is possible to calibrate the thermopower of the split-gates via Eq. (3.19) (see Section 3.2.2).

In order to characterize the 2DEG, it is necessary to measure both the electron density and the mobility. This is done by measuring the Shubnikov-de Haas oscillations of the resistance of the heating channel while sweeping a magnetic field B, perpendicular to the 2DEG (see, for example, Refs. [8, 9]). Usually the current

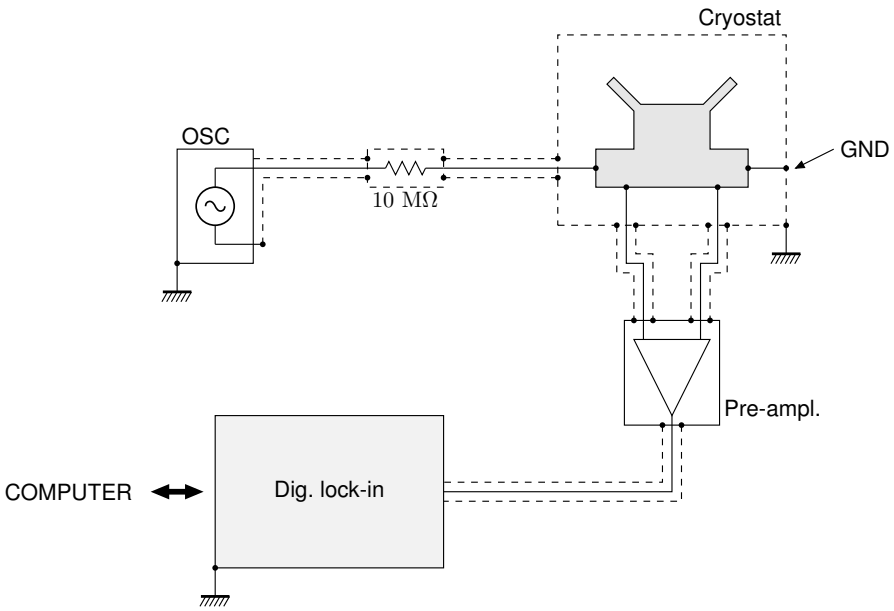

Figure 4.9: Typical configuration for the Shubnikov-de Haas measurement, where the four-terminal resistance of the heating channel is measured as a function of a magnetic field applied perpendicular to the 2DEG. The AC current in the heating channel, typically 10 nA, is fixed by putting a large resistor of 10 MΩ in series with the device. The voltage is measured by the voltage pre-amplifier, with a typical amplification of 100 or 1000, using high-impedance leads. The computer controls the magnetic field and records the measured voltage.

is 10 nA, which, for a heating channel of approximately 100 Ω resistance, gives a measured voltage of 1 mV. The electron density and the mobility are obtained from the zero-field resistance and the periodicity of the magneto-resistance in low fields (up to 2 T).

4.2.2 Thermopower and thermal conductance

In order to measure thermal and thermoelectric effects, a temperature difference is produced between reservoirs of electrons, using the current heating technique (see Sec. 3.3 and Ref. [10]).

Since the heating of the electrons occurs via *Joule heating*, the electron temperature oscillates with the frequency of the dissipated power $P = R_H I_H^2$ (where R_H is the resistance of the heating channel). Therefore, if the heating current I_H has a frequency f, the electron temperature oscillates at a frequency $2f$, shown in Fig. 4.10.

Our measurements of the thermopower follow Ref. [2]. The gate voltage of split-gate B is swept, while split-gate C (the reference) is set on a conductance

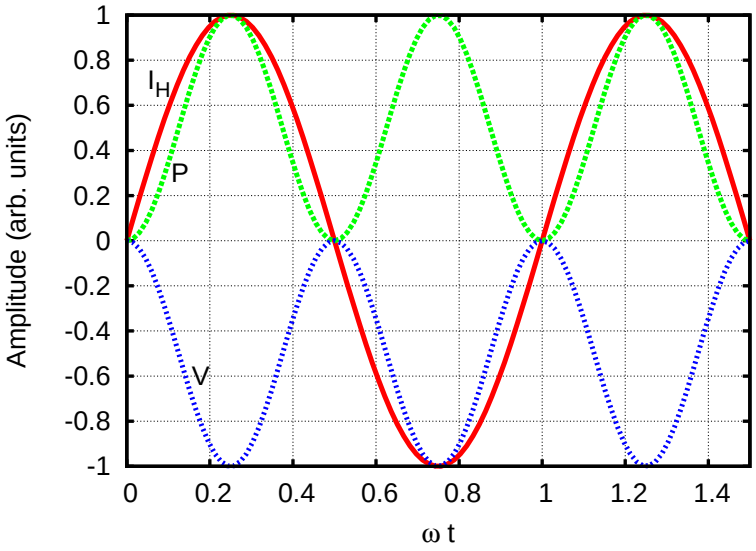

Figure 4.10: Current heating technique. $I_H = I_0 \sin(\omega t)$ is the heating current, $P = R_H I_H^2$ is the power of Joule heating in the heating channel, and $V = -S\Delta T$, where $\Delta T \propto P$, is the thermoelectric voltage. If the AC current that provides the heating of the electrons has a frequency f, the resulting thermal effects (Joule heating and thermoelectric voltage) have a frequency of $2f$.

plateau (which corresponds to zero thermopower, $S_C = 0$). In this configuration the thermovoltage of the electron thermometer (constriction B) due to the temperature difference $T_H - T_L$, is measured without additional thermovoltage contributions from portions of the 2DEG and the wires (see Fig. 4.2). Since the diffusion length of electrons in the 2DEG is of the order of 10 µm, the temperature T_H is uniform over the size of the mesoscopic structures.

Figure 4.11 shows the measurement setup, where the heating current I_H is provided by an oscillator and a 100 kΩ resistor. For currents between 0.1 µA and 10 µA, the temperature differences $T_H - T_L$ are of the order of 0.05−5 K (depending on the lattice temperature T_L). For a typical thermopower $S \approx -20$ µV/K (at 1 K), this results in thermovoltages of $V_{th} = 1 - 100$ µV, that are measured by the differential voltage pre-amplifier.

The principle of the thermal conductance measurements has been explained in Section 4.1.1, and follows that presented in Ref. [1], but with an improved design. As in Ref. [1], the temperature T_{box} is the direct result of heat conduction through constriction A. The main improvement to the design is a well defined temperature

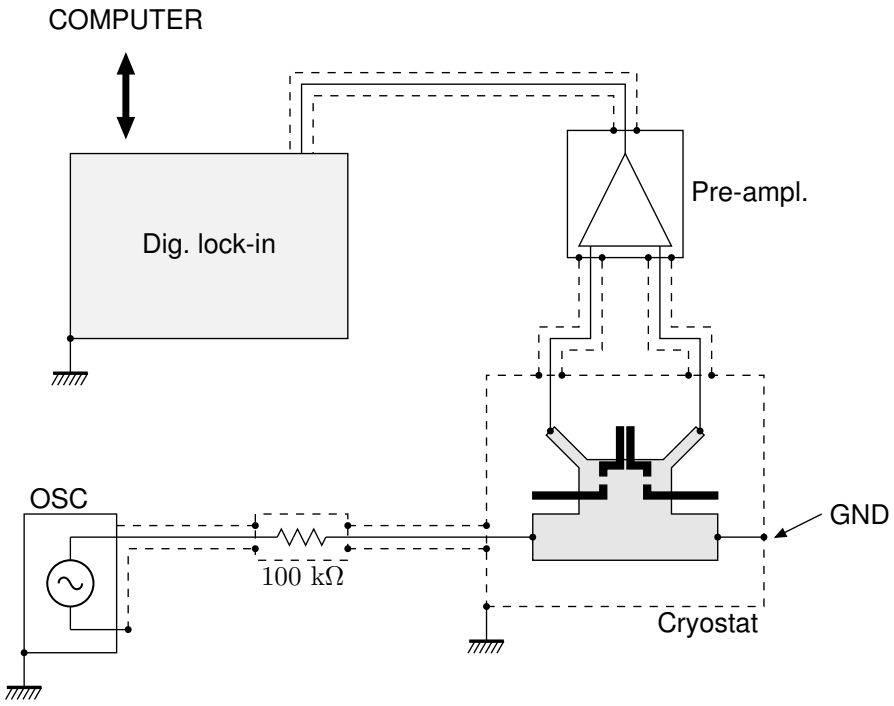

Figure 4.11: Typical configuration for thermopower measurements. The current in the heating channel I_H is provided by the oscillator and the 100 kΩ resistor (typically $I_H = 0.1 - 10$ µA). The corresponding Joule heating in the heating channel ($R_H \approx 100\,\Omega$) is $P = R_H I_H^2 = 1{-}10^4$ pW. The thermoelectric voltage V_{th} is measured using a differential pre-amplifier with high-impedance probes (typically $V_{th} = 0.1{-}10$ µV). The digital lock-in amplifier is locked at $2f$, twice the frequency of the heating current. Both the DAC that controls the gate voltages and the connection between the oscillator and lock-in have been omitted for simplicity.

T_{box}, which is uniform in the thermal box.

Split-gate B (the "thermometer") is set at a local maximum of the thermopower, so that Eq. (3.19) is used as a calibration of the measured thermovoltage. Split-gate C is again set on a conductance plateau, where $S_C = 0$. The electrical conductance G is compared the thermal conductance κ, allowing a quantitative test of the Wiedemann-Franz law (3.17c). The setup for the measurement of the thermal conductance is the same as for the thermopower, but with the addition of the main constriction. The typical configuration is is shown in Fig. 4.12.

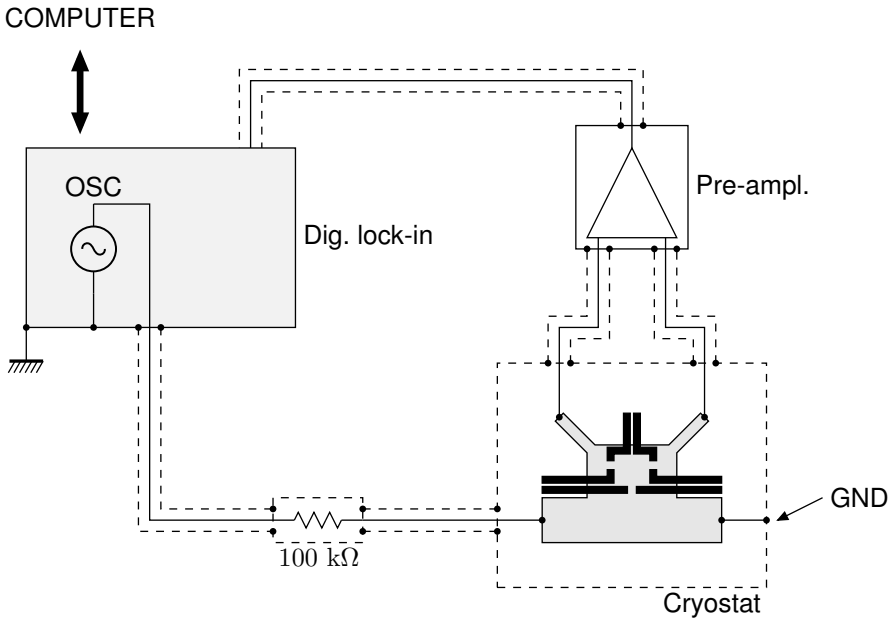

Figure 4.12: Typical configuration for the thermal conductance measurements. The setup is essentially the same as for thermopower measurements, see Fig. 4.11, with the addition of the main split-gate, whose voltage is controlled by the DAC (not depicted). The internal oscillator of the lock-in amplifier is used, so that the voltage can be controlled by the computer (allowing changes of the heating current I_H).

Bibliography

[1] L. W. Molenkamp, T. Gravier, H. van Houten, O. J. A. Buijk, M. A. A. Mabesoone, and C. T. Foxon, *Phys. Rev. Lett.* **68**, 3765 (1992).

[2] N. J. Appleyard, J. T. Nicholls, M. Y. Simmons, W. R. Tribe, and M. Pepper, *Phys. Rev. Lett.* **81**, 3491 (1998).

[3] N. J. Appleyard, J. T. Nicholls, W. R. Tribe, M. Y. Simmons, and M. Pepper, *Physica E* **6**, 534 (2000).

[4] L. I. Glazman and A. V. Khaetskii, *Europhys. Lett.* **9**, 263 (1989).

[5] N. K. Patel, L. Martin-Moréno, M. Pepper, R. Newbury, J. E. F. Frost, D. A. Ritchie, G. A. C. Jones, J. T. M. B. Janssen, J. Singleton, and J. A. A. J. Perenboom, *J. Phys.: Cond. Matt.* **2**, 7247 (1990).

[6] N. K. Patel, J. T. Nicholls, L. Martin-Moréno, M. Pepper, J. E. F. Frost, D. A. Ritchie, and G. A. C. Jones, *Phys. Rev. B* **44**, 13549 (1991).

[7] L. Martin-Moréno, J. T. Nicholls, N. K. Patel, and M. Pepper, *J. Phys.: Cond. Matt.* **4**, 1323 (1992).

[8] D. K. Ferry and S. M. Goodnick, *Transport in Nanostructures* (Cambridge University Press, Cambridge, 1997).

[9] S. Datta, *Electronic Transport in Mesoscopic Systems* (Cambridge University Press, Cambridge, 1995).

[10] M. C. Payne, R. A. Davies, J. C. Inkson, and M. Pepper, *J. Phys. C* **16**, L291 (1983).

Chapter 5

Thermal conductance measurements

In this chapter the results of the thermal conductance measurements will be presented and discussed. The principle and the setup of the measurements are explained in detail in the previous chapter, but will be presented briefly here as a reminder. The measurements for each sample are presented and discussed separately, because each sample has its own peculiar characteristics that make a comparison with the theory problematic. The samples are presented in chronological order, and we will see that there is a progression where the experimental results get closer to the theory. At the end of the chapter we present the conclusions that can be reached based on the measurements.

5.1 Setup and sample characteristics

Figure 5.1 is a schematic representation of the device, where the current I_H in the "heating channel" heats the electrons to a temperature T_H. Heat flows through the constrictions A, B and C, and some heat is also lost to the lattice by the electron-phonon interaction. The temperature of the electrons in the "thermal box", T_{box}, is determined by balancing the heat flows in and out of the box:

$$\kappa_A(T_H - T_{box}) = (\kappa_B + \kappa_C)(T_{box} - T_L) + \dot{Q}_{el-ph}(T_{box}, T_L), \tag{5.1}$$

where T_L is the lattice temperature, $\dot{Q}_{el-ph}(T_{box}, T_L) = N_{el}\,(F(T_{box}) - F(T_L))$ is the heat lost via the electron-phonon interaction, and N_{el} is the number of electrons in the box. T_{box} is uniform throughout the box, because the scattering time for electron-electron interactions is much smaller than the time necessary for an electron to travel from one constriction to another ($d \approx 5$ µm), and the average scattering time for electron-phonon interaction[1].

In a measurement, split-gate B (the thermometer) is held at a constant gate voltage V_g on a peak in the thermopower, corresponding to $G_B = (N_B + \frac{1}{2})(2e^2/h)$ in the electrical conductance (N_B is the subband index; typically $N_B = 1$). Split-gate C (the reference) is held on a conductance plateau $G_C = N_C(2e^2/h)$ (N_C is the subband index; typically $N_C = 1$). The electron temperature T_{el} is then determined by measuring the thermovoltage between B and C:

$$V_{th} = (|S_B| + |S_C|) \cdot (T_{el} - T_L) = |S_B| \cdot (T_{el} - T_L), \tag{5.2}$$

where $S_C = 0$ because C is held on a conductance plateau. The calibration (3.19) of the thermopower of S_B yields

$$V_{th} = \left(c^* \frac{T_{el} + T_L}{2} \right) \cdot (T_{el} - T_L) = c(T_{el}^2 - T_L^2), \tag{5.3}$$

where $c = c^*/2 = (\pi^2 {k_B}^2/6e\hbar\omega_x)(N_B + \frac{1}{2})^{-1} = (19.2/[\hbar\omega_x]_{\mathrm{meV}})(N_B + \frac{1}{2})^{-1}$ µV/K^2 is a calibration constant that depends on the properties of constriction B, and is determined by the calibration (see also Sec. 3.2.2). The gate voltage of A, the "main" split-gate, is swept, varying its thermal conductance and hence the amount of heat flowing into the box. We will write V_{th}^{box} and V_{th}^{H} when the thermovoltage measures T_{box} and T_H respectively.

[1] $\tau_{ee} \sim 100$ fs $\ll \tau_{transit} \approx d/v_F \sim 100$ ps $\ll \tau_{eph} \sim 1$ ns.

Table 5.1 summarizes the characteristics of the samples. The electron density n and the mobility μ of the 2DEG are determined by Shubnikov-de Haas measurements. The area of the thermal box A_{box} is obtained from the lithographic dimensions of the gates defining it, and the box contains $N_{el} = n \cdot A_{box}$ electrons.

L and W are respectively the lithographic length and width of the split-gates. The thermometer constriction is calibrated by determining the parameters for the saddle-point potential $\hbar\omega_x$ and $\hbar\omega_y$, using non-linear electrical conductance measurements. The calibration constant c is given for $N_B = 1$, which is the typical situation.

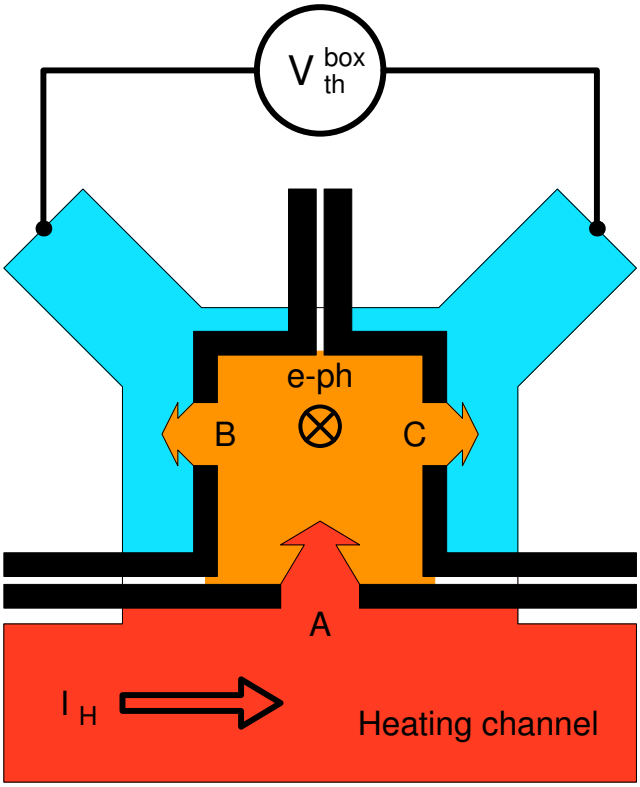

Figure 5.1: Schematic of the thermal box. The box (in orange) is defined by the three split-gates A, B and C (in black), where the thermal conductance $\kappa(V_g)$ of A, the main constriction, will be measured. B is the thermometer: its thermopower is used to measure the electron temperature in the box. C is the reference: it provides a reference for the thermovoltage measurements, removing spurious voltages on the 2DEG.
The electrons in the heating channel (in red) are heated by a current I_H. The heat flows through the constrictions as depicted, and *e-ph* is the heat lost to the lattice by electron-phonon interaction in the box. The electron temperature in the box, T_{box}, is measured from the thermovoltage V_{th}^{box} between B and C.

The electron-phonon interaction is estimated to be [1–3]

$$F(T) = 270 \cdot T^5 \cdot \left(\frac{n}{10^{11}\ \mathrm{cm}^{-2}}\right)^{-\frac{3}{2}},$$

so the heat lost to the phonons is given by $\dot{Q}_{el-ph}(T_{box}, T_L) = N_{el}\,(F(T_{box}) - F(T_L)) = b(T_{box}^5 - T_L^5)$ eV/sK^5. For $T_L = 0.3$ K and $T_{box} = 0.4$ K, $\dot{Q}_{el-ph}(T_{box}, T_L) \sim 10^4$ eV/s. Under the same conditions, the heat flow through a 1D constriction is $\dot{Q} = \kappa(T_{box} - T_L) = L_0 G\overline{T} \cdot (T_{box} - T_L) \approx 4 \times 10^6$ eV/s, with $G = 2e^2/h$ and $\overline{T} = \frac{1}{2}(T_L + T_{box})$. Therefore, the heat lost via the electron-phonon interaction is expected to be orders of magnitude less than the heat transmitted through constrictions B and C.

Sample	**I**	**II**	**III**
n (10^{11} cm^{-2})	2.5	3.2	3.0*
μ (10^6 cm^2/Vs)	3.3	1.4	4.6*
A_{box} (µm^2)	35	15	60
N_{el} (1000)	87.5	48.0	180
b (10^6 eV/s)	6	2.3	9.4
L (µm)	0.50	0.8	0.50
W (µm)	0.63	0.8	0.63
$\hbar\omega_x$ (meV)	0.80	n. a.	1.0
$\hbar\omega_y$ (meV)	1.7	n. a.	3.7
c (µV/K^2)	16	n. a.	12.8

Table 5.1: Overview of the sample characteristics.
The (*) marks n and μ that were not obtained from Shubnikov-de Haas measurements of the sample, but from the general characteristics of the wafer. The characterization of the thermometer constriction could not be done for sample II. The parameter c is given for $N_B = 1$.

5.2 Sample I

Sample I was the first device measured. We will see that the measured $V_{th}^{box}(V_g)$ curves show the effect of 1D quantization in the main constriction. We will also see that the experimental $T_{box}(V_g)$ curves do not match the theory, and this discrepancy will be discussed. Then we will discuss the other features of the measured $\kappa(V_g)$, in particular the unexpected reduction in κ at the 0.7 structure. Finally, we will show that the sample design used in this work is superior to earlier designs [4].

5.2.1 Results

Measurements were performed at constant lattice temperature in the range $T_L \approx 0.3 - 1.2$ K. Figure 5.2 shows the $V_{th}^{box}(V_g)$ curves taken at $T_L = 0.315$ K for fixed heating currents I_H between 0.89 and 7.08 µA. The thermovoltage curves show three plateaux at $V_g \approx -1.6,\ -1.4,\ -1.2$ V, corresponding to the conductance plateaux shown in Fig. 5.4*a*.

The measured $V_{th}^{box}(V_g)$ curves span an order of magnitude in voltage ($V_{th}^{box} \approx 0.1 - 2$ µV), and to highlight similarities and differences between them, each curve has been normalized by dividing it by the thermovoltage measured on the first plateau ($V_g \approx -1.6$ V). In the linear regime the normalized curves are expected to collapse onto a single curve (see Ref. [1] for the analogous behaviour of thermopower measurements). Figure 5.3 shows that the linear regime occurs for $I_H < 2$ µA ($T_H \leq 0.5$ K).

Figure 5.4*b* shows the $V_{th}^{box}(V_g)$ traces of Fig. 5.2 after normalization. As expected, the curves overlap near the first plateau, but show a greater spread for higher subbands ($V_g \gtrsim -1.5$ V). Measurements at higher I_H lie below those at lower current, which is consistent with the increased effect of the electron-phonon interaction at higher electron temperatures (see Section 3.3). The same behaviour is observed in the normalized curves shown in Fig. 5.5.

Figure 5.4*c* shows normalized $V_{th}^{box}(V_g)$ curves taken at T_L between 0.3 K and 0.9 K, and at $I_H = 7.08$ µA. As expected, the curves overlap on the first plateau, but near the second plateau there is a wider spread than in Fig. 5.4*b*; as the lattice temperature increases, the second plateau in the normalized traces goes from ∼1.5 to ∼1.75. Curves measured at higher lattice temperature become more "thermally smeared" with respect to the low temperature curves.

For comparison to the thermal measurements, Fig. 5.4*a* shows the two-terminal conductance $G(V_g)$ of the main split-gate, measured at $T_L \approx 0.3$ K and 1.2 K, and

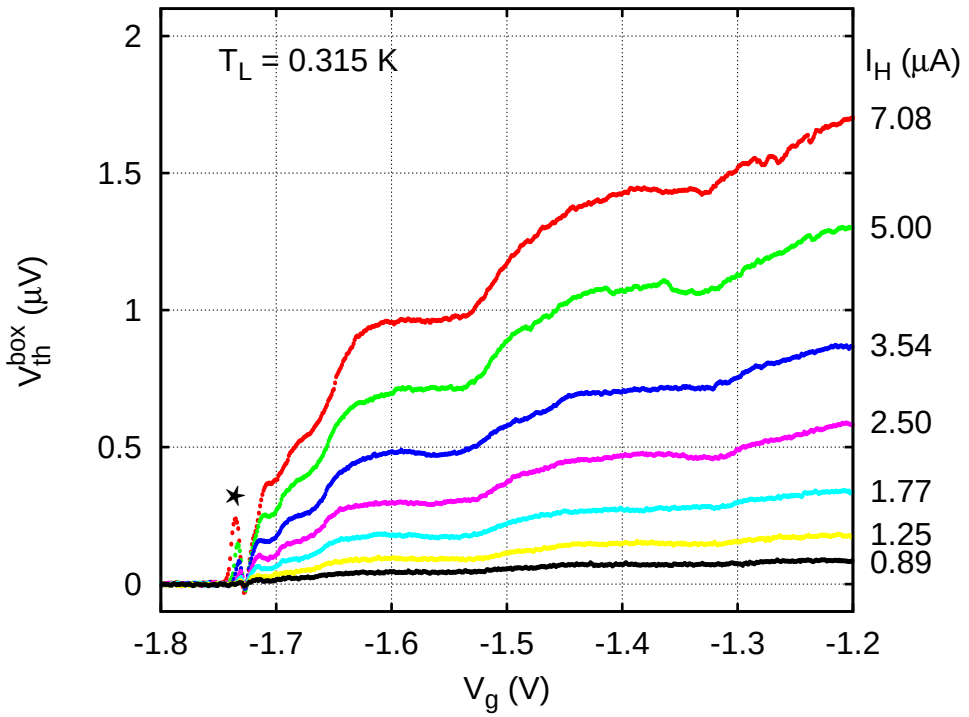

Figure 5.2: $V_{th}^{box}(V_g)$ characteristics of sample I at $T_L = 0.315$ K, for $I_H = 7.08, 5.00, 3.54, 2.50, 1.77, 1.25, 0.89$ μA.
As I_H is increased, T_H becomes larger, and consequently more heat is transmitted into the thermal box through constriction A. At low I_H the curves scale approximately as $V_{th}^{box} \sim I_H^2$, consistent with T_H scaling with Joule heating in the heating channel.
The feature marked with a star (*) is an artefact of the measurement, and is discussed in Sec. 5.13.

which is corrected for a series resistance of $R_s \approx 900\ \Omega$. There is a *0.7 structure* at $V_g \approx -1.675$ V and a small peak at $V_g \approx -1.72$ V, due to an impurity in the constriction. This impurity peak has been used to align the electrical and thermal traces in Fig. 5.4, since they were not measured simultaneously. The alignment required shifts in gate voltage of approximately 0.02 V. When aligned, the following features can be identified in the thermal conductance measurements:

- Plateaux $i = 1,\ 2,\ 3$ are observed at $V_g \approx -1.6,\ -1.4,\ -1.2$ V, respectively, coinciding with the plateaux in $G(V_g)$.
- The 0.7 structure occurs at $V_g \approx -1.675$ V.
- There is an impurity feature at $V_g \approx -1.72$ V.
- There are features between the first and second plateau, similar to the 0.7 structure, but with no correspondence in $G(V_g)$.
- The peaks beyond pinch-off, $V_g \lesssim -1.73$ V, show no corresponding feature in $G(V_g)$.

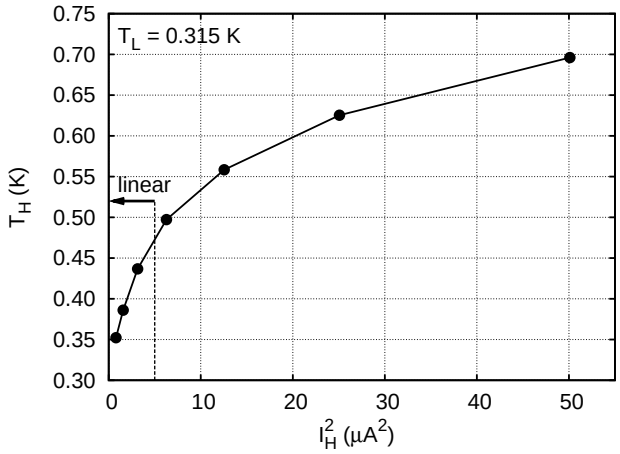

Figure 5.3: T_H as a function of I_H^2 for $T_L = 0.315$ K in sample I.
T_H is determined from V_{th}^H using the calibration of the thermopower (5.2). The heating currents and the lattice temperature are the same as in Fig. 5.2. The regime where the thermopower is linear, i. e. $(T_H - T_L)/T_L \ll 1$ and $V_{th}^H \sim I_H^2$, is indicated by the black arrow.

Figure 5.5 shows normalized $V_{th}^{box}(V_g)$ curves measured at three different lattice temperatures: $T_L = 0.380,\ 0.510,$ and 0.705 K. The behaviour of the curves is consistent with that observed in Figs. 5.4*b* and *c*.

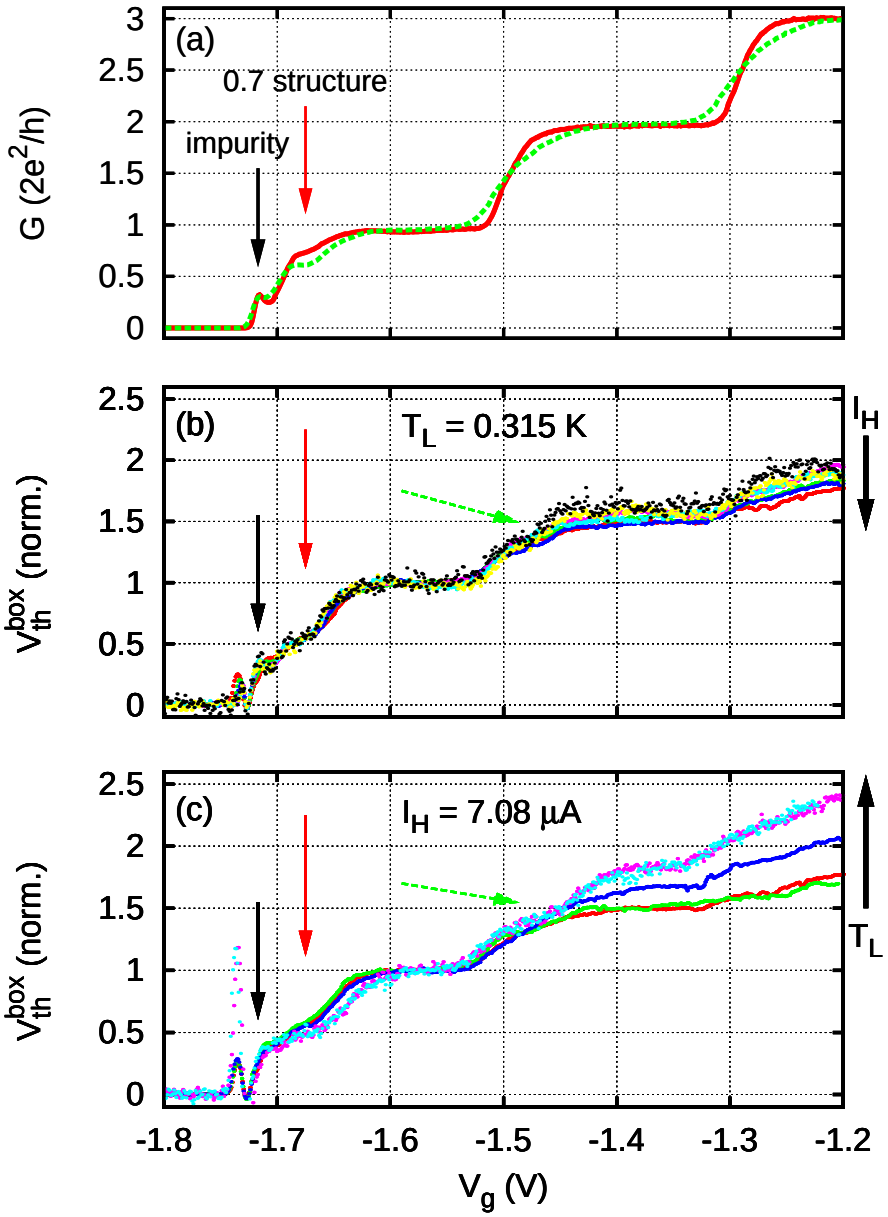

Figure 5.4: Comparison of thermal conductance and electrical conductance measurements for sample I.
(a) $G(V_g)$ of the main split-gate for $T_L = 0.3$ K (solid red curve) and $T_L = 1.2$ K (dashed green curve).
(b) Normalized $V_{th}^{box}(V_g)$ measured at $T_L = 0.315$ K for $I_H = 0.89 - 7.08$ µA (from Fig. 5.2).
(c) Normalized $V_{th}^{box}(V_g)$ measured for $I_H = 7.08$ µA at $T_L \approx 0.3 - 0.9$ K.
The black arrow indicates the "impurity feature", not to be confused with the artefact in $\kappa(V_g)$, which is marked by a star (*) in Fig. 5.2, and which is beyond pinch-off. The red arrow indicates the *0.7 structure* which has a corresponding feature in $\kappa(V_g)$. The green arrow points at features in $\kappa(V_g)$ which have no correspondence in $G(V_g)$, and will be discussed in Sec. 5.4.2.

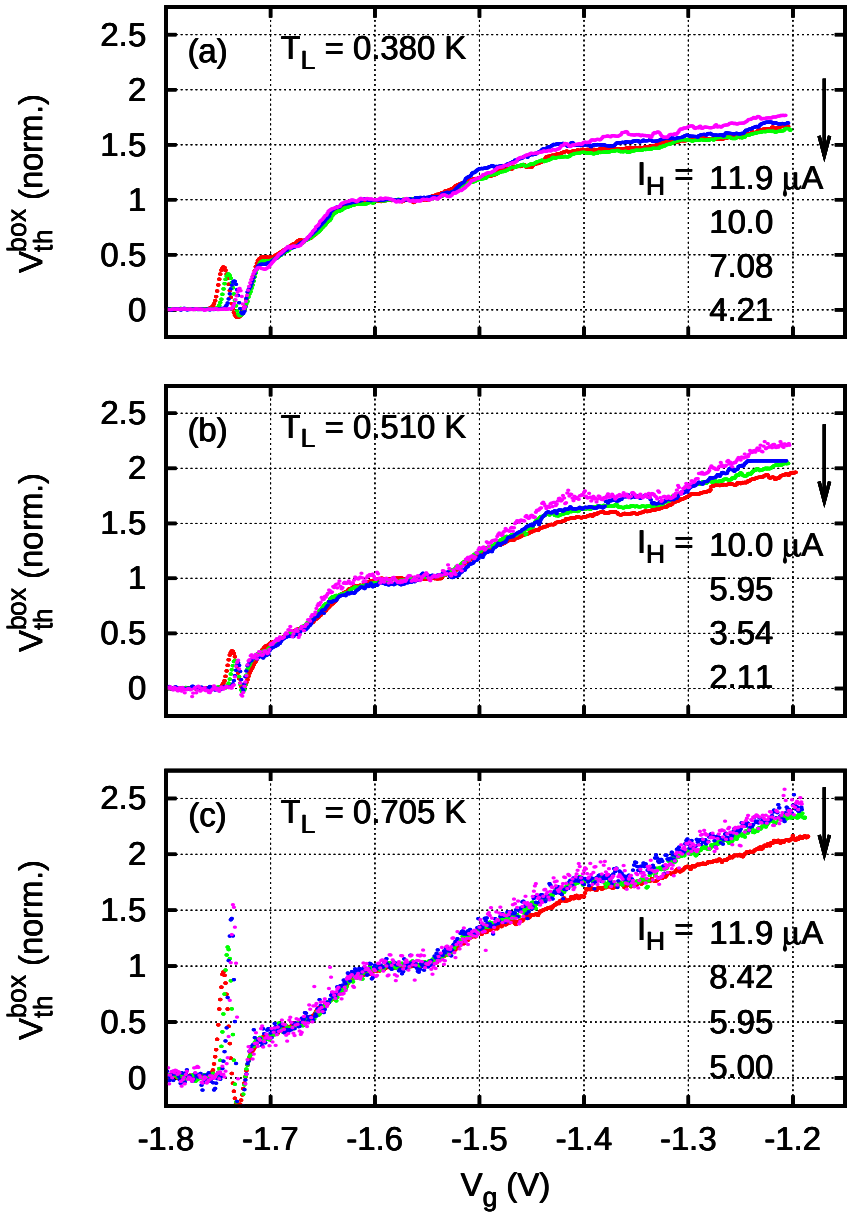

Figure 5.5: Sample I: normalized $V_{th}^{box}(V_g)$ measured at lattice temperatures (a) $T_L = 0.380$ K, (b) 0.510 K, and (c) 0.705 K.
In each figure, curves for four different I_H are presented. On the second plateau, the curves at higher I_H lie below those at lower current, consistent with an increase electron-phonon interaction. The second plateau in the normalized traces goes from ∼1.5 to ∼1.75 with increasing T_L.

5.2.2 Comparison of experiment and theory

The calibration of the thermometer split-gate using Eq. (5.3), allows us to convert the $V_{th}^{box}(V_g)$ characteristics into $T_{box}(V_g)$ curves. The results are then compared to theoretical calculations, where the thermal conductances of the constrictions are calculated by computing the integrals in Eq. (3.14) (see Section 3.2.1). The two-terminal conductance at low temperatures $G(V_g)$ is used as the transmission probability $t(E)$ of the main constriction, and is assumed to be temperature independent. The parameters obtained from the calibration of the thermometer split-gate have been used for the reference constriction.[2]

From the calculated thermal conductances, the heat balance equation (5.1) is solved with respect to T_{box} for given T_H and T_L, and theoretical $T_{box}(V_g)$ curves are produced. Figure 5.6 shows $T_{box}(V_g)$ generated from Fig.5.4: on the left are the experimental curves, on the right are the calculated $T_{box}(V_g)$ curves. The theoretical curves are consistently higher than the experimental ones by a factor $\sim$2; similar discrepancies are seen at other T_L in sample I.

The theoretical calculations rely on accurate measurements of both T_L and T_H. Both the sample and the resistance thermometer are in good thermal contact with the liquid ^{3}He. Therefore the accuracy of the measurement reflects the stability of the ^{3}He temperature and the calibration of the thermometer, which can change slightly with time and thermal cycling. The accuracy of T_L is estimated to be 5%.

The accuracy of T_H depends on both the accuracy of T_L and the calibration of S_B. The accuracy of the thermopower calibration is no better than 20% (see Appendix), and determines the accuracy of the temperature measurements. A relative error of 20% is not enough to account for the discrepancies in Fig. 5.6. In the following section we will describe an improved method, which does not depend on the calibration of the thermometer.

[2]The split-gate C is lithographically identical to split-gate B, so the parameters ω_x, ω_y are assumed to be the same.

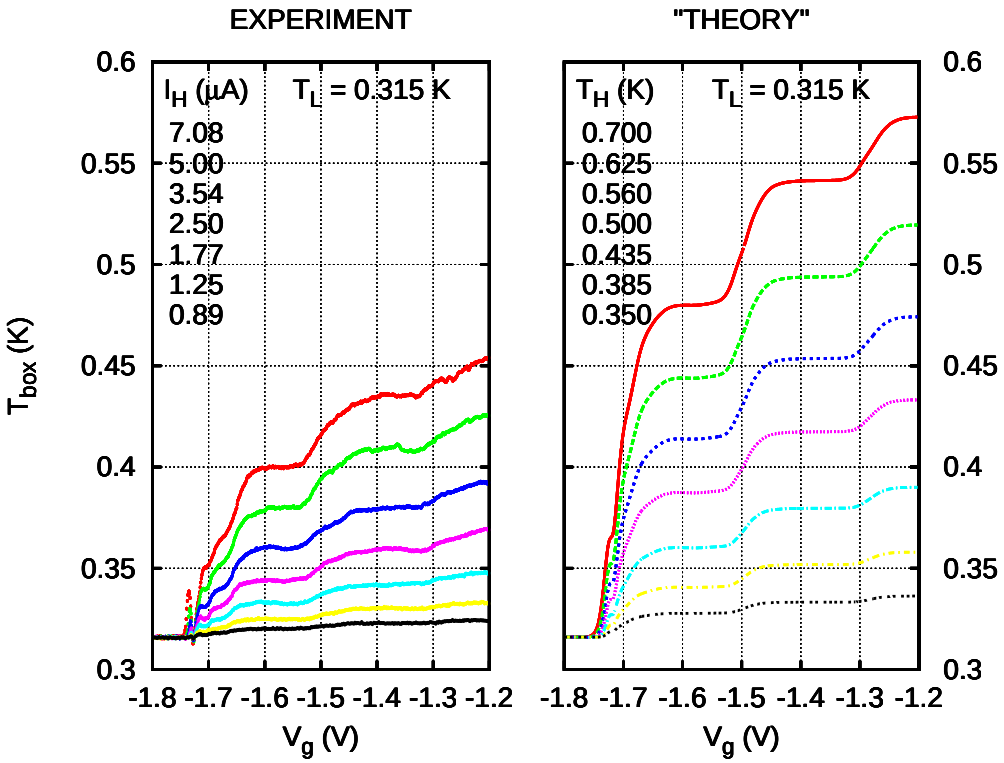

Figure 5.6: Electron temperature T_{box} in the thermal box, as a function of gate voltage V_g on split-gate A.
Left: Experimental temperatures obtained from measurements at $T_L = 0.315$ K (Fig. 5.2), using the calibration of the thermometer constriction given by Eq. (5.3). *Right*: Theoretical temperatures calculated using the values of T_L and T_H at fixed $G_B = 1.5(2e^2/h)$ and $G_C = 2e^2/h$; $G(V_g)$ at $T \approx 0$ K of split-gate A has been used to obtain the transmission probability $t(E)$. The values for T_H on the right correspond to the values of I_H on the left.

5.2.3 Test of the Wiedemann-Franz law

The heat balance equation (5.1) assumes that heat flows through the 1D constrictions or into the lattice. If we assume that each of the constriction has a thermal conductance κ proportional to the electrical conductance G, then

$$\kappa = \alpha\, G\, \overline{T}, \tag{5.4}$$

where α is a constant and $\overline{T}$ is the average of the temperatures on either side of the constriction (see Section 3.2 and Ref. [5]). If α is the same constant for A, B and C, the heat balance equation (5.1) becomes

$$\begin{aligned} \alpha G_A \left(\frac{T_H + T_{box}}{2}\right)(T_H - T_{box}) &= \alpha(G_B + G_C)\left(\frac{T_{box} + T_L}{2}\right)(T_{box} - T_L) + \\ &\quad + \dot{Q}_{el-ph}(T_{box}, T_L). \end{aligned} \tag{5.5}$$

Equation (5.5) can be rewritten as

$$G_A = (G_B + G_C)\frac{T_{box}^2 - T_L^2}{T_H^2 - T_{box}^2} + \frac{2\dot{Q}_{el-ph}(T_{box}, T_L)}{\alpha(T_H^2 - T_{box}^2)}. \tag{5.6}$$

Using the calibration (5.3) of the thermometer split-gate, Eq. (5.6) becomes

$$G_A = (G_B + G_C)\frac{V_{th}^{box}}{V_{th}^H - V_{th}^{box}} + \frac{2\dot{Q}_{el-ph}(T_{box}, T_L)}{\alpha(T_H^2 - T_{box}^2)}, \tag{5.7}$$

where $V_{th}^H = c(T_H^2 - T_L^2)$ is obtained by measuring the thermopower of constriction B when constriction A is not defined. For typical temperatures ($T_L < 1$ K) the heat lost via the electron-phonon interaction is small compared to the heat flowing through the constrictions, so the term containing $\dot{Q}_{el-ph}(T_{box}, T_L)$ in Eq. (5.7) can be neglected, giving

$$G_A = (G_B + G_C)\frac{V_{th}^{box}}{V_{th}^H - V_{th}^{box}}. \tag{5.8}$$

The left-hand side of Eq. (5.8) is the conductance $G_A = G(V_g)$ of the main split-gate. If the Wiedemann-Franz law is valid, $G_A = \kappa_A/L_0T_A = \kappa(V_g)/L_0T(V_g)$, where $T_A = T(V_g) = \frac{1}{2}(T_H + T_{box})$ and L_0 is the Lorenz number (see Section 3.2.1). On the right-hand side, $G_B + G_C = \left((N_B + \frac{1}{2}) + N_C\right)(2e^2/h)$ is constant in a given measurement, and $V_{th}^{box}/(V_{th}^H - V_{th}^{box})$ does not depend on the calibration of the thermometer constriction, but requires that T_L and I_H are kept constant. $G(V_g)$, $V_{th}^{box}(V_g)$, and V_{th}^H, can be measured independently. Therefore, by plotting

$(G_B + G_C)\dfrac{V_{th}^{box}(V_g)}{V_{th}^{H} - V_{th}^{box}(V_g)}$ and comparing it to $G(V_g)$, the Wiedemann-Franz law can be tested, without explicit calibrations. We will write $(\kappa/L_0T)(V_g)$ for the curves obtained using Eq. (5.8).

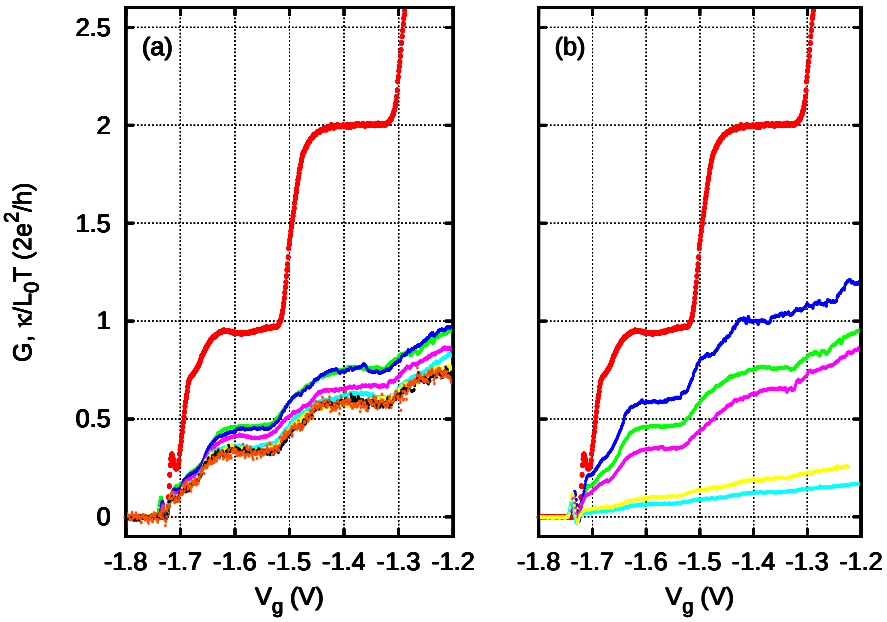

Figure 5.7: Test of the Wiedemann-Franz law for sample I. Eq. (5.8) has been applied to the curves in Fig. 5.4*b* and *c*:
(a) $T_L = 0.315$ K, $I_H \approx 0.9 - 7$ µA.
(b) $I_H = 7.08$ µA, $T_L \approx 0.3 - 0.9$ K.
The electron-phonon interaction has been neglected. If the Wiedemann-Franz law is valid, the $(\kappa/L_0T)(V_g)$ curves are expected to follow the electrical conductance $G(V_g)$ (thick red curve).

The advantage of Eq. (5.8) is that an accurate measurement of the lattice temperature is not necessary, and as long as both V_{th}^{box} and V_{th}^{H} are measured at the same T_L and I_H, the calibration of the thermometers does not enter the equation. However, if heat losses due to the electron-phonon are not negligible, the full expression in Eq. (5.7) has to be used.

The results of applying Eq. (5.8) to sample I are shown in Fig. 5.7. In Fig. 5.7*a* the curves are measured at $T_L = 0.315$ K for different I_H (as in Fig. 5.2 and Fig. 5.4*b*). In Fig. 5.7*b* the curves have the same heating current, $I_H = 7.08$ µA, at different T_L (as in Fig. 5.4*c*). In both figures the thick red curve is the two-terminal

conductance $G(V_g)$ of the main split-gate, and all the other curves are $(\kappa/L_0T)(V_g)$, as calculated using the right-hand side of Eq. (5.8); if the Wiedemann-Franz law is valid, all the curves should follow $G(V_g)$. The experimental curves in Fig. 5.7*a* are about a factor $\sim$2 lower than the expected curve $G(V_g)$, similar to Fig. 5.6. In Fig. 5.7*b* the experimental curves are also lower than expected, but there is no consistent pattern in the discrepancies.

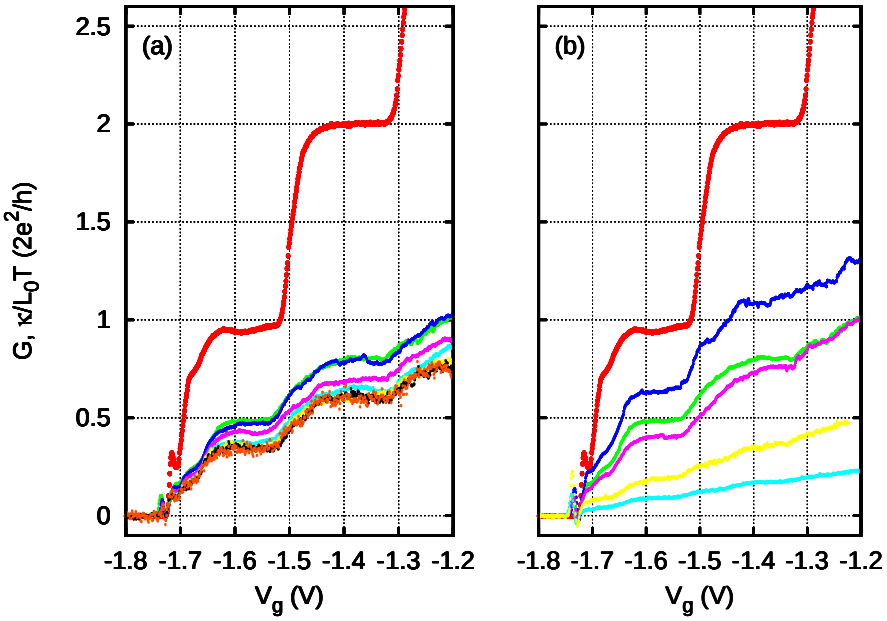

Figure 5.8: Test of the Wiedemann-Franz law for sample I, including the electron-phonon interaction. Eq. (5.7), which includes the heat losses to the lattice, has been applied to the curves in Fig. 5.4*b* and *c*:
(a) $T_L = 0.315$ K, $I_H \approx 0.9 - 7$ µA.
(b) $I_H = 7.08$ µA, $T_L \approx 0.3 - 0.9$ K.
The curves in this figure differ from the corresponding curves in Fig. 5.7 by less than 10% for $T_L \lesssim 0.5$ K; with increasing lattice temperature the difference goes up to 100% (for the trace at $T_L \approx 0.9$ K).

Figure 5.8 shows the result of including the electron-phonon interaction into the data analysis (Eq. (5.7)). The curves of Fig. 5.7 are changed by 10% for $T_L \lesssim 0.5$ K, and the difference increases up to 100% for the curve at $T_L \approx 0.9$ K.

The major discrepancy between experiment and theory is that T_{box} is lower than predicted. By using Eq. (5.8), an inaccurate calibration of the thermometers is ruled out, but other reasons could be:

- a breakdown of the Wiedemann-Franz law in a 1D constriction, or
- a greater heat flow out of the thermal box than expected, or
- a smaller heat flow into the thermal box than expected.

Breakdown of the Wiedemann-Franz law

Equations (5.7) and (5.8) assume that κ is proportional to G and T, as in Eq. (5.4), with the same constant of proportionality α for all constrictions. If $\alpha \neq L_0$, it would not affect the validity of Eq. (5.8); however, if the heat losses due to electron-phonon interaction are included, then α could be determined using Eq. (5.7).

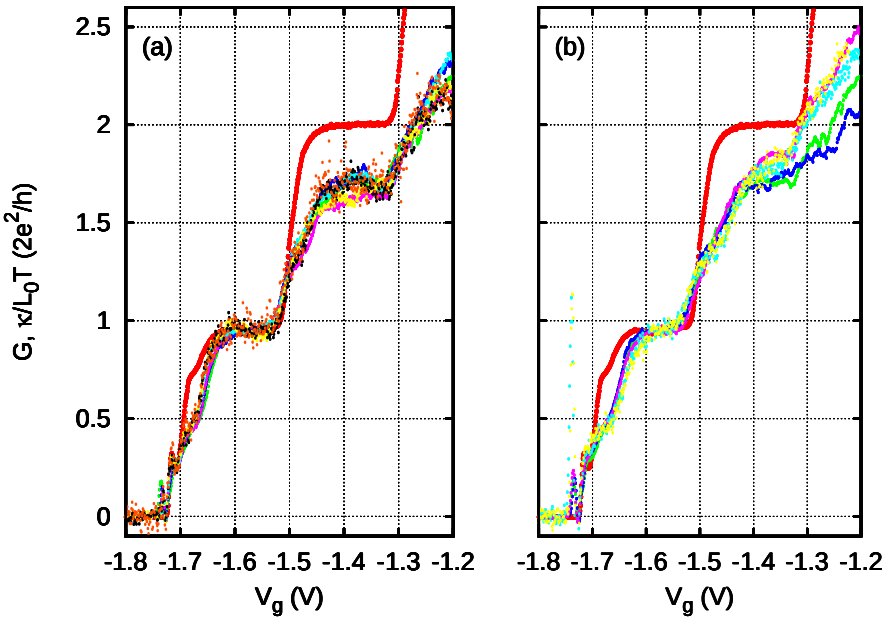

Figure 5.9: Fits of the thermal conductance to the theoretical curve for sample I:
(a) $T_L = 0.315$ K, $I_H \approx 0.9 - 7$ µA.
(b) $I_H = 7.08$ µA, $T_L \approx 0.3 - 0.9$ K.
The experimental curves from Fig. 5.8 have been fitted to the theoretical curve $G(V_g)$, by adjusting a parameter in the second term on the right hand-side of Eq. (5.7). This fitting applies to two situations:
1) the constant α in Eq. (5.4) differs from the Lorenz number, with (a) $\alpha \approx 1.6 - 4.6 \times 10^{-2} L_0$ and (b) $\alpha \approx 2.8 - 12 \times 10^{-2} L_0$;
2) the heat lost via electron-phonon interaction is greater than expected, following Eq. (5.9) with (a) $\beta \approx 22 - 59$, and (b) $\beta \approx 8 - 36$.

Figure 5.9 shows fits to the measurements using the data from Fig. 5.8. At constant T_L (on the left) the $(\kappa/L_0T)(V_g)$ curves fit best to $G(V_g)$ with $\alpha \approx 1.6 - 4.2 \times 10^{-2} L_0$; the fitted α decreases with decreasing I_H. At constant I_H (on the right) the curves fit with $\alpha \approx 2.7 - 11 \times 10^{-2} L_0$, but there is no clear temperature dependence.

Greater heat flow out of the box

A lower T_{box} is consistent with a greater than expected heat flow out of the thermal box. Besides the thermometer and reference constrictions, the other route for heat loss is to the lattice, via the electron-phonon interaction. If we assume that electron-phonon interaction is larger in the thermal box than in a bulk 2DEG by a factor β, then Eq. (5.7) becomes

$$G_A = (G_B + G_C)\frac{V_{th}^{box}}{V_{th}^{H} - V_{th}^{box}} + \beta \frac{2\dot{Q}_{el-ph}(T_{box}, T_L)}{L_0(T_H^2 - T_{box}^2)}. \tag{5.9}$$

Adjusting the factor β to fit the experimental curves to $G(V_g)$ gives the curves shown in Fig. 5.9. At $T_L = 0.315$ K, β is between 22 and 59, and decreases as I_H increases. For the curves measured at $I_H = 7.08$ µA, β is between 8 and 36, but has no defined dependence on temperature.

Smaller heat flow into the box

A lower T_{box} could be due to a lower than expected T_H, resulting in less heat flowing into the thermal box. If T_H is reduced, we can modify Eq. (5.8) by a factor γ:

$$G_A = (G_B + G_C)\frac{V_{th}^{box}}{(\gamma V_{th}^{H}) - V_{th}^{box}}. \tag{5.10}$$

The result of adjusting γ to fit the measured $(\kappa/L_0T)(V_g)$ to $G(V_g)$ is shown in Fig. 5.10. At $T_L = 0.315$ K, γ is between 0.43 and 0.59, and increases with increasing I_H. At $I_H = 7.08$ µA, γ is between 0.13 and 0.74, and does not follow a clear temperature dependence.

Conclusion

An error in the calibration is ruled out by using Eq. (5.8). The other samples do not display the same kind of discrepancy between theory and experiment, and the correction to the experimental curves that fits best the theory is given by

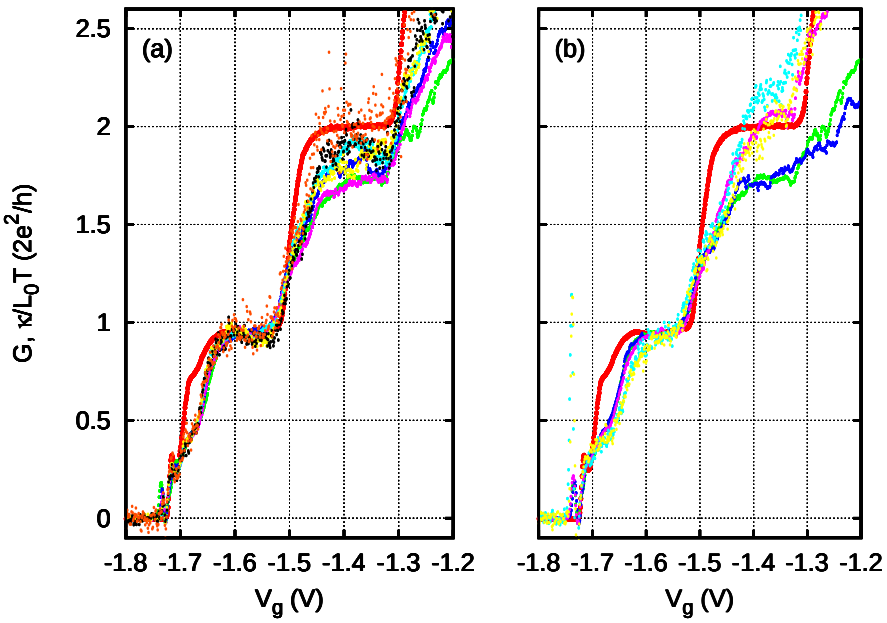

Figure 5.10: Fits of the thermal conductance to the theoretical curve for sample I. The experimental curves from Fig. 5.7 have been fitted to the theoretical curve by adjusting the factor γ in Eq. (5.10):
(a) $T_L = 0.315$ K, $I_H \approx 0.9 - 7$ µA; γ increases from 0.43 to 0.59 with increasing I_H.
(b) $I_H = 7.08$ µA, $T_L \approx 0.3 - 0.9$ K; γ varies between 0.13 and 0.74, with no obvious pattern.

Eq. (5.10). Therefore, the most likely source of the discrepancy is an impurity configuration peculiar to this sample, whose effect is mainly to reduce the amount of heat flowing into the thermal box.

5.2.4 Other features

So far we have focused on the conductance plateaux. In the following we will examine other features.

0.7 structure

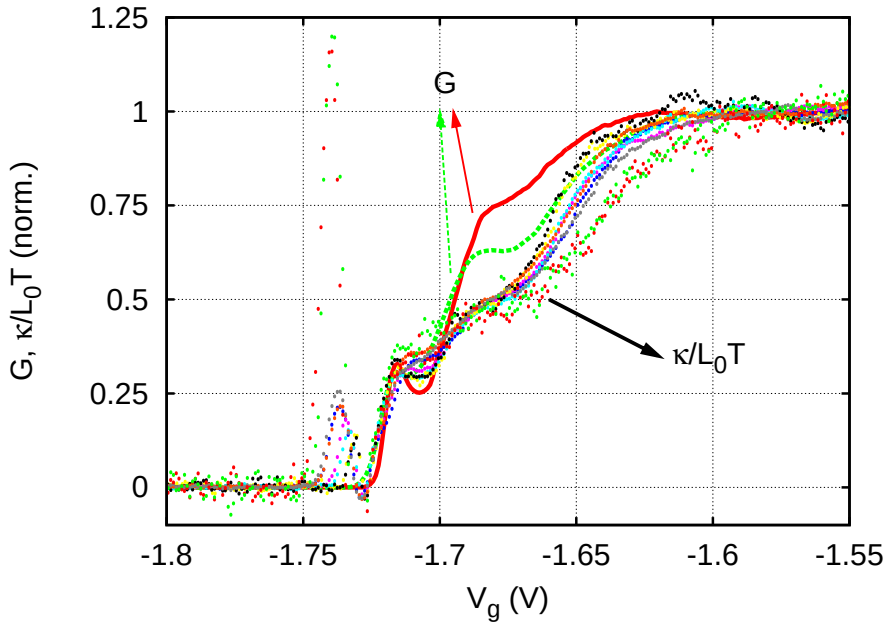

Figure 5.11: Comparison of the thermal measurement $(\kappa/L_0T)(V_g)$ and the electrical conductance $G(V_g)$ for sample I. The thicker curves are the two-terminal conductance $G(V_g)$ at $T_L = 0.3$ K (full, red) and $T_L = 1.2$ K (dashed, green), corrected for a series resistance. The remaining curves are obtained from Eq. (5.7) and are normalized at the first plateau. At $V_g \approx -1.675$ V the *0.7 structure* in the electrical conductance is observed at $G \approx 0.75(2e^2/h)$ for $T_L = 0.3$ K and at $G \approx 0.63(2e^2/h)$ for $T_L = 1.2$ K. In the thermal conductance the corresponding feature is observed at $\kappa/L_0T \approx (0.47 - 0.5)2e^2/h$.

Figure 5.11 shows a selection of κ/L_0T curves for sample I obtained using Eq. (5.7). The experimental data span a range of lattice temperatures and heating currents, and the traces have been normalized on the first plateau. For comparison, the curves are shown with the $G(V_g)$ characteristics measured at $T_L = 0.3$ K and $T_L = 1.2$ K.

In $G(V_g)$ the 0.7 structure appears as a shoulder at $G \approx 0.75(2e^2/h)$ at $T_L = 0.3$ K. At $T_L = 1.2$ K the 0.7 structure has evolved into a small plateau at

$G \approx 0.63(2e^2/h)$, consistent with previous measurements [6–8]. In the thermal conductance, the feature corresponding to the 0.7 structure is observed at $\sim(0.47-0.5)2e^2/h$, with no observable temperature dependence. In Sec. 5.5 we will see that the calculated curves, using $G(V_g)$ as transmission $t(E)$, show the 0.7 structure at $\kappa/L_0T > 0.5(2e^2/h)$.

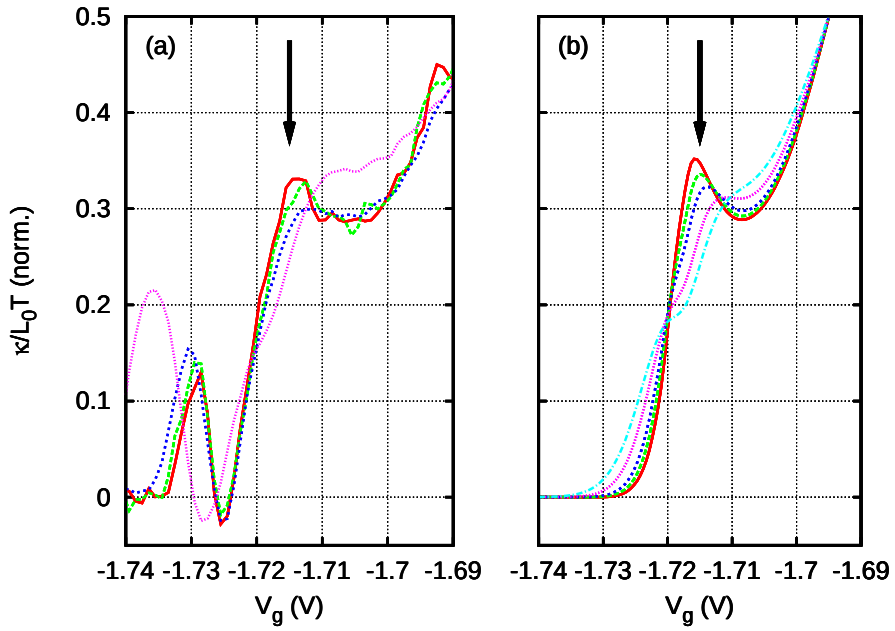

Figure 5.12: The impurity feature (marked with an arrow) observed in $G(V_g)$, is also present in $(\kappa/L_0T)(V_g)$.
(a) experimental κ/L_0T curves obtained from Eq. (5.7) and normalized at the first plateau: $T \approx 0.380$ K, 0.415 K, 0.465 K, and 0.530 K.
(b) κ/L_0T curves calculated using $G(V_g)$ as $t(E)$, for temperatures $T = 0.050$ K, 0.075 K, 0.100 K, 0.150 K, and 0.200 K.
In both cases the temperatures span a range of about 0.150 K, but the average temperature for the theoretical curves is between three and seven times smaller than for the experimental curves. However, the experimental and theoretical curves show the same qualitative behaviour.

Impurity feature

Figure 5.12 shows the measured κ/L_0T and the same quantity calculated from $G(V_g)$ of the main constriction. The experimental curves have been normalized at the first plateau. The evolution of the impurity feature with increasing temperat-

ure is qualitatively the same in the measured curves and the theoretical prediction. However, the theoretical curves have been calculated using temperatures between 0.05 K and 0.2 K, while the experimental curves have temperatures between 0.38 K and 0.53 K.

Past-pinch-off feature

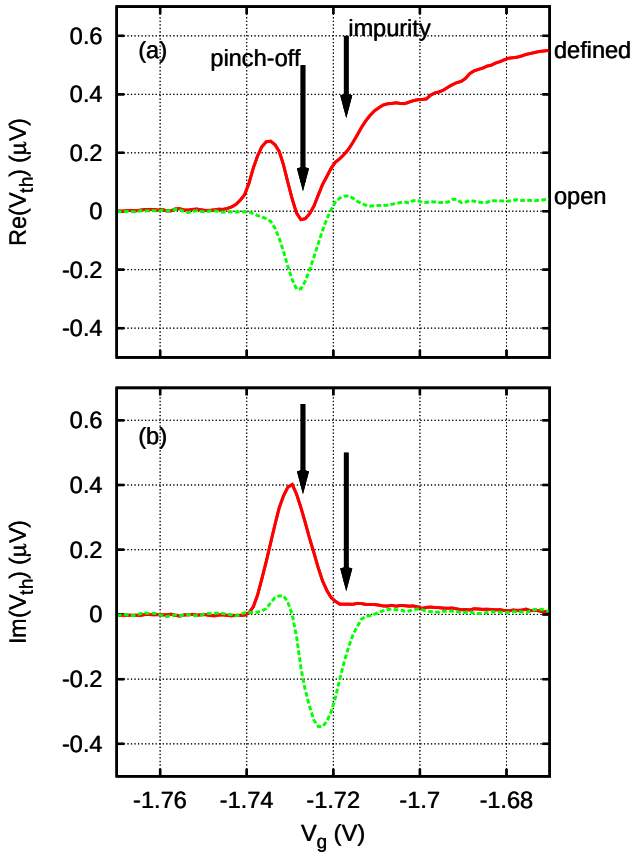

Figure 5.13: Thermovoltage measurements at $T_L = 0.315$ K and $I_H = 7.08$ μA.
(a) The real part of the thermovoltage signal, Re(V_{th}).
(b) The imaginary part of the signal, Im(V_{th}).
The two curves in each plot have been measured in two different situations: the thermal box is defined and the reference split-gate is set on the first conductance plateau (solid red); the reference constriction is not defined and the box is open (dashed green).

In the thermal conductance measurements a feature is observed after the main split-gate has reached pinch-off, at -1.75 V $\lesssim V_g \lesssim -1.73$ V. Figure 5.13 shows that for gate voltages beyond pinch-off, the signal becomes first negative and then

forms a positive peak. The height of this peak is weakly dependent on I_H, but depends more strongly on T_L. Measurements also show a linear dependence of the peak height with the frequency of I_H.

Figure 5.13 shows the in-phase and quadrature thermoelectric voltage, $\mathrm{Re}(V_{th})$ and $\mathrm{Im}(V_{th})$, respectively. The curves are measured in two different situations: in one case (red), the thermal box is defined by setting the reference at the first conductance plateau; in the other case (green), the box is open by keeping C at zero gate voltage. T_H and I_H are the same in both cases, but the feature is qualitatively different.

The facts that the feature is different for open and defined box, that the peak height depends on frequency, and that this feature has been observed in other samples, supports the idea that it is an artefact of the measurement. We interpret this "past-pinch-off feature" as due to the separation of the voltage probes on one side of A, from the electrical earth on the heating channel on the other side of A. The thermovoltage does not go to zero as it should probably due to capacitive coupling between the two regions of the 2DEG separated by A at pinch-off.

Defined thermal box vs open box

In previous measurements [4] of the thermal conductance there was no defined thermal box. Instead it was assumed that a region of uniform electron temperature is defined within $L_D \times W_{ch}$, where L_D is the diffusion length of the electrons in the 2DEG and W_{ch} is the width of the channel as defined by gates. This situation can be reproduced in our sample by putting the gate voltage of the reference split-gate at zero (that is, constriction C is not defined and the thermal box is half open).

In sample I, the diffusion length is $L_D \approx 19$ µm and $W_{ch} = 12-20$ µm, therefore $L_D \times W_{ch} = 200 - 400$ µm^2, much larger than $A_{box} \approx 35$ µm^2. If T_L and I_H are the same, the thermovoltages in the two situations are expected to scale inversely with the area of uniform electron temperature. In this case $(L_D \times W_{ch})/A_{box} \approx 10$, which is consistent with $V_{th}^{box}/V_{th}^{open} \approx 14$, as can be seen in Fig. 5.14.

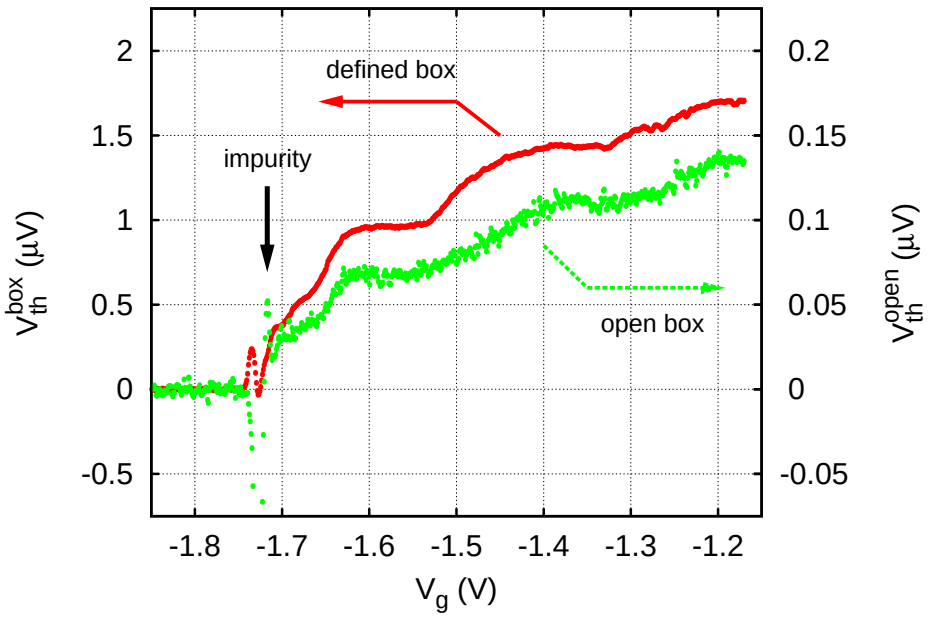

Figure 5.14: Thermovoltage measurements at $T_L = 0.315$ K and $I_H = 7.08$ µA, for two different situations, in sample I.
Defined box: the thermal box is defined, with the reference split-gate set at $G_C = 2e^2/h$; the area of the box is $A_{box} \approx 35$ µm^2.
Open box: the reference constriction not defined, and the electron temperature is uniform over an area of $200 - 400$ µm^2.
The ratio of the signals is $V_{th}^{box}/V_{th}^{open} \approx 14$. The 0.7 structure is at $\kappa/L_0T \approx e^2/h$ in both cases.

5.3 Sample II

Sample II was fabricated with the aim of increasing the thermovoltage as much as possible. The area of the thermal box was reduced to decrease the effect of the electron-phonon interaction, and the length of the split-gates was increased to decrease the $\hbar\omega_x$ parameter and so increase the sensitivity of the thermometer constrictions (according to Eq. (5.3)).

The consequence of bringing the constrictions so close to each other, is that the gate voltage on one split-gate affects the other constrictions. This reduces the range of gate voltages that can be swept on the main constriction, because it affects the thermometer and reference. The lengthening of the split-gates results in the appearance of resonance structures at low temperatures, which makes the calibration of the thermopower unreliable. In addition to these problems, the characteristics showed random telegraph switching [9].

For these reasons, sample II is not very representative of the general behaviour of split-gate devices. However, we observe the same reduction in κ at the 0.7 structure, as in the other two samples.

5.3.1 Results

Measurements were performed at constant lattice temperatures in the range $T_L \approx 0.3-1.2$ K. Figure 5.15 shows the $V_{th}^{box}(V_g)$ curves taken at $T_L = 0.84$ K for heating currents $I_H = 2 - 10$ µA. The curves show plateaux at $V_g \approx -3.05$ and -2.75 V, corresponding to the usual conductance plateaux $i = 1$ and 2, as can be seen in Fig. 5.16.

The measured $V_{th}^{box}(V_g)$ curves span an order of magnitude in voltage ($V_{th}^{box} \approx 0.1 - 1$ µV), and to highlight similarities and differences between them, each trace has been normalized by dividing by the voltage on the first plateau (at $V_g \approx -3.05$ V). Figures 5.16*b* and *c* show the normalized $V_{th}^{box}(V_g)$ characteristics for $T_L = 0.84$ K and $T_L = 0.52$ K, respectively. The normalized curves overlap near the first plateau, but on the second plateau the curves with higher I_H lie beneath the curves for lower I_H, which is consistent with a larger electron-phonon interaction. The height of the second plateau, relative to the first plateau, increases with decreasing lattice temperature, opposite behaviour to that observed in sample I (see Fig. 5.5).

Figure 5.16*a* shows the conductance characteristics $G(V_g)$ of the main split-gate, measured at $T_L \approx 0.3$ K and at $T_L \approx 1.2$ K, and corrected for a series

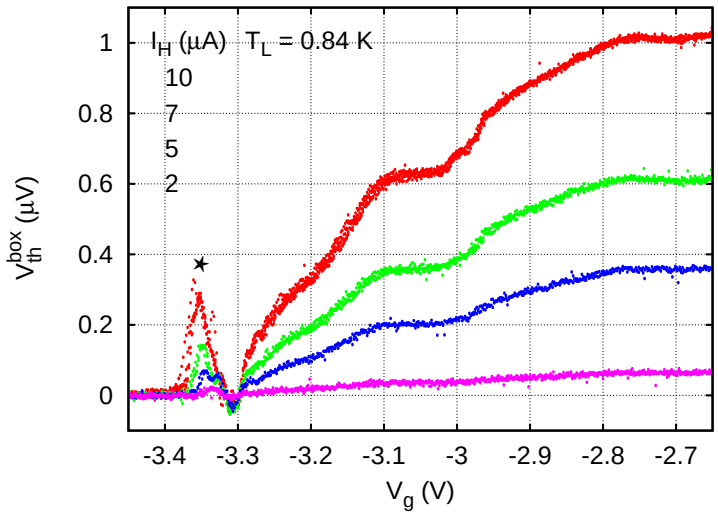

Figure 5.15: $V_{th}^{box}(V_g)$ characteristics of sample II at $T_L = 0.84$ K and $I_H = 10,\ 7,\ 5,\ 2$ μA (from top to bottom). Each curve is the result of plotting several consecutive measurements at the same time.
For $I_H \leq 7$ μA, V_{th}^{box} scales approximately as I_H^2. The feature marked with a star (*) is an artefact of the measurement, as discussed in Sec. 5.2.4.

resistance ($R_s \approx 1800$ and 700 Ω, respectively). The curves are the result of several consecutive measurements, and show that there is *random telegraph switching* (RTS) [9]. The same type of RTS is also present in the $G(V_g)$ characteristics of split-gates B and C. The 0.7 structure is observed at $V_g \approx -3.2$ V: for $T_L \approx 1.2$ K it is at $G \approx 0.63(2e^2/h)$, but for $T_L \approx 0.3$ K it is at $G \approx 0.5(2e^2/h)$. This is not the usual behaviour of the 0.7 structure, and it is most likely due to impurity effects. Also, resonant structures are visible on the conductance plateaux, which are thermally "smeared" in the $G(V_g)$ curve taken at $T_L \approx 1.2$ K. As for sample I, the $\kappa(V_g)$ shows a feature after pinch-off (at $V_g \approx -3.35$ V), which has no corresponding feature in $G(V_g)$.

Figure 5.17 shows three normalized $V_{th}^{box}(V_g)$ characteristics at 1) $T_L = 0.52$ K and $I_H = 5$ μA, 2) $T_L = 0.84$ K and $I_H = 5$ μA, and 3) $T_L = 0.84$ K and $I_H = 10$ μA. The average of the electron temperature on either side of the main constriction, $T_A = \frac{1}{2}(T_{box} + T_H)$, increases from curve 1 to 3. As it does so, the height of the second plateau decreases relative to the first plateau, which is consistent with an increased electron-phonon interaction.

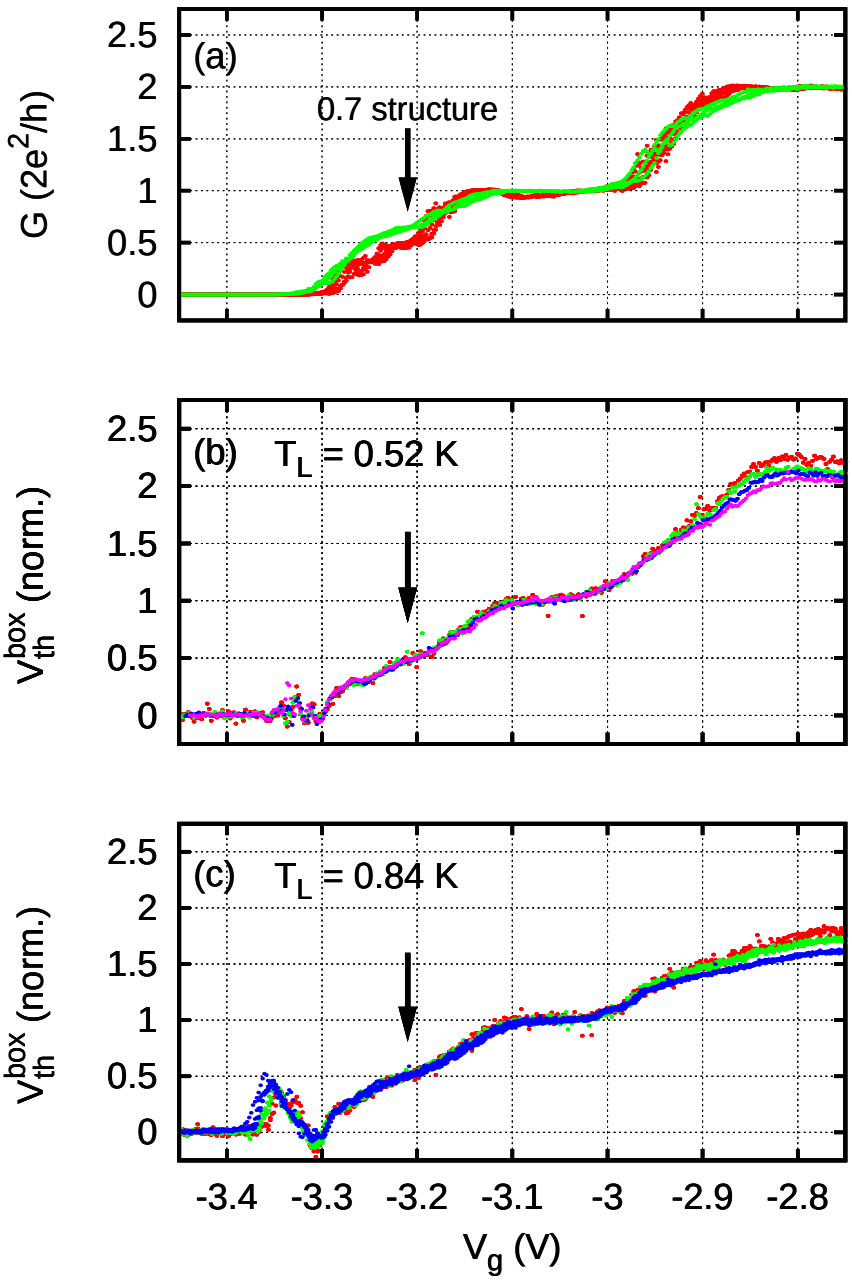

Figure 5.16: Comparison of thermal conductance $\kappa(V_g)$ and electrical conductance $G(V_g)$ for sample II.
(a) $G(V_g)$ measured at $T_L \approx 0.3$ K (red) and $T_L \approx 1.2$ K (green), both corrected for a series resistance
(b) Normalized $V_{th}^{box}(V_g)$ measured at $T_L = 0.52$ K for $I_H = 2 - 5$ µA.
(c) Normalized $V_{th}^{box}(V_g)$ measured at $T_L = 0.84$ K for $I_H = 5 - 10$ µA.
For each trace several consecutive measurements are plotted at the same time.

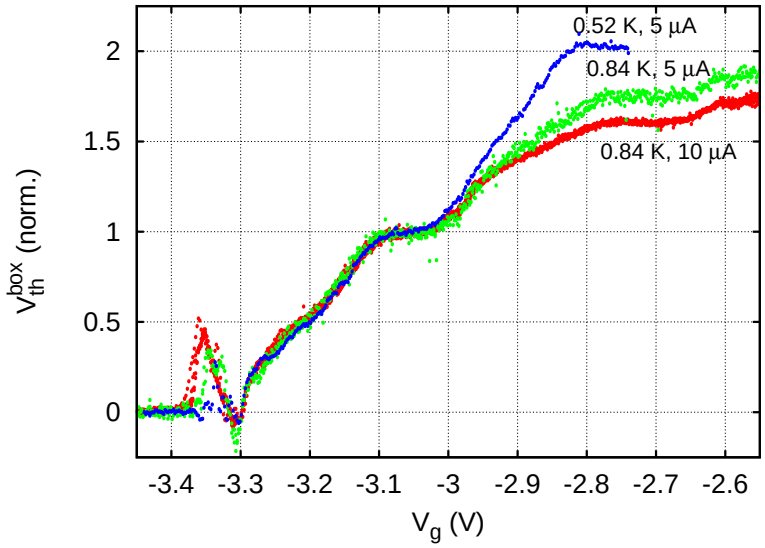

Figure 5.17: Temperature dependence of $V_{th}^{box}(V_g)$ for sample II. The average temperature at the main constriction, $T_A = \frac{1}{2}(T_{box} + T_H)$, increases from the top curve to the bottom curve.

5.3.2 Test of the Wiedemann-Franz law

Since there is no calibration of the thermometer split-gate in sample II, a comparison between theory and experiment as described in Sec. 5.2.2 is not possible. However, it is possible to perform an approximate test of the Wiedemann-Franz law using Eq. (5.8):

$$G_A = (G_B + G_C)\frac{V_{th}^{box}}{V_{th}^{H} - V_{th}^{box}}, \tag{5.8}$$

where $G_A = G(V_g)$ is the electric conductance of split-gate A, G_B and G_C are the electric conductances of B and C (held constant throughout the measurement), and V_{th}^{H} is the thermovoltage measured when A is not defined. The right-hand side of Eq. (5.8) is κ/L_0T of A.

Figures 5.18*a* and *b* show the result of applying Eq. (5.8) to the measurements taken at $T_L = 0.52$ K and $T_L = 0.84$ K. On the first plateau all κ/L_0T traces lie within 25% of the expected curve, $G(V_g)$. The curves with higher heating current I_H lie beneath the curves with lower I_H, which is consistent with the effect of the electron-phonon interaction (neglected in Eq. (5.8)). However, for $V_g \gtrsim -3$ V the (κ/L_0T) traces lie above the theoretical curve, beyond the experimental errors. This discrepancy cannot be explained by the electron-phonon interaction, which

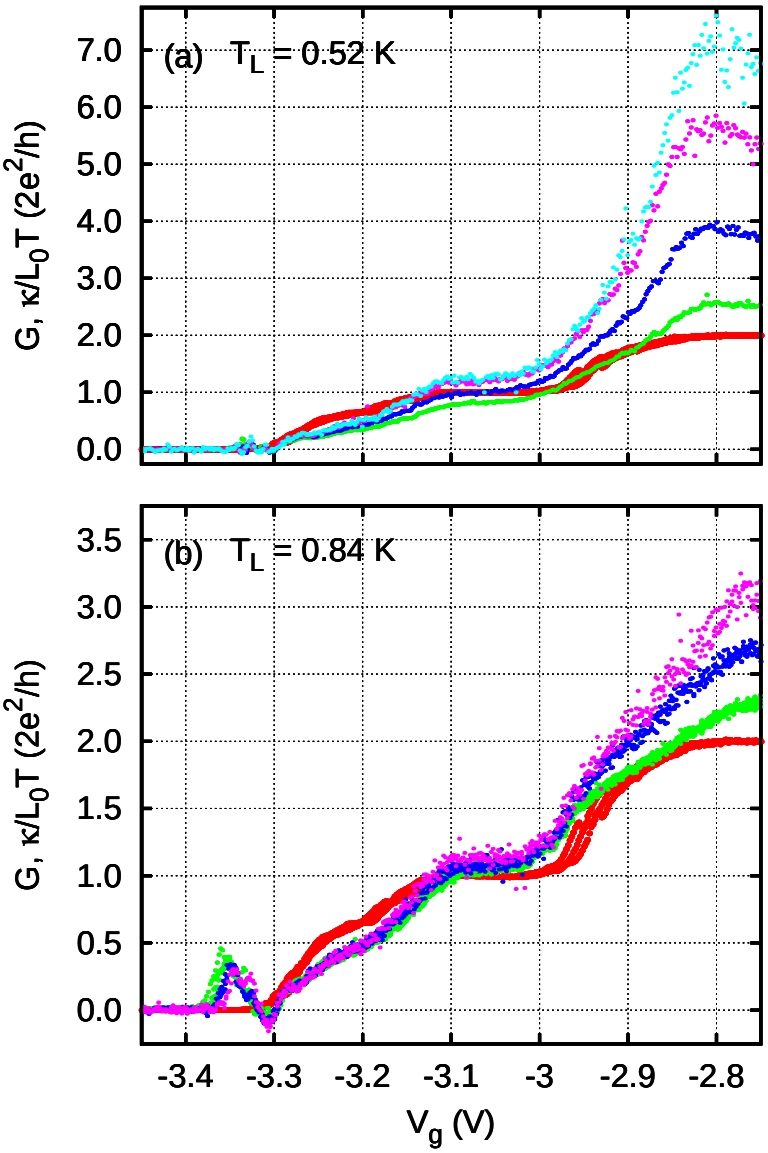

Figure 5.18: Test of the Wiedemann-Franz law for sample II. Equation (5.8) has been applied to the data from Fig. 5.16:
(a) κ/L_0T at $T_L = 0.52$ K for $I_H = 2 - 5$ µA.
(b) κ/L_0T at $T_L = 0.84$ K for $I_H = 5 - 10$ µA.
The thick, red curve is $G(V_g)$, corrected for a series resistance. The feature corresponding to the 0.7 structure is at $V_g \approx -3.2$ V.

would have the opposite effect.

Since the distance between the constrictions is only ∼5 µm, it is possible that the split-gates affect each other via capacitive coupling. It was observed that the characteristic of a split-gate is affected by the gate voltage applied to neighboring split-gates. This *cross-talk* of the split-gates was minimised on the thermometer constriction, by keeping the left half of A at a constant gate voltage. The right half of split-gate A can still affect the reference constriction. If C is not on a conductance plateau, the thermopower is no longer zero and the measured thermovoltage is larger:

$$V_{th}^{box} = (|S_B| + |S_C|) \cdot (T_{box} - T_L) > |S_B| \cdot (T_{box} - T_L).$$

However, S_C increases with increasing I_H, while the observed discrepancy has the opposite behaviour.

It is possible to obtain a better agreement with the expected curve, by modifying Eq. (5.8) as in Eq. (5.10):

$$G_A = (G_B + G_C)\frac{V_{th}^{box}}{\gamma V_{th}^{H} - V_{th}^{box}}, \tag{5.10}$$

where γ is an adjustable parameter. Figure 5.19 shows the result of the free parameter fitting for the curves from Fig. 5.18. The traces for $T_L = 0.84$ K match the expected curves within 15%, using $\gamma \approx 1.06 - 1.19$. For $T_L = 0.52$ K the match is within 25% with $\gamma \approx 1.06 - 1.54$. This is consistent with a measured thermovoltage V_{th}^{H} smaller than expected, possibly due to a variation of electron temperature between the heating channel and the thermometer split-gate. However, the diffusion length of the 2DEG is about 9 µm, twice the length of the thermal box, which means that the electrons should have a uniform temperature over an area much larger than the thermal box. Therefore, the discrepancy between experiment and theory is not understood.

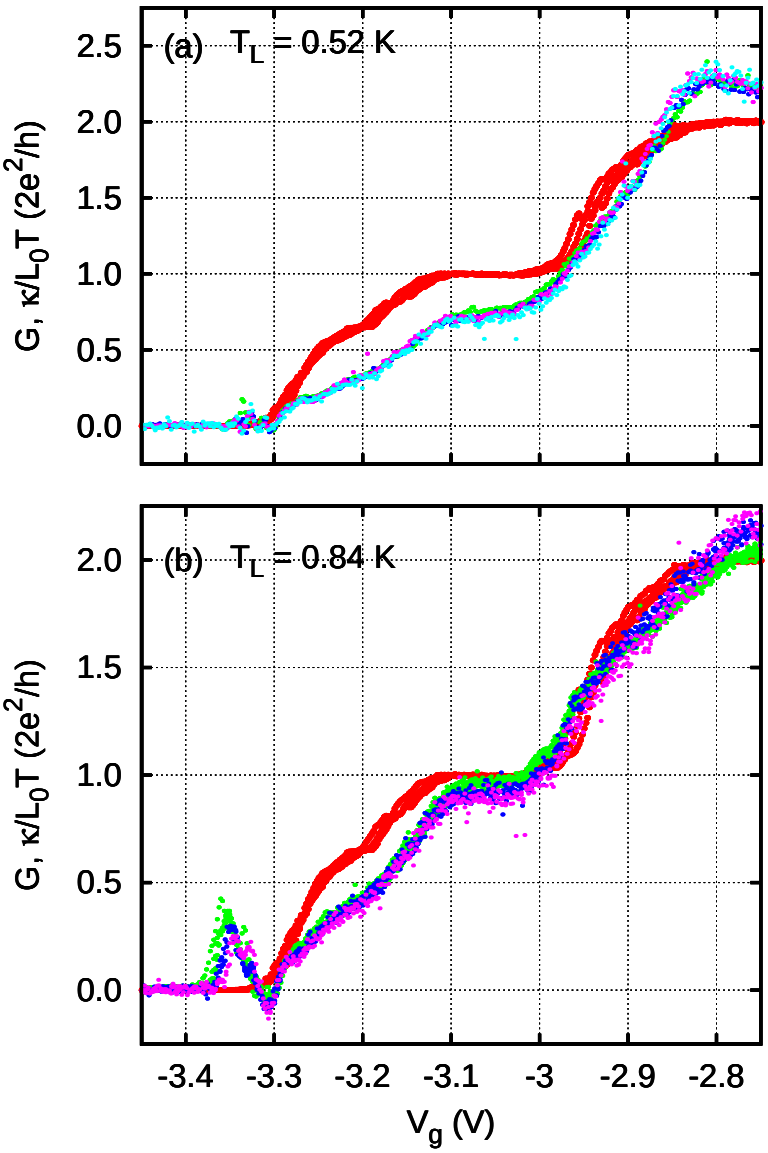

Figure 5.19: Free parameter fitting of thermal conductance curves for sample II:
(a) κ/L_0T at $T_L = 0.52$ K for $I_H = 2 - 5$ µA; $\gamma \approx 1.06 - 1.54$.
(b) κ/L_0T at $T_L = 0.84$ K for $I_H = 5 - 10$ µA; $\gamma \approx 1.06 - 1.19$.
The thick, red curve is $G(V_g)$, corrected for a series resistance.

5.3.3 Other features

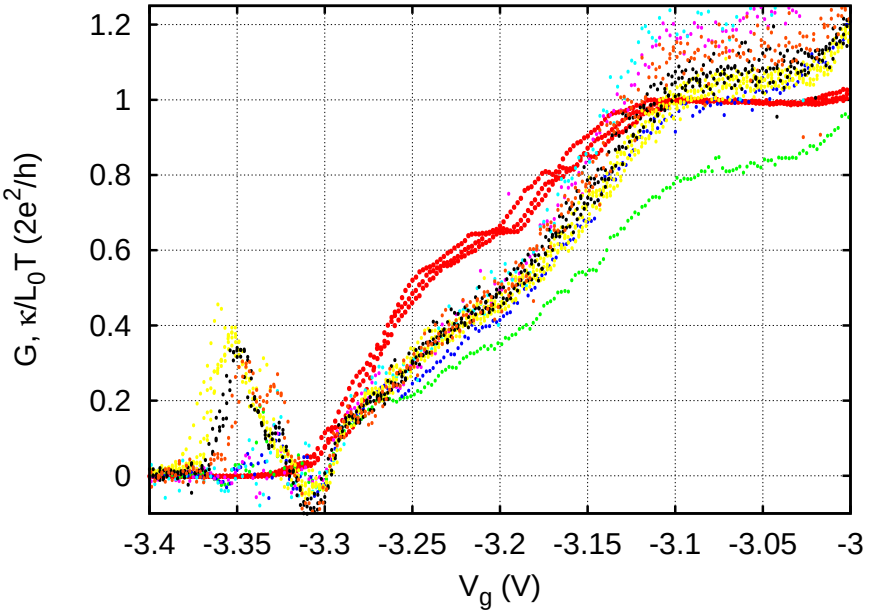

Figure 5.20: Comparison of the thermal κ/L_0T and electrical conductance G for sample II.
The thick, red curve is $G(V_g)$ measured at $T_L = 1.2$ K, corrected for a series resistance of 1800 Ω. The remaining curves are obtained from Eq. (5.7), using the data from Figs. 5.15*a*,*b*: $T_L = 0.52$ K with $I_H = 2 - 5$ µA, and $T_L = 0.84$ K with $I_H = 5 - 10$ µA.
At $V_g \approx -3.2$ V, the 0.7 structure in $G(V_g)$ is observed at $G \approx 0.65(2e^2/h)$. The corresponding feature in $\kappa(V_g)$ is observed at $\kappa/L_0T \approx (0.4 - 0.5)2e^2/h$.

Figure 5.20 shows the κ/L_0T curves for $T_L = 0.52$ K and $T_L = 0.84$ K. The traces are compared to $G(V_g)$, which was measured at $T_L = 1.2$ K and has been corrected for a series resistance of 900 Ω. The 0.7 structure appears in the $G(V_g)$ curve at $G \approx 0.65(2e^2/h)$; the corresponding feature in the κ/L_0T curves is observed between $0.4(2e^2/h)$ and $0.5(2e^2/h)$. This is consistent with the results for sample I, shown in Sec. 5.2.4.

Figure 5.21 shows the past-pinch-off feature for sample II. The two curves were taken at $T_L = 0.84$ K and $I_H = 10$ µA, and $T_L = 0.52$ K and $I_H = 5$ µA, respectively. Re(V_{th}) is the same for both curves, except where the peak after pinch-off appears.

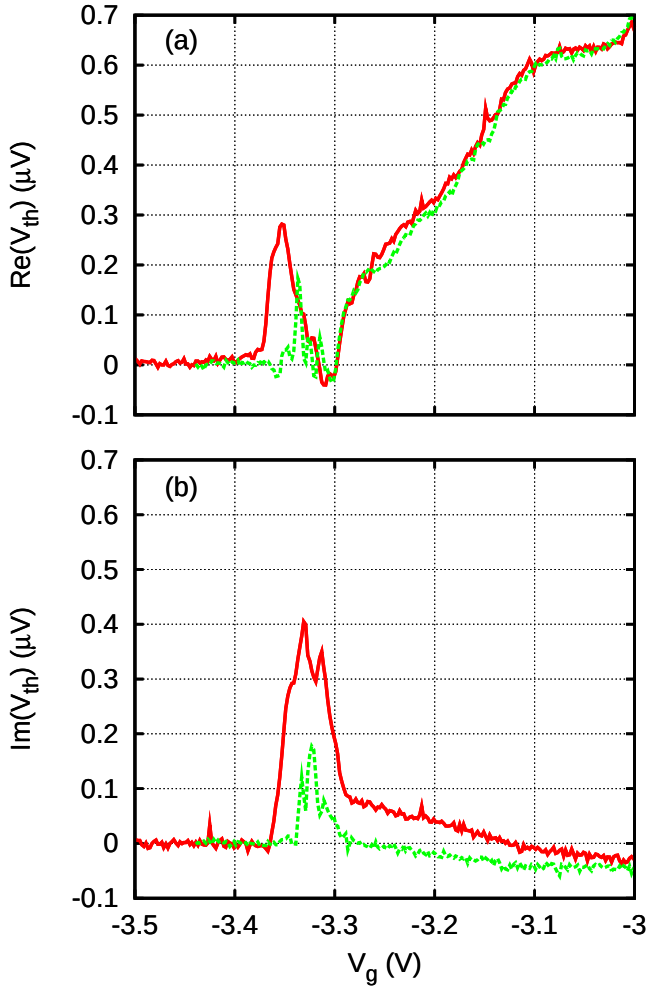

Figure 5.21: Thermal conductance measurements at $T_L = 0.84$ K and $I_H = 10$ µA (red) and at $T_L = 0.52$ K and $I_H = 5$ µA (green).
(a) The real part of the thermovoltage signal, Re(V_{th}).
(b) The imaginary part of the signal, Im(V_{th}).

5.4 Sample III

Sample III was fabricated trying to avoid the problems sample II had. The lithographic dimensions of the split-gates are the same as for sample I, but the gates are spread further apart from each other. Conductance measurements show that there is no cross-talk between split-gates, which allowed thermal conductance measurements over a much wider range of gate voltages. However, the area of the thermal box is greater than in the other samples, which leads to an increased effect of the electro-phonon interaction.

Again, the experimental $\kappa(V_g)$ curves do not match exactly the theory, and both impurity effects and RTS are observed. However, the discrepancy between experiment and theory is much smaller than in samples I and II. The experimental curves also display a reduction in κ corresponding to the 0.7 structure, like in the other two samples.

5.4.1 Results

Measurements were performed at constant lattice temperature in the range $T_L \approx 0.05 - 0.5$ K. Figure 5.22 shows the $V_{th}^{box}(V_g)$ curves taken at $T_L = 0.203$ K for heating currents $I_H = 0.88 - 10$ µA. The curves show plateaux at $V_g \approx -1.55, -1.3, -1.05,$ and-0.85 V, corresponding to the conductance plateaux shown in Fig. 5.23*a*.

The measured $V_{th}^{box}(V_g)$ curves span an order of magnitude in voltage ($V_{th}^{box} \approx 0.1 - 5$ µV), and to highlight similarities and differences between them, each curve has been normalized by the voltage on the first plateau (at $V_g \approx -1.55$ V). Figure 5.23*b* shows the traces of Fig. 5.22 after normalization. As expected, the curves overlap around the first plateau, but for $V_g \gtrsim -1.45$ V they spread out. The curves measured at higher heating current I_H are lower than those at lower I_H, which is consistent with an increased effect of the electron-phonon interaction.

Figure 5.23*c* shows normalized $V_{th}^{box}(V_g)$ curves taken at $T_L \approx 0.05,\ 0.2,$ and 0.5 K, and at $I_H = 2.5$ and 5.0 µA. The curves taken at higher I_H lie beneath the curves for lower I_H, and the curves taken at higher T_L lie below those at lower T_L. Both behaviours are consistent with the increased effect of the electron-phonon interaction.

For comparison to the thermal measurements, Fig. 5.23*a* shows the electrical conductance $G(V_g)$ of the main split-gate, measured at $T_L \approx 0.05$ K. The measured conductance is corrected for a series resistance of $R_s \approx 500\ \Omega$. The following

features can be identified in the thermal conductance traces:

- Plateaux $i = 1,\ 2,\ 3,\ 4,\ 5$ are at $V_g \approx -1.55,\ -1.3,\ -1.05,\ -0.85,\ -0.70$ V, respectively, coinciding with the plateaux in $G(V_g)$.
- The 0.7 structure occurs at $V_g \approx -1.66$ V.
- Additional features appear between plateaux, which have no corresponding feature in $G(V_g)$.
- There is a feature at $V_g \approx -1.72$ V, corresponding to a tail in the conductance right after pinch-off.
- The artefact beyond pinch-off at $V_g \approx -1.75$ V has no corresponding feature in the electrical conductance.

Figure 5.24 shows normalized $V_{th}^{box}(V_g)$ curves measured at three different lattice temperatures: $T_L \approx 0.05$ K, 0.2 K, and 0.5 K. The behaviour of the curves is consistent with that observed in Fig. 5.24*b* and *c*. The range of heating currents is approximately the same for all three measurements: $I_H \approx 1.5 - 10$ µA. With increasing lattice temperature the spread of the normalized curves becomes smaller, and at $T_L = 0.496$ K the normalized $V_{th}^{box}(V_g)$ overlap up to the fifth plateau.

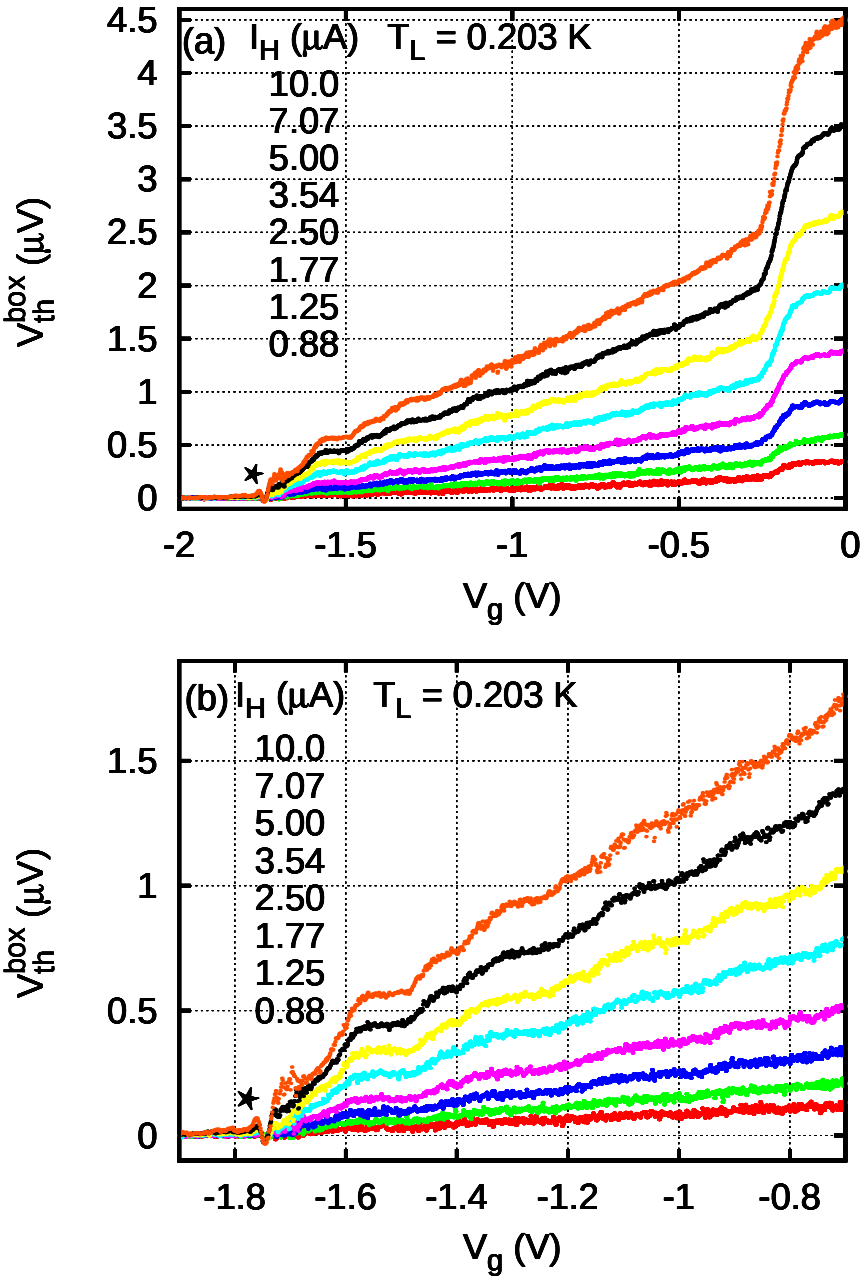

Figure 5.22: $V_{th}^{box}(V_g)$ characteristics of sample III at $T_L = 0.203$ K and $I_H = 10.0, 7.07, 5.00, 3.54, 2.50, 1.77, 1.25, 0.88$ μA (from top to bottom):
(a) Full curves, where we can see $V_{th}^{H} = V_{th}^{box}(V_g = 0)$.
(b) Close-up on the first five plateaux.
The feature marked with a star (*) is an artefact of the measurement, as discussed in Sec. 5.2.4.

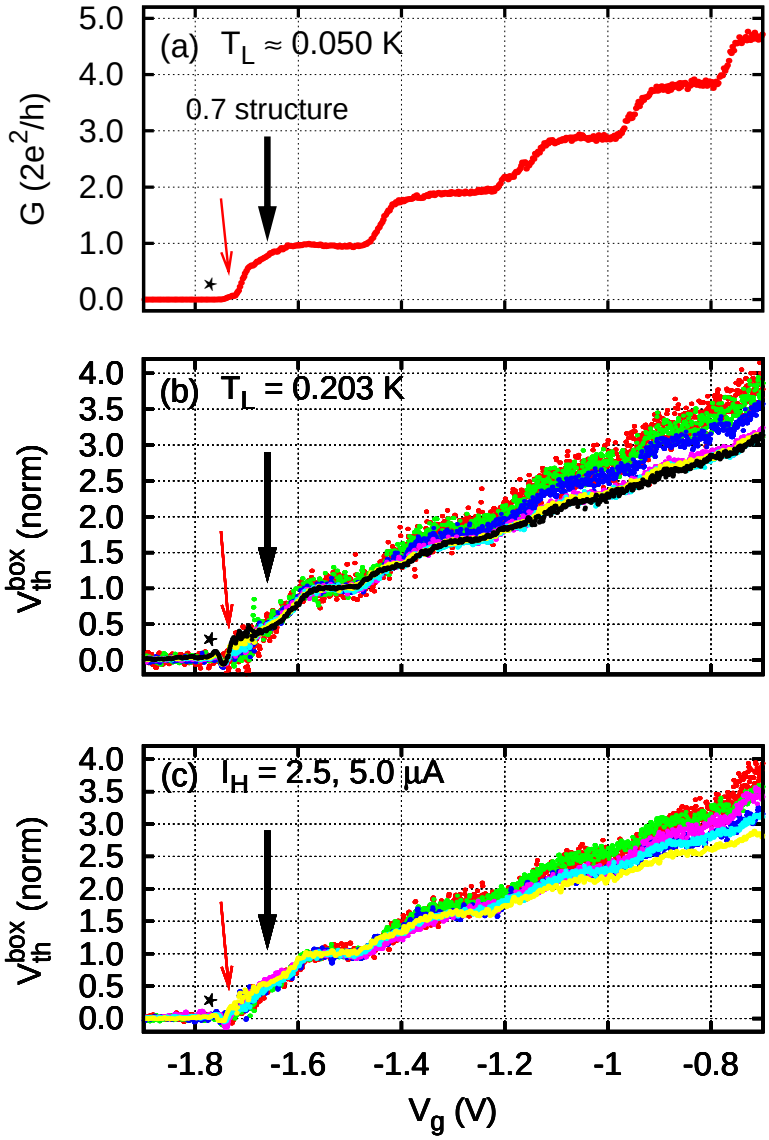

Figure 5.23: Comparison of thermal conductance measurements to $G(V_g)$ for sample III:
(a) $G(V_g)$ at $T_L \approx 0.05$ K, corrected for a series resistance of 500 Ω.
(b) Normalized $V_{th}^{box}(V_g)$ at $T_L = 0.203$ K for $I_H \approx 0.9 - 10$ µA.
(c) Normalized $V_{th}^{box}(V_g)$ measured for $I_H = 2.5$ and 10 µA at $T_L \approx 0.05,\ 0.2,\ 0.5$ K.
The black arrow at $V_g = -1.66$ V indicates the 0.7 structure, the red arrow indicates a tail in the electrical conductance after pinch-off, and the star indicates an artefact in the $V_{th}^{box}(V_g)$ curves, which is not present in $G(V_g)$.

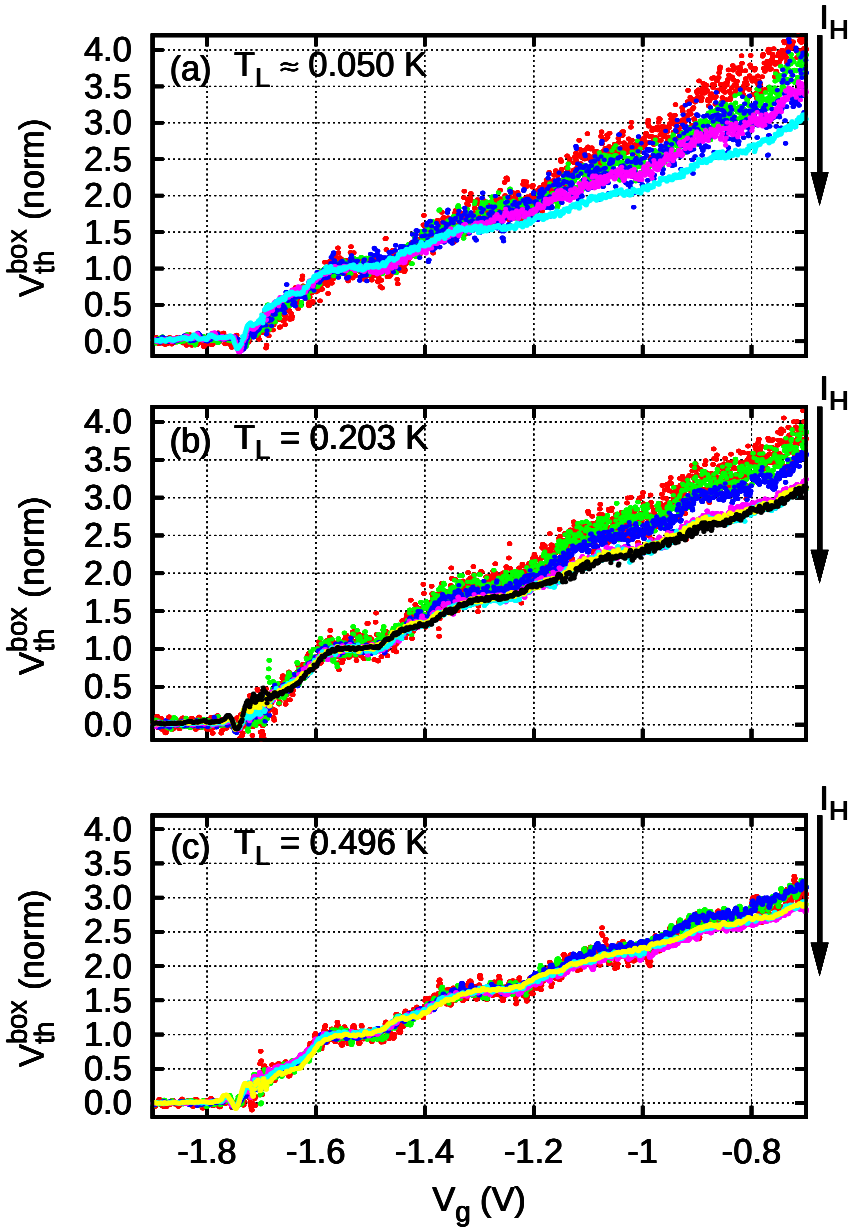

Figure 5.24: Normalized $V_{th}^{box}(V_g)$ characteristics of sample III:
(a) $T_L \approx 0.05$ K and $I_H = 7.07, 5.00, 3.54, 2.50, 1.77$ µA.
(b) $T_L = 0.203$ K and $I_H = 10.0, 7.07, 5.00, 3.54, 2.50, 1.77, 1.25$ µA.
(c) $T_L = 0.496$ K and $I_H = 10.0, 7.07, 5.00, 3.54, 2.50, 1.77$ µA.

5.4.2 Test of the Wiedemann-Franz law

Unlike samples I and II, sweeping the gate voltage on A in sample does not affect constrictions B and C. So it was possible to measure a full $V_{th}^{box}(V_g)$ curve from $V_g = 0$ to pinch-off, without adjusting the gate voltage applied to the thermometer split-gate. Hence both $V_{th}^{box}(V_g)$ and $V_{th}^{H} = V_{th}^{box}(V_g = 0)$ are measured under the same conditions, and the Wiedemann-Franz law can be tested over a larger number of plateaux.

Figure 5.25 shows the results of applying Eq. 5.7 to the measurements taken at $T_L \approx 0.05,\ 0.2,$ and 0.5 K:

$$G_A = (G_B + G_C)\frac{V_{th}^{box}}{V_{th}^{H} - V_{th}^{box}} + \frac{2\dot{Q}_{el-ph}(T_{box}, T_L)}{L_0(T_H^2 - T_{box}^2)}. \tag{5.7}$$

In all three cases the experimental κ/L_0T curves lie beneath the expected curve, $G(V_g)$. The discrepancy decreases as the heating current increases:

(a) at $T_L \approx 0.05$ K, the discrepancy goes from ∼50% for $I_H = 1.77$ µA down to ∼30% for $I_H = 7.07$ µA;

(b) at $T_L = 0.203$ K, the discrepancy goes from ∼40% for $I_H = 1.25$ µA down to ∼23% for $I_H = 10.0$ µA;

(c) at $T_L = 0.496$ K, the discrepancy goes from ∼30% for $I_H = 1.77$ µA down to ∼5% for $I_H = 10.0$ µA.

As has been done for samples I and II, we can modify Eq. (5.7) as follows:

$$G_A = (G_B + G_C)\frac{V_{th}^{box}}{\gamma V_{th}^{H} - V_{th}^{box}} + \frac{2\dot{Q}_{el-ph}(T_{box}, T_L)}{L_0(T'^2_H - T_{box}^2)}, \tag{5.11}$$

where γ is a free parameter and T'^2_H is obtained using γV_{th}^{H} in Eq. (5.3). Adjusting γ to fit the experimental curves to the theory yields the results shown in Fig. 5.26:

(a) at $T_L \approx 0.05$ K, $\gamma = 0.72 - 0.80$;

(b) at $T_L = 0.203$ K, $\gamma = 0.72 - 0.82$;

(c) at $T_L = 0.496$ K, $\gamma = 0.80 - 0.95$.

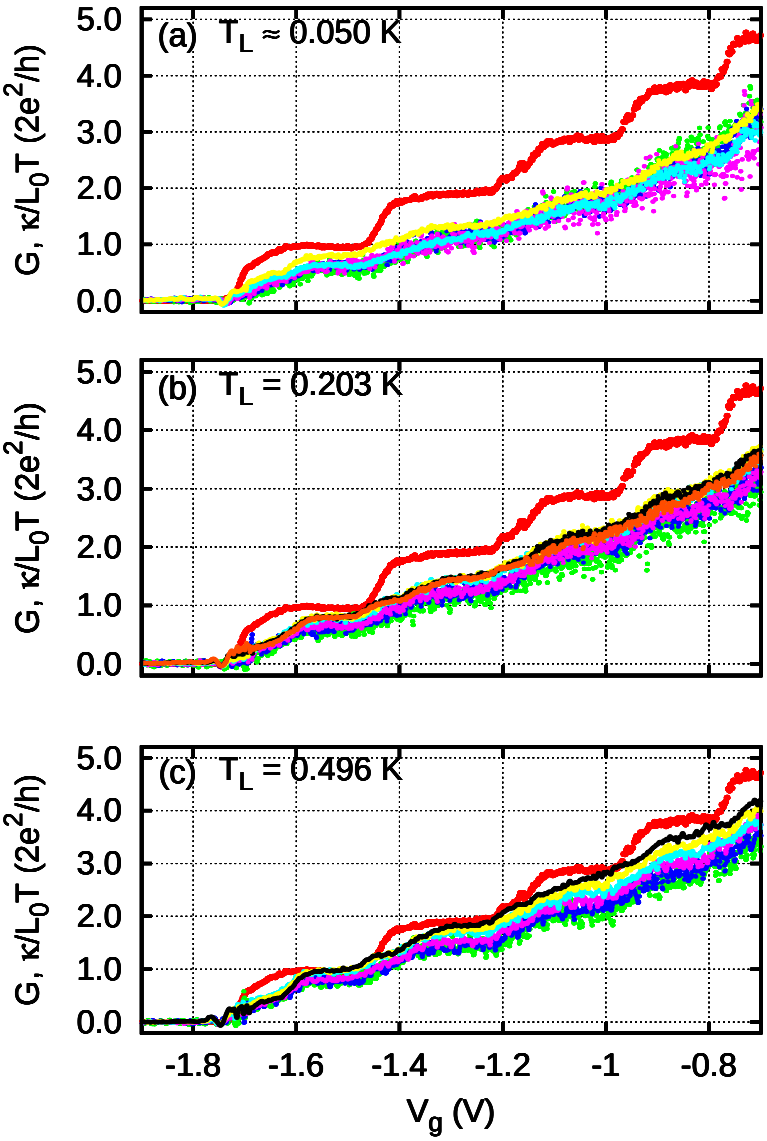

Figure 5.25: Test of the Wiedemann-Franz law for sample III. Eq. (5.7) has been applied to the data from Fig. 5.16:
(a) (κ/L_0T) at $T_L \approx 0.05$ K for $I_H \approx 1.7 - 7.1$ µA.
(b) (κ/L_0T) at $T_L = 0.203$ K for $I_H \approx 1.2 - 10$ µA.
(c) (κ/L_0T) at $T_L = 0.496$ K for $I_H \approx 1.7 - 10$ µA.
The thick, red curve is $G(V_g)$, corrected for a series resistance of 500 Ω. The feature corresponding to the 0.7 structure is at $V_g \approx -1.66$ V.

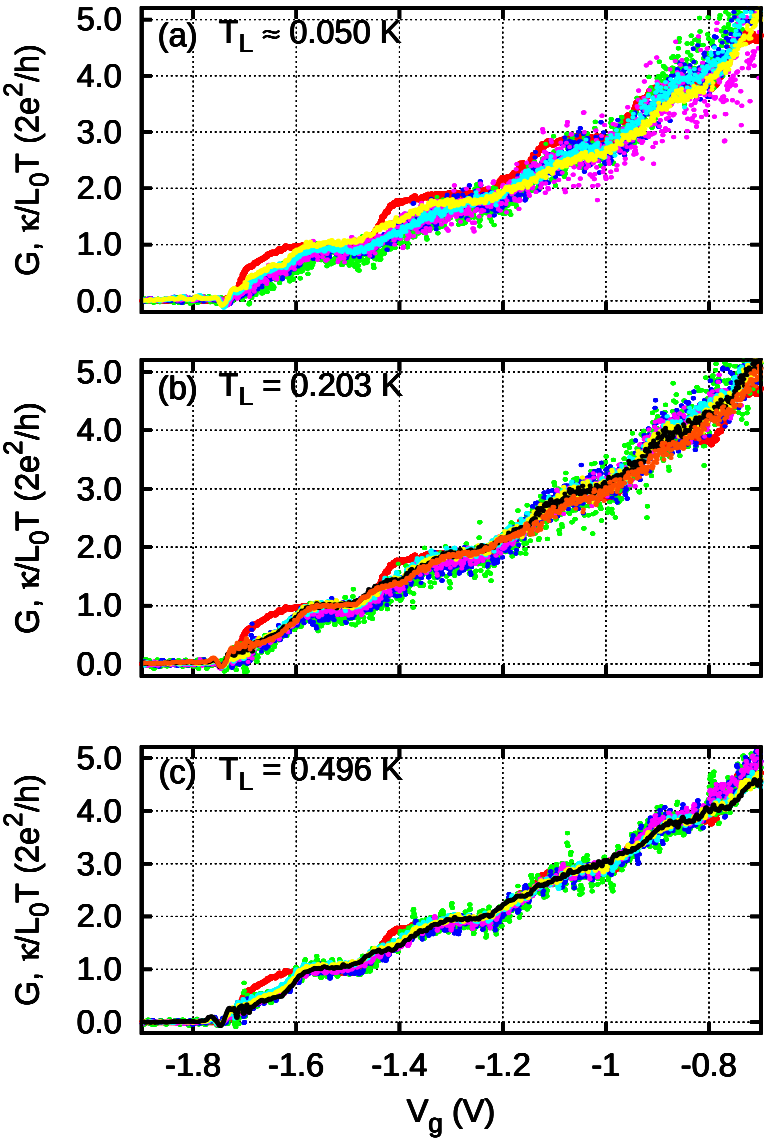

Figure 5.26: Free parameter fitting of $(\kappa/L_0T)(V_g)$ curves for sample III:
(a) κ/L_0T at $T_L \approx 0.05$ K for $I_H \approx 1.7 - 7.1$ µA; $\gamma \approx 0.72 - 0.80$.
(b) κ/L_0T at $T_L = 0.203$ K for $I_H \approx 1.2 - 10$ µA; $\gamma \approx 0.72 - 0.82$.
(c) κ/L_0T at $T_L = 0.496$ K for $I_H \approx 1.7 - 10$ µA; $\gamma \approx 0.80 - 0.95$.
The thick, red curve is $G(V_g)$, corrected for a series resistance of 500 Ω.

0.7 structure

Figure 5.27 shows a selection of $(\kappa/L_0T)(V_g)$ curves from the whole range of measurements. At $V_g \approx -1.66$ V the 0.7 structure is observed in $G(V_g)$ as a shoulder at $G \approx 0.8(2e^2/h)$. The corresponding feature in the thermal conductance is between $0.4(2e^2/h)$ and $0.5(2e^2/h)$.

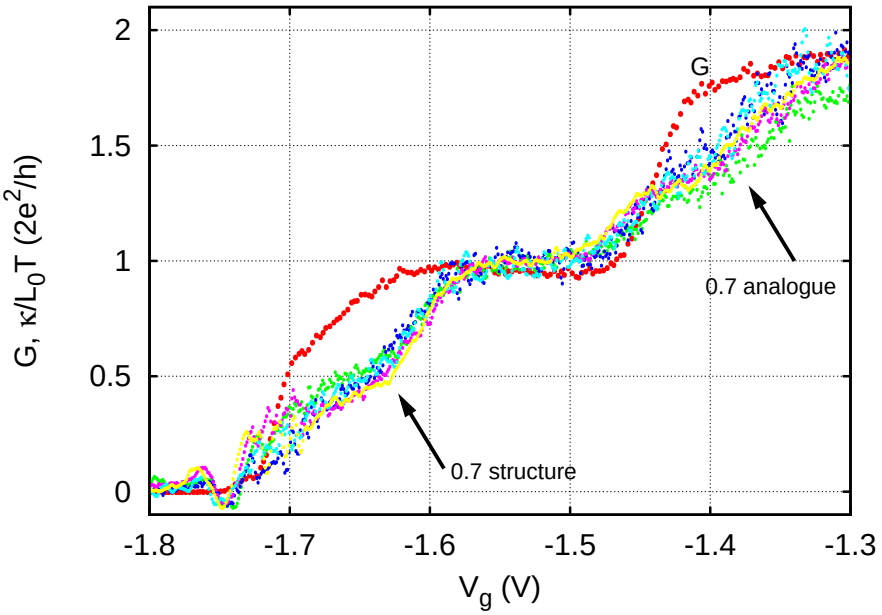

Figure 5.27: Comparison of the thermal measurement $(\kappa/L_0T)(V_g)$ and the electrical conductance $G(V_g)$ for sample III.
The thick, red curve is $G(V_g)$ measured at $T_L \approx 0.05$ K and corrected for a series resistance. The κ/L_0T curves are a selection over the whole range of measurements, and features analogous to the 0.7 structures are observed between the first and second plateau.

At $V_g \approx -1.4$, $\kappa(V_g)$ shows a feature analogous to the 0.7 structure at $\kappa/L_0T \approx 1.4(2e^2/h)$ (halfway between the first and the second plateau). There is no corresponding feature in $G(V_g)$. This *0.7 analogue* is similar to the features described in Ref. [7].

5.5 Conclusions

In this chapter thermal conductance measurements in three samples have been presented and discussed. In the following we will summarize the results and conclusions. Our attention will be focused mainly on the thermal conductance feature related to the 0.7 structure.

5.5.1 Summary of the measurements

The thermal conductance κ of a split-gate device has been measured as function of gate voltage V_g for temperatures between 0.05 K and 1.2 K. Previous measurements [4] showed that $\kappa(V_g)$ displays rough structures corresponding to the usual plateaux at $N(2e^2/h)$ in the electrical conductance $G(V_g)$.

The design of the samples used in this work follows the proposal in Ref. [10], and is presented schematically in Fig. 5.1 on page 83. The electrons on one side of the constriction were heated with a current, and the temperature drop across the constriction was measured using the thermopower of another constriction. A third split-gate completes the definition of a region of uniform electron temperature between the main constriction and the thermometer constriction, and provides a reference for the thermovoltage measurement.

The measurements confirm the advantages of the new design over earlier designs [4], as can be seen from Fig. 5.14 on page 102. The measured thermovoltage is larger and a wider range of temperatures in the linear regime is accessible. The higher accuracy of the measurements allows for quantitative tests of the theory, and in particular of the Wiedemann-Franz law.

5.5.2 Quantization of the thermal conductance and Wiedemann-Franz law

Comparing the thermovoltage measurements to the conductance curves $G(V_g)$ shows that in all three samples the thermal conductance $\kappa(V_g)$ displays plateaux corresponding to the plateaux in $G(V_g)$. If the Wiedemann-Franz law, $\kappa = L_0TG$, is satisfied, all the $\kappa(V_g)$ curves of a sample are expected to collapse onto one curve when divided by L_0T, and the resulting curve is expected to follow the $G(V_g)$ of the sample.

As can be seen from Fig. 5.8 on page 94, Fig. 5.18 on page 107, and Fig. 5.25 on page 118, most of the $\kappa(V_g)$ curves do not follow this expected behaviour. Each

sample seems to have peculiar type of discrepancy between theoretical and experimental curves. Several scenarios for these discrepancies have been considered: a breakdown of the Wiedemann-Franz law, an electron-phonon interaction stronger than expected, and a lower than expected electron heating by the heating current. The experimental curves have been fitted to the theoretical curves with each of these scenarios, but no single conclusion about a mechanism could be reached.

The fact that the discrepancies between measured and theoretical curves show no consistent pattern between different samples, suggests that they are not an intrinsic property of a 1D constriction. Heat flows and electron temperatures can be affected by the specific properties of the sample and are not determined solely by the constrictions, so we can assume that the absolute value of the $\kappa(V_g)$ curves obtained from the measurements deviates from the theoretical value. We can interpret this deviation from theory as a calibration problem: the electron temperatures measured are not the ones directly related to the thermal conductance. We believe that a 1D constriction will follow the Wiedemann-Franz law, and that it can be observed for a sample where there is no such calibration problem.

Under this assumption, we can compare the shape of the $\kappa(V_g)$ curves for different temperatures and for different samples, and compare them to the corresponding $G(V_g)$. This is done by dividing the curves by their value on the first plateau.[3] The result of this "normalization" fits with the expected behaviour [11]: $\kappa(V_g)$ follows $G(V_g)$ on the plateaux, and between the plateaux it is flatter. The exception is the feature corresponding to the 0.7 structure.

5.5.3 0.7 structure

Under the assumption that the first plateau follows the Wiedemann-Franz law, $\kappa = (2e^2/h)L_0T$, in all samples the thermal conductance feature corresponding to the 0.7 structure shows the following:

$$0.85\frac{e^2}{h}L_0\ T \lesssim \kappa \lesssim \frac{e^2}{h}L_0\ T. \tag{5.12}$$

The electrical conductance of the 0.7 structure is never observed below $0.63(2e^2/h)$, and grows stronger with increasing temperature. In contrast, κ becomes thermally smeared with increasing temperature, but it never develops a plateau like G.

Figure 5.28 shows the theoretical $\kappa(V_g)$, calculated using $G(V_g)$ as transmission probability $t(E)$, and the experimental curves for sample I. The $G(V_g)$ was

[3]Effectively, we are "re-calibrating" $T(V_g)$ in the $(\kappa/L_0T)(V_g) = \kappa(V_g)/L_0T(V_g)$ curves.

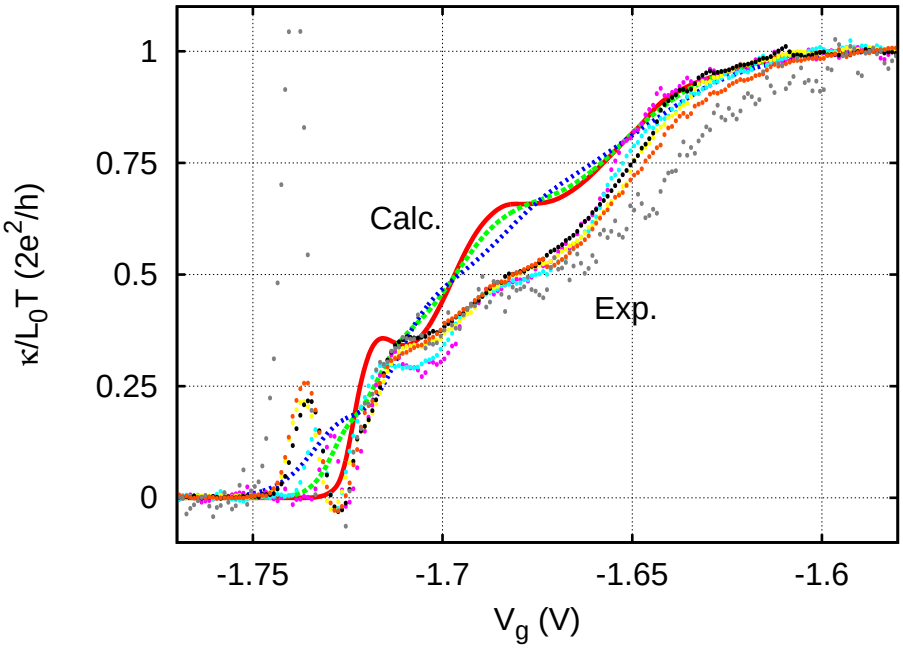

Figure 5.28: Calculated and experimental $(\kappa/L_0T)(V_g)$ curves for sample I. The theoretical curves are calculated from the transmission probability $t(E)$, which is obtained from $G(V_g)$ measured at $T_L \approx 1.2$ K, which has a well defined plateaux at $G \approx 0.63(2e^2/h)$. The temperatures for the calculations were $T = 0.05\text{ K}, 0.25\text{ K}, 0.50\text{ K}$. The experimental curves are a selection over the range $T \approx 0.3 - 1$ K.

measured at $T \approx 1.2$ K and has a plateaux at $G \approx 0.63(2e^2/h)$. Theoretically the 0.7 structure in $G(V_g)$ gives a feature at $\kappa/L_0T \approx 1.3(e^2/h)$, but the experimental curves exhibit the corresponding feature at $\kappa/L_0T \approx e^2/h$. This difference shows that the 0.7 structure does not follow the single-particle picture, on which the calculations are based.

Figure 5.29 shows $(\kappa/L_0T)(V_g)$ curves for sample I and sample III. Both samples again show the structure at $\kappa/L_0T \approx e^2/h$ (marked with A and B), as does sample II (which can be seen in Fig. 5.20 on page 110). Since all three samples show the same result, we believe that, like the 0.7 structure in $G(V_g)$, this feature is an intrinsic property of a 1D constriction. Furthermore, both samples I and III show an analogue feature at $2.7(e^2/h) \lesssim \kappa/L_0T \lesssim 3(e^2/h)$, which has no corresponding feature in $G(V_g)$. In sample I (marked with D) the feature is visible for $T > 0.7$ K, but for sample III (marked with C) it is observed at all

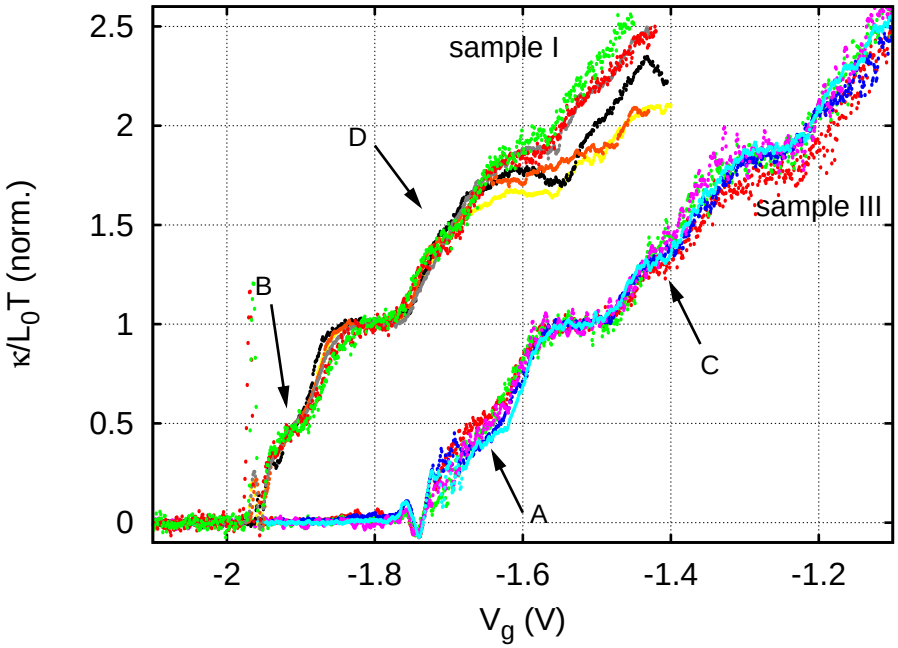

Figure 5.29: $(\kappa/L_0T)(V_g)$ curves for samples I and III. All curves have been normalized at the first plateau, and cover the whole temperature range examined. The curves for sample I are offset horizontally by ∼200 mV for clarity.
The features indicated by A and B correspond to the 0.7 structure. C marks the 0.7 analogue in sample III, which is observed at all temperatures. D marks a similar feature in sample I, which is observed only for $T_L > 0.7$ K.

temperatures.

According to Van Houten *et al.* [11], if the transmission probability $t(E)$ changes abruptly from one 1D to the next, the thermal conductance displays quasi-plateaux at odd multiples of $L_0T(e^2/h)$. Figure 5.30 shows theoretical $(\kappa/L_0T)(V_g)$ curves, calculated using the saddle-point potential with $\omega_y/\omega_x = 5$. As the temperature increases, features at $\kappa/L_0T \gtrsim (2N+1)e^2/h$ develop between the regular plateaux. In contrast, the experimental curve shows features at $\kappa/L_0T \lesssim (2N+1)e^2/h$ even at the lowest temperatures. Again, the experimental features cannot be explained within a single-particle picture.

Summarizing some of the experimental results on the 0.7 structure obtained

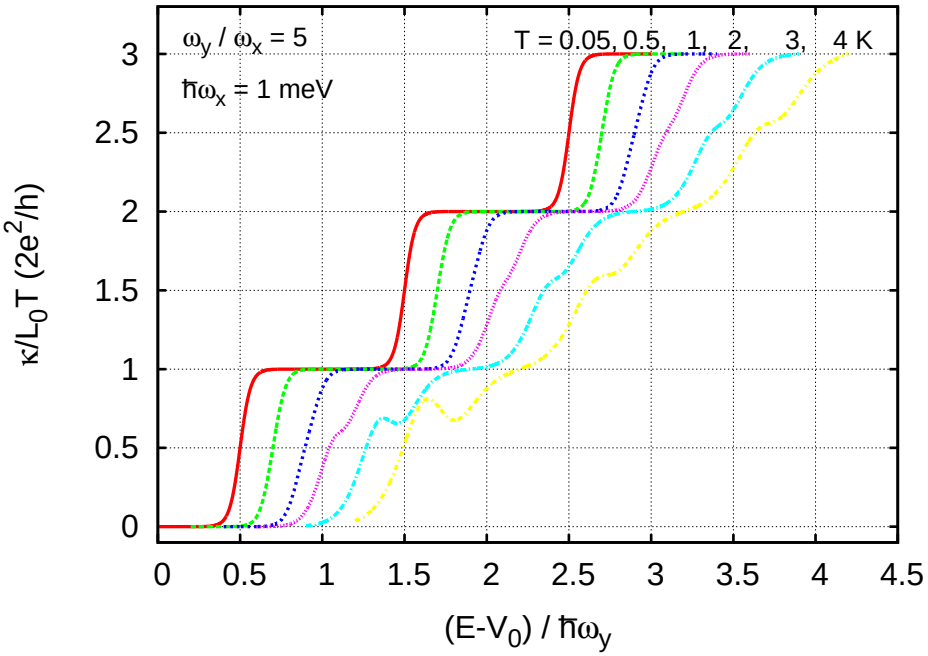

Figure 5.30: Theoretical $(\kappa/L_0T)(V_g)$ curves, calculated using the saddle-point potential model. The parameters are $\hbar\omega_x = 1$ meV and $\hbar\omega_x = 5$ meV. The traces are off-set horizontally for clarity. For $T > 1$ K, κ shows structures at $\kappa/L_0T \gtrsim (2N+1)e^2/h$, in addition to the regular plateaux.

here and elsewhere:

$$\begin{array}{rcll} \text{electrical conductance} & G & \approx & 0.63\dfrac{2e^2}{h} - 0.85\dfrac{2e^2}{h} \\ \text{thermal conductance} & \kappa & \approx & \dfrac{e^2}{h}L_0T \\ \text{thermopower} & S & > & 0 \end{array} \tag{5.13}$$

In the following sections we will present and discuss possible interpretations for the observed features.

Two channels

From the outset [6] until the latest works [12], the 0.7 structure has often been interpreted as the result of two channels, with different transmission probabilities. Wang and Berggren [13] found in their calculations that the potential barrier in the constriction is different for spin up and spin down: spin-up electrons are fully

transmitted, but spin-down electrons tunnel through the barrier. We can assume the same and write the contribution of each channel as follows:

	Spin-up	Spin-down
G	e^2/h	$0 - e^2/h$
κ	$L_0\ T\ (e^2/h)$	~ 0
S	0	> 0

There are several problems with this interpretation. If the conductance for the spin-down channel was due to tunneling, we would expect an increase in G with increasing temperature, contrary to what is observed. The temperature dependence is consistent with a scattering mechanism, which saturates at high temperatures. However, neither tunneling nor scattering can explain why the thermal conductance of the spin-down channel is nearly zero and has no temperature dependence. Tunneling or scattering in the spin-down channel yield an energy-dependent transmission probability, and, according to the Cutler-Mott relation, a non-zero thermopower.

Cronenwett *et al.* [14] interpreted the 0.7 structure as a Kondo-like effect, based on similarities with the Kondo effect in quantum dots (QDs). The 0.7 structure is the result of a fully transmitting channel and a Kondo-like channel:

	Normal	Kondo-like
G	e^2/h	$(e^2/h)\ f(T/T_K)$
κ	$L_0\ T\ (e^2/h)$	$\leq L_0\ T\ (e^2/h)$
S	0	$\neq 0$ and changes sign

where $f(T/T_K)$ is the universal function for Kondo conductance, and T_K is the Kondo temperature. G seems to fit reasonably well with the measurements, including the zero-bias anomaly. However, the thermal conductance of a QD in the Kondo regime is predicted [15] to increase from zero to $L_0\ T\ (e^2/h)$ with decreasing temperature, contrary to what is observed for the 1D constriction. Furthermore, the thermopower of a QD changes sign with increasing temperature [15], which is also not observed in 1D constrictions.

Luttinger liquid

The 0.7 structure has also been interpreted as a manifestation of Luttinger liquid (LL) behaviour. Maslov and Stone [16] have shown that two-terminal conductance of a LL connected to Fermi liquid reservoirs should be quantized at e^2/h per spin orientation (the interaction between electrons in the 1D conductor does not change

G). This does not agree with the measured conductance of the 0.7 structure, which is always $0.63(2e^2/h) \lesssim G < 2e^2/h$.

Kane and Fisher [17] showed that the interaction in a Luttinger liquid modifies the Wiedemann-Franz law: $\frac{\kappa}{TG} = L = \frac{L_0}{g} \neq L_0$, where g is the parameter characterizing the LL. For repulsive interactions between electrons we have $g < 1$, and thus $L > L_0$, contrary to the measured $L < L_0$. So, neither G nor κ of the 0.7 structure show the behaviour expected from a Luttinger liquid.

Wigner crystal

Matveev [18, 19] proposed a model for the 0.7 structure, where the quantum wire at low densities is a Wigner crystal. In this model the charge and spin degrees of freedom are separated. If the quantum wire is connected to reservoirs, the conductance has two contributions:

$$G = \frac{1}{R_c + R_s},$$

where $R_c = h/2e^2$ is the charge contribution, and $R_s = 0 - h/2e^2$ is the spin contribution. In the limit of high temperatures, R_s saturates at $h/2e^2$, and we obtain $G = e^2/h$. The measurements give $G > 0.63(2e^2/h)$ for the highest temperatures where it is observed, so this model does not match the experimental results.

Alternative

Here we will present an interpretation based on the "two channels" approach. In Section 5.2.2 we showed a comparison between experiment and theory, where the theoretical curves are obtained from calculations of the type presented in Ref. [11]. It is assumed that the transmission probability can be obtained from the low-temperature conductance:

$$t(E) = \lim_{T \to 0} G(V_g).$$

Although this assumption is correct only within a single-particle picture, it is a legitimate starting point to understand transport.

Based on Fig. 5.29, we see that κ/L_0T has plateaux at multiples of $2e^2/h$ and weaker features at odd multiples of e^2/h. Assuming that $\kappa(V_g)$ gives a more faithful picture of $t(E)$ than $G(V_g)$, we could say that $t(E)$ has well-defined plateaux at $2N(e^2/h)$ and less well-defined ones at $(2N+1)(e^2/h)$. This situation reminds

one of the Zeeman-split subbands in a low magnetic field, so we can attribute the structure of $t(E)$ to a spontaneous spin polarization in the 1D constriction. The problem is why $G(V_g)$ does not show plateaux at $(2N+1)(e^2/h)$? It might be that the conductance is enhanced when there is one spin polarized subband, with a mechanism similar to the Kondo effect.

In conclusion, all the interpretations presented do not cover one or more aspects of the experimental properties of the 0.7 structure. In particular the suppression of the thermal conductance with respect to the electrical conductance cannot be explained by the existing theories. However, the most promising seems to be the interpretation of two channels.

5.5.4 Suggestions for future work

Measurements presented here strongly suggest that the Wiedemann-Franz law is satisfied by a 1D constriction. The necessary next step is to perform the same measurements in samples not affected by impurities or RTS.

An important step is repeating the measurements in a parallel magnetic field. This is especially important for the 0.7 structure, which is known to evolve into the Zeeman-split e^2/h plateau in $G(V_g)$; observing the evolution of the corresponding feature in $\kappa(V_g)$ can give new information. We expect that κ/L_0T will stay at $\sim e^2/h$, and develop into a plateau in a strong magnetic field, according to the single-particle picture.

In order to determine whether the $\kappa(V_g)$ curves presented show intrinsic properties of 1D constriction, measurements in different types of constriction are suggest. Examples are constrictions formed by split-gates in deeper 2DEGs, and constrictions fabricated by shallow-etching. In particular the etched constrictions should be interesting, because these have typically larger subband spacing. Therefore a wider temperature range is available, and it should be possible to observe whether the features at $\kappa/L_0T \approx e^2/h,\ 3e^2/h$ scale with temperature as the 0.7 structure does.

Bibliography

[1] N. J. Appleyard, J. T. Nicholls, M. Y. Simmons, W. R. Tribe, and M. Pepper, *Phys. Rev. Lett.* **81**, 3491 (1998).

[2] P. J. Price, *J. Appl. Phys.* **53**, 6863 (1982).

[3] C. Jasiukiewicz and V. Karpus, *Semicond. Sci. Technol.* **11**, 1777 (1996).

[4] L. W. Molenkamp, T. Gravier, H. van Houten, O. J. A. Buijk, M. A. A. Mabesoone, and C. T. Foxon, *Phys. Rev. Lett.* **68**, 3765 (1992).

[5] U. Sivan and Y. Imry, *Phys. Rev. B* **33**, 551 (1986).

[6] K. J. Thomas, J. T. Nicholls, M. Y. Simmons, M. Pepper, D. R. Mace, and D. A. Ritchie, *Phys. Rev. Lett.* **77**, 135 (1996).

[7] K. J. Thomas, J. T. Nicholls, N. J. Appleyard, M. Y. Simmons, M. Pepper, D. R. Mace, and D. A. Ritchie, *Phys. Rev. B* **58**, 4846 (1998).

[8] A. Kristensen, P. E. Lindelof, J. Bo Jensen, M. Zaffalon, J. Hollingbery, S. W. Pedersen, J. Nygard, H. Bruus, S. M. Reimann, C. B. Sørensen, M. Michel, and A. Forchel, *Physica B* **251**, 180 (1998).

[9] D. H. Cobden, N. K. Patel, M. Pepper, D. A. Ritchie, J. E. F. Frost, and G. A. C. Jones, *Phys. Rev. B* **44**, 1938 (1991).

[10] N. J. Appleyard, J. T. Nicholls, W. R. Tribe, M. Y. Simmons, and M. Pepper, *Physica E* **6**, 534 (2000).

[11] H. van Houten, L. W. Molenkamp, C. W. J. Beenakker, and C. T. Foxon, *Semicond. Sci. Technol.* **7**, B215 (1992).

[12] P. Roche, J. Ségala, D. C. Glattli, J. T. Nicholls, M. Pepper, A. C. Graham, K. J. Thomas, M. Y. Simmons, and D. A. Ritchie, *Phys. Rev. Lett.* **93**, 116602 (2004).

[13] C.-K. Wang and K.-F. Berggren, *Phys. Rev. B* **54**, 14257 (1996).

[14] S. M. Cronenwett, H. J. Lynch, D. Goldhaber-Gordon, L. P. Kouwenhoven, C. M. Marcus, K. Hirose, N. S. Wingreen, and V. Umansky, *Phys. Rev. Lett.* **88**, 226805 (2002).

[15] D. Boese and R. Fazio, *Europhys. Lett.* **56**, 576 (2001).

[16] D. L. Maslov and M. Stone, *Phys. Rev. B* **52**, R5539 (1995).

[17] C. L. Kane and M. P. A. Fisher, *Phys. Rev. Lett.* **76**, 3192 (1996).

[18] K. A. Matveev, *Phys. Rev. Lett.* **92**, 106801 (2004).

[19] K. A. Matveev, *Phys. Rev. B* **70**, 245319 (2004).

Appendix A

Sample characterization

We will present here the result of the characterization measurements of the samples. The setups are explained in Chapter 4, and the results are summarized in the form of graphics.

For all samples we present the conductance characteristics $G(V_g)$ of the three split-gate devices. From the $G(V_g)$ characteristic of the thermometer constriction, we obtain the ratio ω_y/ω_x for the saddle-point potential [1, 2].

Where a magnetic field perpendicular to the 2DEG was available, we performed *Shubnikov-de Haas* measurements [3] in the heating channel to characterize the 2DEG. At low magnetic fields, the magnetoresistance of a 2DEG is periodic as a function of B^{-1}, and from the periodicity $\Delta(B^{-1})$ we obtain the electron density:

$$n = \frac{2e}{h\Delta(B^{-1})}.$$

From the resistivity at zero magnetic field $\rho(B = 0)$ we obtain the mobility:

$$\mu = \frac{1}{en\rho(B = 0)},$$

where $\rho = f \cdot R(B = 0)$, and $f = W/L = 1/8$ is the geometrical factor of the heating channel.

Source-drain bias measurements [4–7] allow to measure the subband spacing in a 1D constriction and determine the parameter ω_y of the saddle-point potential. From ω_y/ω_x we obtain the ω_x, which enters the calibration of the thermometer constriction, as shown in Section 3.2.2.

A.1 Sample I

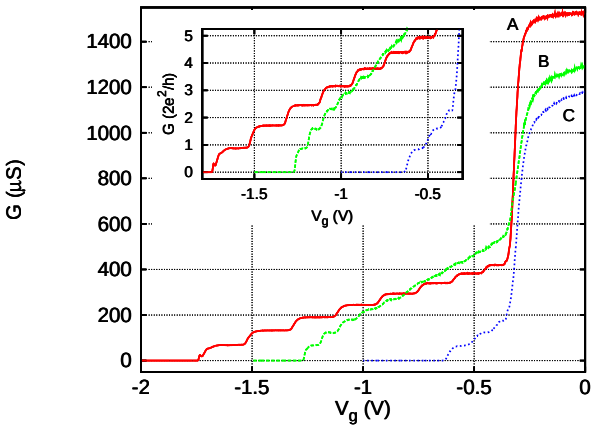

Figure A.1: Conductance characteristics for sample I at $T \approx 0.3$ K. The inset shows a close-up of the characteristics near pinch-off. We obtain $\omega_y/\omega_x = (2.1 \pm 0.2)$ for B.

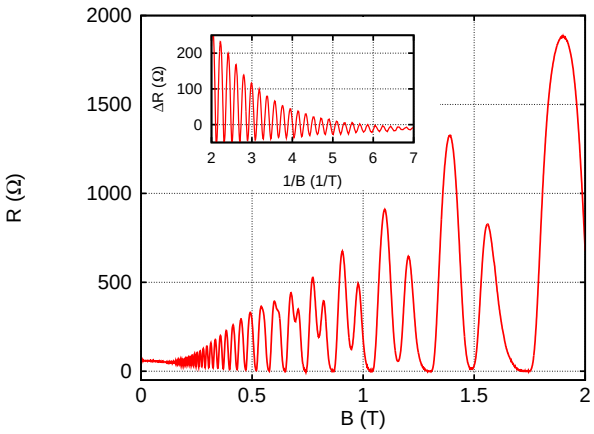

Figure A.2: Shubnikov-de Haas measurements for sample I at $T \approx 0.3$ K. The inset shows $\Delta R = R(B) - R(0)$ as a function of B^{-1}. We obtain $R(0) = (61 \pm 1)\ \Omega$ and $\Delta(B^{-1}) = (0.19 \pm 0.02)\ \mathrm{T}^{-1}$.

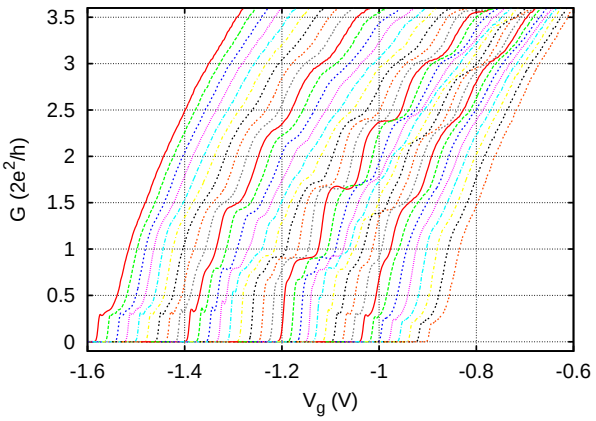

Figure A.3: Source-drain bias measurements for sample I at $T \approx 0.3$ K. The traces are off-set horizontally for clarity. The source-drain voltage V_{sd} is -3.4 mV for the left-most trace, and increases by 0.2 mV going to the right ($V_{sd} = +3.4$ mV for the right-most trace). The subband spacing is $\hbar\omega_y = (1.7 \pm 0.1)$ meV, which gives $\hbar\omega_x = (0.8 \pm 0.1)$ meV.

A.2 Sample II

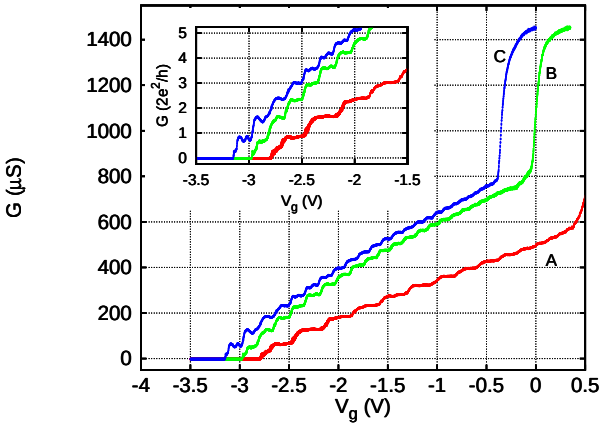

Figure A.4: Conductance characteristics for sample II at $T \approx 0.3$ K. The traces of A and B are off-set horizontally for clarity. The inset shows a close-up of the characteristics near pinch-off.

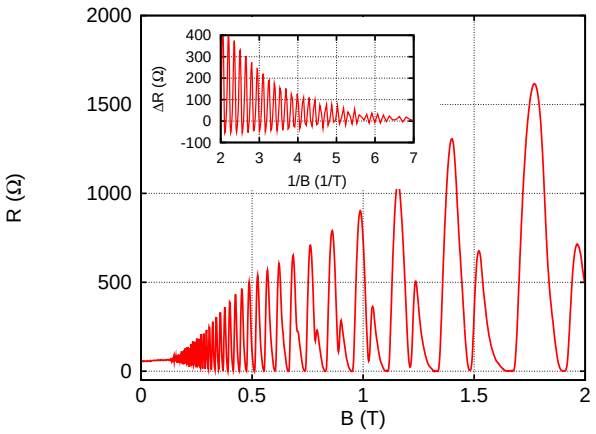

Figure A.5: Shubnikov-de Haas measurements for sample II at $T \approx 0.3$ K. The inset shows $\Delta R = R(B) - R(0)$ as a function of B^{-1}. We obtain $R(0) = (57 \pm 1)\ \Omega$ and $\Delta(B^{-1}) = (0.15 \pm 0.02)\ \mathrm{T}^{-1}$.

A.3 Sample III

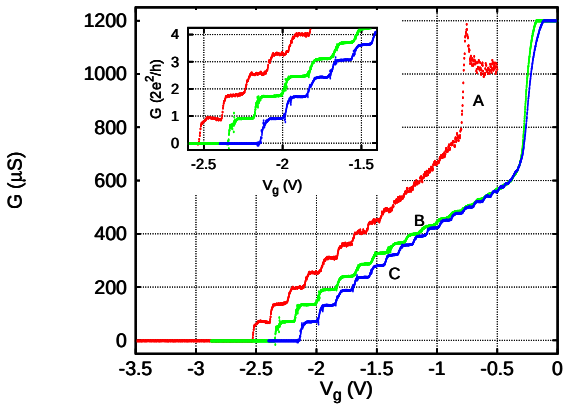

Figure A.6: Conductance characteristics for sample III at $T \approx 0.05$ K. The trace of A is off-set horizontally for clarity. The inset shows a close-up of the characteristics near pinch-off. We obtain $\omega_y/\omega_x = (3.7 \pm 0.2)$ for B.

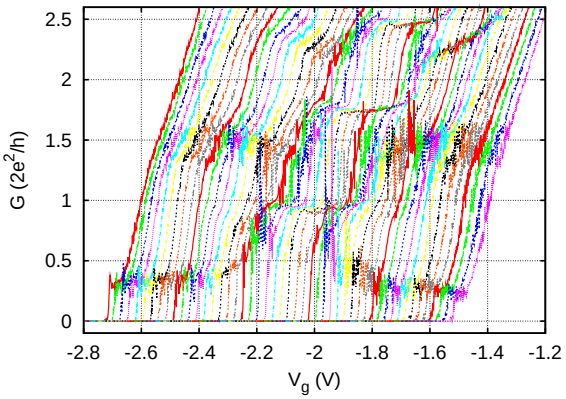

Figure A.7: Source-drain bias measurements for sample III at $T \approx 0.05$ K. The traces are off-set horizontally for clarity. The source-drain voltage V_{sd} is -6 mV for the left-most trace, and increases by 0.25 mV going to the right ($V_{sd} = +6$ mV for the right-most trace). The subband spacing is $\hbar\omega_y = (3.7 \pm 0.1)$ meV, which gives $\hbar\omega_x = (1.0 \pm 0.1)$ meV.

Bibliography

[1] H. A. Fertig and B. I. Halperin, *Phys. Rev. B* **36**, 7969 (1987).

[2] M. Büttiker, *Phys. Rev. B* **41**, 7906 (1990).

[3] C. W. J. Beenakker and H. van Houten, *Solid State Physics* **44**, 1 (1991).

[4] L. I. Glazman and A. V. Khaetskii, *Europhys. Lett.* **9**, 263 (1989).

[5] N. K. Patel, L. Martin-Moréno, M. Pepper, R. Newbury, J. E. F. Frost, D. A. Ritchie, G. A. C. Jones, J. T. M. B. Janssen, J. Singleton, and J. A. A. J. Perenboom, *J. Phys.: Cond. Matt.* **2**, 7247 (1990).

[6] N. K. Patel, J. T. Nicholls, L. Martin-Moréno, M. Pepper, J. E. F. Frost, D. A. Ritchie, and G. A. C. Jones, *Phys. Rev. B* **44**, 13549 (1991).

[7] L. Martin-Moréno, J. T. Nicholls, N. K. Patel, and M. Pepper, *J. Phys.: Cond. Matt.* **4**, 1323 (1992).